“In rust we trust” - Electrochemical and Photoelectrochemical Water Oxidation Using the Iron-Only Layered Oxyhydroxide Mössbauerite

DISSERTATION

zur Erlangung des akademischen Grades eines

Doktors der Naturwissenschaften (Dr. rer. nat.)

in der Bayreuther Graduiertenschule für Mathematik und Naturwissenschaften (BayNAT)

der Universität Bayreuth

vorgelegt von

Michael Maximilian Ertl

geboren in Sulzbach-Rosenberg

Bayreuth, September 2019

Die vorliegende Arbeit wurde in der Zeit von Juni 2016 bis September 2019 in Bayreuth am Lehrstuhl für Anorganische Chemie I unter Betreuung von Herrn Professor Dr. Josef Breu angefertigt.

Vollständiger Abdruck der von der Bayreuther Graduiertenschule für Mathematik und Naturwissenschaften (BayNAT) der Universität Bayreuth genehmigten Dissertation zur Erlangung des akademischen Grades einer Doktorin/ eines Doktors der Naturwissenschaften (Dr. rer. nat.).

Dissertation eingereicht am: 18.09.2019

Zulassung durch das Leistungsgremium: 26.09.2019

Wissenschaftliches Kolloquium: 30.04.2020

Amtierender Direktor: Prof. Dr. Markus Lippitz

Prüfungsausschuss:

Prof. Dr. Josef Breu	(Gutachter)
JProf. Dr. Anna Schenk	(Gutachterin)
Prof. Dr. Roland Marschall	(Vorsitz)
Prof. Dr. Seema Agarwal	

Meiner Familie

Content

List of abbreviations VI

1. Summary 1

2. Zusammenfassung 3

3. Introduction 5

3.1. The Necessity for Energy Storing Technologies 5

3.2. Electrochemical Hydrogen Production 7

3.3. Photoelectrochemical Hydrogen Production 13

3.4. Layered Base Metal Catalysts in Electrochemistry 16

3.5. Iron-Only Layered Hydroxides and Oxyhydroxides 18

3.6. Scope of Thesis 21

4. Literature 22

5. Synopsis 31

5.1. Electrocatalytic Water Oxidation with an Iron-Only Layered Oxyhydroxide 33

5.2. Mössbauerite/WO_3 Heterojunction Photoanodes 36

5.3. In-depth Study on the Structure of Iron-Only Layered (Oxy-)hydroxides 38

6. Results 40

6.1. Electrocatalytic Water Oxidation with an Iron-Only Layered Oxyhydroxide 40

6.2. Mössbauerite/WO_3 Heterojunction Photoanodes 68

6.3. In-depth Study on the Structure of Iron-Only Layered (Oxy-)Hydroxides 82

7. List of Publications 102

8. Acknowledgements 104

9. Eidesstattliche Verfassers 106

List of abbreviations

α	proportional to
CB	conduction band
CE	counter electrode
d	crystallographic d-spacing
DFT	density functional theory
E	potential
E_{eq}	equilibrium voltage / zero current cell voltage
F	Faraday constant
i	current
i_p	peak current
J	Joule
LDH	layered double hydroxide
LSV	linear sweep voltammetry
MS	Mott-Schottky
η	overpotential
NMBC	noble-metal-based catalyst
OER	oxygen evolution reaction
PEC	photoelectrochemical
R	universal gas constant
RE	reference electrode
RHE	reversible hydrogen electrode
RT	room temperature
T	temperature
UV Vis DRS	ultraviolet visible diffuse reflectance spectroscopy
v	scan rate

VB	valence band
WE	working electrode

1. Summary

Electrocatalytic water splitting by layered catalysts is dominated by materials containing expensive or toxic metals such as nickel and cobalt. Pure iron-based layered systems have been neglected due to their difficult accessibility, although iron has often been identified as the active metal center. In the context of this work it was possible to synthesize and characterize the oxidation stable material mössbauerite from the mixed-valent "green rust" LDH and to investigate its catalytic properties.

In the first part of the work, the phase-pure synthesis of mössbauerite is presented. The structure is similar to the γ-phase of the nickel oxyhydroxide which was already used as an electrocatalyst. Building on this, we used a layered iron oxyhydroxide as a catalyst in the oxygen evolution reaction. The material proved to be an efficient and stable electrocatalyst. The characterization showed that mössbauerite is a semiconductor without localized transitions.

Pure iron-based oxyhydroxides have already been used in earlier work as co-catalysts for photoanodes. After mössbauerite turned out to be an efficient electrocatalyst with semiconducting properties and a band gap in the visible range of the solar spectrum, it was investigated whether the material could be used as a co-catalyst. The band gap and band position of the material was determined for the first time. In combination with monoclinic tungsten(III) oxide, a type II hetero-junction should result. Photoanodes on which tungsten(III) oxide was deposited by electrophoresis were additionally coated with mössbauerite and showed an increase of the current flow by more than 10%. Also, the experimental determination of the band gap was in excellent agreement with DFT+U calculations of the electronic structure.

In the third part of the work, both the electronic and especially the crystallographic structure of mössbauerite were investigated. Starting from the observation in the first paper that the layer distance is significantly smaller than in related structures, the assumption was investigated that the structure in the interlayer changes during oxidation from "green rust" to mössbauerite. The degrees of freedom in FTIR were used to demonstrate that carbonate in the interlayer is bound to the layers during oxidation. This observation causes a shrinkage of the layer distance to 7.0 Å and could be proved plausible by DFT+U calculations. A structural model was established by quantum mechanical calculations and subsequently refined under the assumption of a randomized alternating storage of layers with bound and free carbonate in the intermediate layer.

This thesis is presented as a cumulative work; therefore, the results are described thematically in the attached manuscripts.

2. Zusammenfassung

Die elektrokatalytische Wasserspaltung durch schichtartige Katalysatoren wird von Materialien dominiert die teure oder toxische Metalle wie Nickel und Kobalt enthalten. Rein Eisen-basierte schichtartige Systeme wurden durch ihre erschwerte Zugänglichkeit vernachlässigt obwohl Eisen häufig als das aktive Metallzentrum identifiziert wurde. Im Rahmen dieser Arbeit ist es gelungen, ausgehend von dem gemischt-valenten „green rust“ LDH, das gegen Oxidation stabile Material Mössbauerit zu synthetisieren, charakterisieren und hinsichtlich seiner Katalyse-Eigenschaften zu untersuchen.

Im ersten Teil der Arbeit wird die phasenreine Synthese von Mössbauerit präsentiert. Die Struktur weist Ähnlichkeiten mit der γ-Phase des Nickeloxyhydroxids auf welches bereits als Elektrokatalysator eingesetzt wurde. Darauf aufbauend haben wir ein schichtartiges Eisenoxyhydroxid als Katalysator in der Sauerstoffevolutionsreaktion eingesetzt. Das Material erwies sich als effizienter und stabiler Elektrokatalysator. Im Zuge der Charakterisierung zeigte sich, dass es sich bei Mössbauerit um einen Halbleiter ohne lokalisierte Übergänge handelt.

Rein Eisen-basierte Oxyhydroxide wurden in früheren Arbeiten bereits als Co-Katalysatoren für Photoanoden eingesetzt. Nachdem Mössbauerit sich als effizienter Elektrokatalysator mit halbleitenden Eigenschaften und einer Bandlücke im sichtbaren Bereich des Sonnenspektrums herausgestellt hat, wurde untersucht, ob das Material als Co-Katalysator verwendet werden kann. Im Zuge dessen wurde zum ersten Mal die Bandlücke und Bandposition des Materials bestimmt. In Kombination mit monoklinischem Wolfram(III)oxide sollte sich eine Typ-II Hetero-Junction ergeben. Photoanoden auf denen durch Elektrophorese abgeschiedenes Wolfram(III)oxid zusätzlich mit Mössbauerit belegt wurde, zeigten eine Verstärkung des Stromflusses um mehr als 10%. Die Bestimmung der Bandlücke zeigte sich in guter Übereinstimmung mit DFT+U Berechnungen zur elektronischen Struktur.

Im dritten Teil der Arbeit wurden sowohl die elektronische, aber besonders die kristallographische Struktur des Mössbauerit untersucht. Ausgehend von der Beobachtung in der ersten Arbeit, dass der Schichtabstand deutlich geringer ist als in verwandten Strukturen, wurde die Annahme untersucht, dass sich während der Oxidation von „green rust“ zu Mössbauerit die Struktur in der Zwischenschicht ändert. Es konnte anhand der Freiheitsgrade im FTIR nachgewiesen werden, dass Carbonat in der Zwischenschicht während der Oxidation an die Schichten gebunden wird. Diese Beobachtung verursacht ein Schrumpfen des Schichtabstands zu 7.0 Å und konnte durch DFT+U Berechnungen als plausibel belegt werden.

Es wurde ein Strukturmodell durch quantenmechanische Rechnungen aufgestellt und anschließend unter der Annahme einer randomisierten Wechsellagerung von Schichten mit gebundenem und freiem Carbonat in der Zwischenschicht verfeinert.

Bei dieser Arbeit handelt es sich um eine kumulative Dissertation, daher werden die Ergebnisse thematisch sortiert in den angehängten Manuskripten beschrieben.

3. Introduction

3.1. The Necessity for Energy Storing Technologies

While the necessity for energy is rather obvious – starting from the most basic such as food preparation or, more recent, almost all comfort appliances – the necessity for energy storing technologies, however, has arisen rather recently as a crucial topic in countless scientific approaches.[1-3] Roughly with the turn of the millennia, the work on 'energy storage' increases significantly with increasing speed (Figure 1).

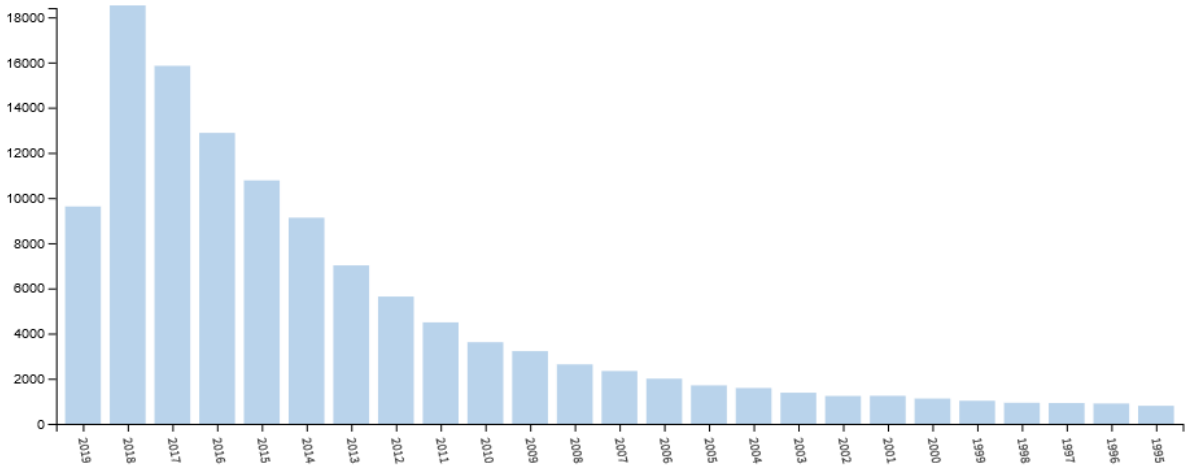

Figure 1: Bibliographic analysis of the keyword 'energy storage' in publications with Web of Science (last update: June 2019).

This trend is caused by the transition from fossil fuels (such as coal or crude oil)[4] to renewable energy (such as solar radiation, winds, waves, tides),[5-6] which, in return, is happening due to two major causes. An increasing environmental awareness caused by the undeniable changing climate and the depletion of fossil fuels.[7-9] Renewable sources could easily provide sufficient energy to make fossil fuels obsolete. The worldwide energy consumption by the human population accounts to roughly 13 terawatts, whereas the sun alone provides 120,000 TW per year.[10-12] Obviously, the amount of energy is sufficient, its intermittence, conversion, and storage are issues that need to be tackled. While there is a wide range of storage possibilities (thermal, mechanic, electric, chemical), this work will be focused on molecular hydrogen (H_2), the lightest existing molecule.

Already today, approximately 60 million tons are produced each year,[13] of which almost half is consumed in the Haber-Bosch process. If considered as a fuel, hydrogen has the major advantage to be a clean energy carrier since its combustion with oxygen yields only water as a product alongside energy. This resulted in the idea of a *hydrogen economy* which is based on

hydrogen as the primary fuel. The concept itself is (in a very simplified version) straightforward and schematically depicted in Figure 2.

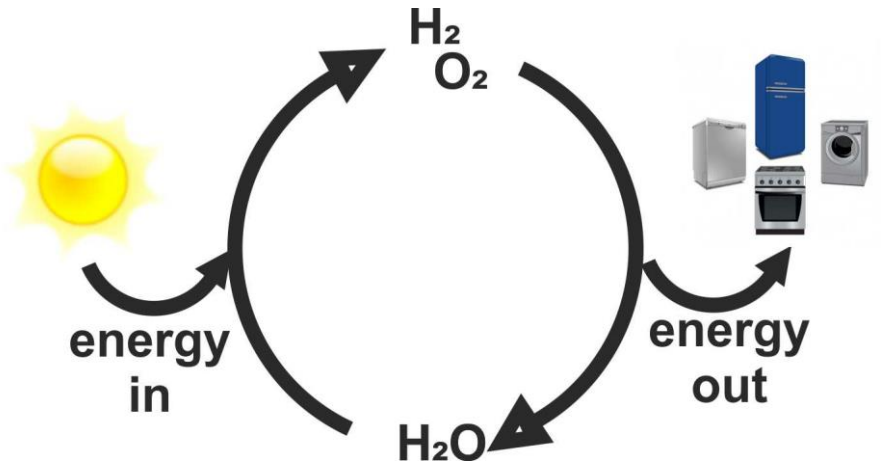

Figure 2: Schematic general concept of an idealized hydrogen economy. (based on[14])

As a closed reaction cycle, no additional compounds are produced or consumed – and hydrogen acts energy carrier to mediate between input and output. Currently, the major share of hydrogen, however, is produced by the steam reforming process (Equation 1)[15]

$$CH_4 + H_2O \rightleftharpoons CO + 3H_2 \tag{1}$$

The initial, mainly nickel-catalyzed, conversion of methane is followed by the water-gas shift reaction to convert the produced carbon monoxide with water according to Equation 2.

$$CO + H_2O \rightleftharpoons CO_2 + H_2 \tag{2}$$

As a rapidly emerging, and currently the second most contributing method, the electrolysis of water in order to produce hydrogen poses a reaction that is completely independent of carbon-based molecules or compounds.[16] Therefore, it could sustain the energy supply (if being scaled up intensely) regardless of the depletion of fossil fuels and is a major step towards an ideal, functioning hydrogen economy. The electrolysis or electrochemical production of hydrogen will be discussed in the following chapter.

3.2. Electrochemical Hydrogen Production

The phenomena of water splitting was initially observed and documented to some extent by Deinman and van Troostwijk in 1789.[17] The decomposition of water into so-called 'combustible' and 'life-giving' air was soon to be followed by many others such as J.W. Ritter or William Nicholson only to by visualized by Alessandro Volta and published in The Royal Society as a letter to Joseph Banks (Figure 3).[18-19]

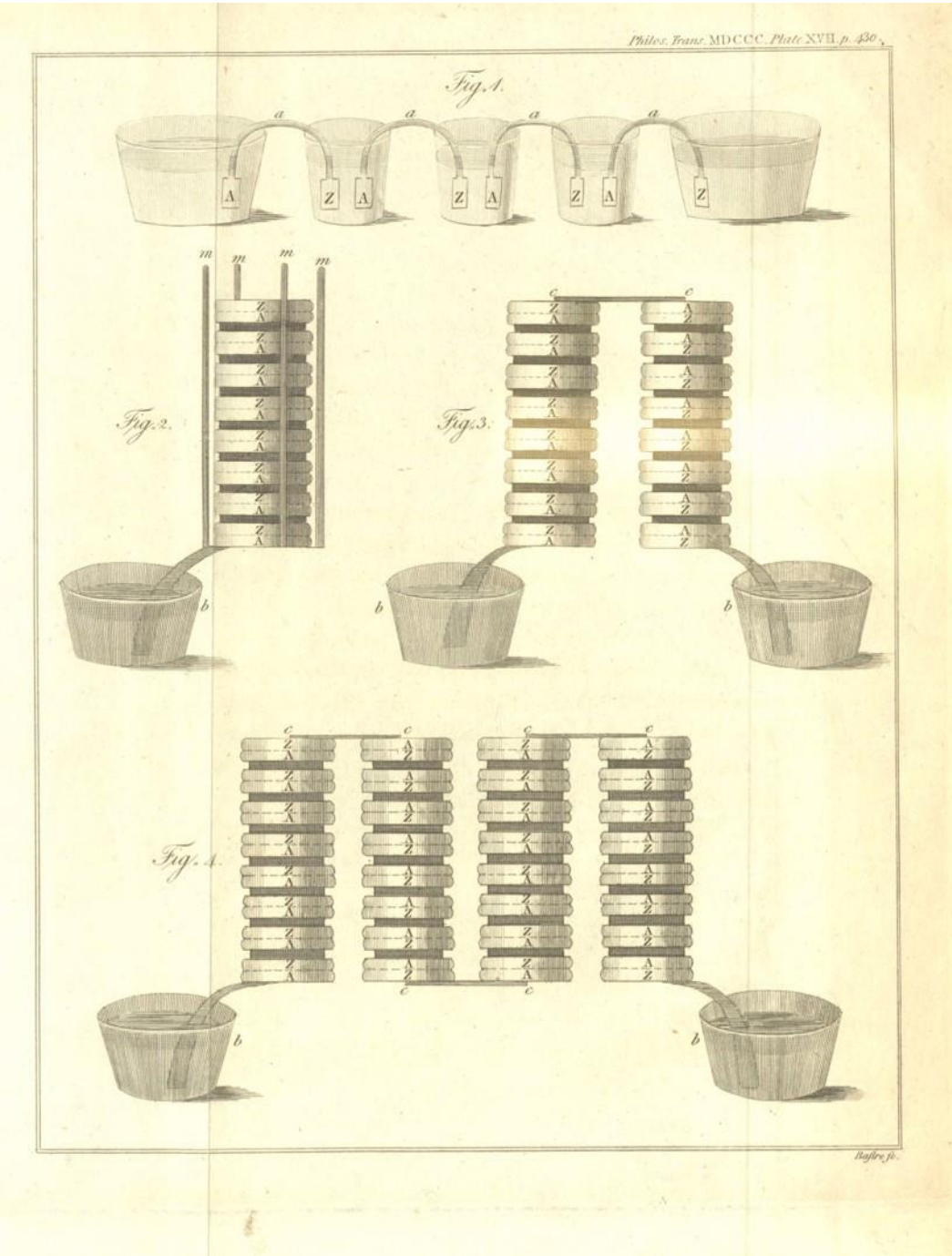

Figure 3: The voltaic pile or 'Organe électrique artificiel' as originally depicted by Alessandro Volta in June 1800. (reprinted with permission from the Royal Society[19])

Whereas the technology of electrolysis cells has come a long way in the past 200 years, the thermodynamics behind the decomposition have, quite understandably, not changed. The zero current cell voltage E_{eq} to split water can be derived from the Gibbs free energy of the formation of water ΔG_f^0. The relation of E_{eq} and ΔG_f^0 is expressed as:

$$E_{eq} = {-\Delta G_f^0}/{2F} \qquad (3)^{20}$$

where F is the Faraday constant ($F = 96{,}500\ {}^{J}/_{V}$) and the 2 in the denominator origins from the two electrons necessary to form molecular hydrogen and oxygen. At standard ambient temperature (25 °C / 298 K), $\Delta G_f^0 = -237.1\ kJ\ /\ mol$. Therefore, the thermodynamically necessary voltage to exceed the stability region of water and to initiate its decomposition equals 1.23 V versus the reversible hydrogen electrode (RHE).[21] Commercial electrolyzers, however, usually operate ranging above 1.8 V.[22] This deviance from the thermodynamically necessary potential is referred to as the overpotential η of an electrochemical reaction. The experimental determination and of the overpotential and its origins will be discussed in the following chapter in a short overview of voltammetry in aqueous media.

3.2.1. The study of electrolysis mechanisms by voltammetry

By measuring the electrode current as a function of the applied voltage in electrolysis cells, in-depth information about the cell characteristics and electrochemical mechanisms can be obtained. In the most elementary approach, information results from the measurements with only two electrodes. The working electrode (WE) conducts the reaction that is to be analyzed. Secondly, the reference electrode (RE) that is supposed to provide a fixed and constant potential to define the drop in potential between WE and the surrounding electrolyte. This configuration, however, is only applicable for a minuscule current flow *e.g.* in microelectrodes. The relation between the potential E and the passing current i is described by:

$$E = (\phi_m - \phi_s) + iR + (\phi_s - \phi_{ref}) \qquad (4)^{23}$$

The first term describes the driving force for electrolysis at the WE, iR origins from the passage of current between electrodes and describes the voltage drop at the WE/electrolyte interface. The third term is the corresponding voltage drop at the RE/electrolyte interface. While the second term in negligible in microelectrode setups, with larger electrodes it is not and therefore affects the cell potential E. This issue is solved by using three-electrode setups with an additional counter electrode (CE). The electrodes are connected to and controlled by a potentiostat, where current only flows between WE and CE, whereas the potential of the RE is

held constant.[24] This setup usually is combined with a rotating disk electrode (RDE) to avoid or minimize diffusion layers that would add additional overpotential.[25] Figure 4 shows a schematic presentation of a three-electrode setup.[26] For the characterization of the processes at the WE, glassy carbon (GC) is a standard material which is usually covered with a catalyst 'ink' of catalyst and Nafion® in a mixture of ethanol and water. Noble metals or noble metal alloys at the CE catalyze the hydrogen evolution reaction (HER)[23, 27] and the electrolyte is saturated with gas (oxygen) to create an equilibrated and also standardized state.[28] This, however, has been the issue of some discussion in recent years.[29]

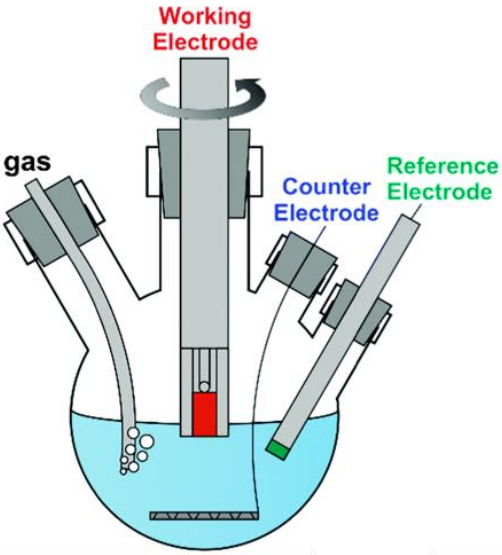

Figure 4: Schematic presentation of a three-electrode setup with RDE. (reprinted with permission from the Royal Society of Chemistry[26])

Using such a setup, various reversible or irreversible electrochemical methods can be performed to characterize electrochemically active materials or processes. Linear-sweep voltammetry (LSV) is a quite simple technique to perform and evaluate but still provides useful information about the system and is a standard technique to benchmark the efficiency of electrocatalysts. By sweeping the electrode in a range of typically between 5 mVs^{-1} and more than 10^2 Vs^{-1},[23] in a range from a value E_1 where no reaction is happening to a potential E_2 where electron transfer is driven by an electrochemical reaction such as the oxygen evolution reaction (OER). If the LSV is extended to a back-sweep in the same potential range as the first sweep, the technique is called cyclic voltammetry. CV runs are used to 'condition' electrodes before performing benchmark activities but also to investigate the kinetics of electrochemical reactions.[30]

Initially, the applied voltage is not sufficient to catalyze the desired reaction – consequently, no current is flowing, but the electrodes are 'charged', comparable to plates in a capacitor. In Figure 5A, this would correspond to the range below 1.4 V vs. RHE. After a certain threshold is reached, the oxidation of water proceeds at the anode as follows:

$$H_2O \rightarrow \frac{1}{2}O_2 + 2H^+ + 2e^- \qquad (5)^{31}$$

This oxidative half-cell reaction is actually a four-electron process (since half an oxygen molecule does not exist) and therefore thermodynamically and kinetically more demanding than the reductive hydrogen evolution.[32] However, if this energy barrier is surpassed, electrons flow from the anode to the cathode to reduce protons. In general, it can be stated, that the sooner and steeper the current starts to increase, the better the catalyst.

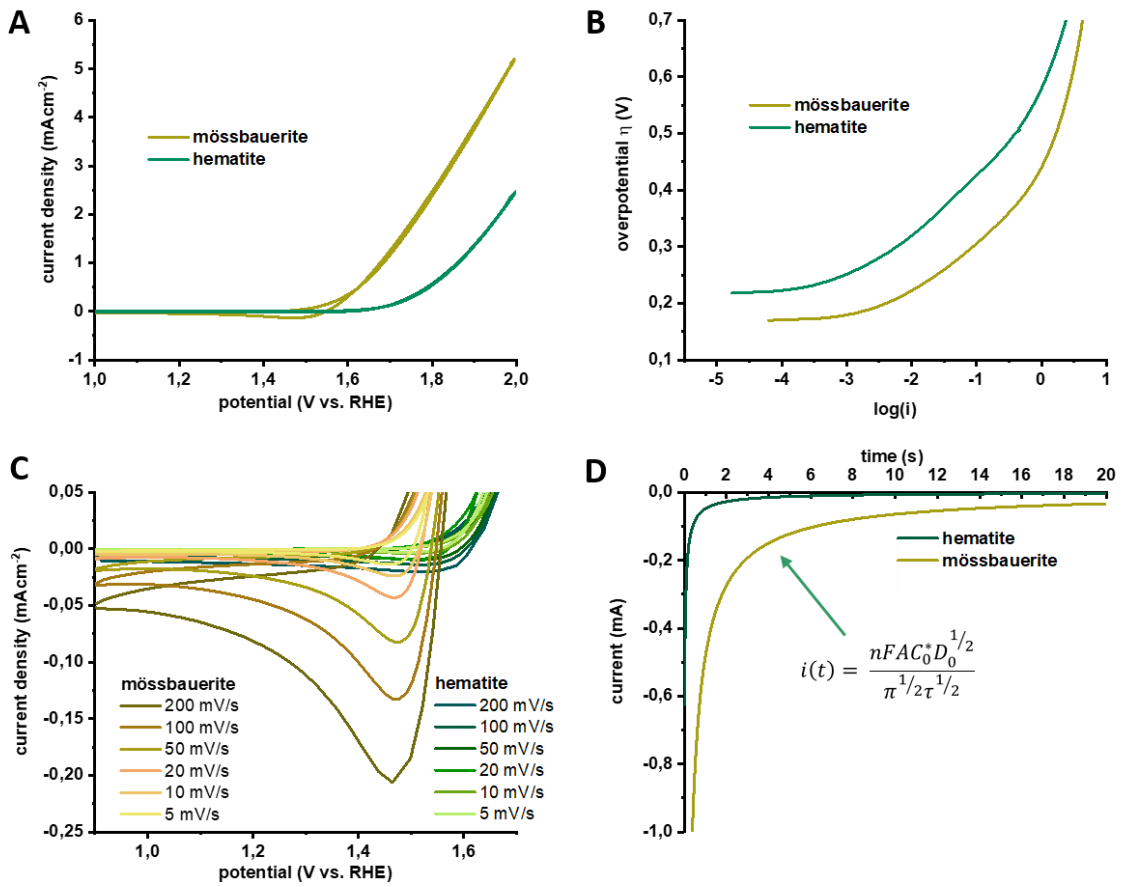

Figure 5: Electrochemical characterization of crystalline hematite and amorphous mössbauerite. (A) Cyclovoltammetric (CV) measurements for the mössbauerite and hematite films (performed in 1.0 M NaOH) which show a distinct cathodic shift in the onset potential. (B) Tafel plots for both the mössbauerite and hematite films. The dotted lines are the extrapolated Tafel slopes and the table shows the values of the Tafel slopes and the exchange current for each film. (C) Scan-rate-dependent CV measurements for both films. The peak current for the reduction wave in mössbauerite is proportional to the square root of the scan rate, indicating a diffusion-controlled redox process. In hematite, the peak current for the reduction wave is proportional to the scan rate indicating a surface-bound redox species. (D) Potential step experiments for both films. The films were held at a potential of 1.9 V vs. RHE for 5 min, followed by a potential step to 0.9 V vs. RHE. The resulting current-decay profile exhibits diffusion-controlled dynamics in the mössbauerite film in contrary to the resulting current-decay profile in hematite.

Electrochemical characterization beyond LSV and CV is used to investigate materials more detailed. Figure 5B shows Tafel plots of the catalysts as the overpotential vs. a logarithmically scaled x-axis of the current. In this case, the slopes are fairly similar and therefore suggest similar kinetic activities or similar kinetic limitations.[33] The slopes of 111 mVdec^{-1} for hematite

and 92 $mVdec^{-1}$ for mössbauerite indicate a predominant surface-species formed in a step just before the rate-determining step.[33-35] This, however, is again subject to discussion since the slopes are also depending on the setup. The possibilities of an in-depth analysis of CV experiments is shown in Figure 5C. Upon reverse cycling during the CV measurement, a reduction wave was observed at the point of water oxidation onset for both films. This peak has been observed for a number of iron oxide electrocatalysts reported in the literature and the origin of the peak species will be discussed in the following.[36-37] For the mössbauerite sample, the peak current density follows a scan rate-dependence of $i_p \ \alpha \ v^{0.5}$, indicating a diffusion-controlled process. While the water oxidation intermediate appears to be under diffusion control in the mössbauerite film, the scan rate-dependence of the reduction wave in the case of the hematite film appears to indicate that this intermediate is surface bound and not under diffusion control. This is evident from the fact that $i_p \ \alpha \ v^1$ for the hematite film.[23] While the species itself is difficult to determine from those experiments, it is evident, that the results indicate different processed in the system. Finally, potential step experiments as shown in Figure 5D can contain information about diffusion coefficients of intermediates.[38]

It is evident, that the information depth of EC experiments goes far deeper than benchmarking a current density at the lowest possible to characterize electrochemically active materials. However, the activity is from an economical point of view still the most decisive. In the following chapter, state-of-the-art OER electrocatalysts will be discussed regarding their performance, advantages, and disadvantages as well as the general direction of research in this field at the moment.

3.2.2. State of the art heterogeneous oxygen evolution electrocatalysts

The high overpotential of the OER is the critical issue in electrocatalytic water splitting. Noble-metal free or non-precious metal-based catalysts are dominating current research efforts on the reduction of the OER overpotential. However, noble metal based catalysts (NMBCs) still have some beneficial characteristics that make them highly interesting materials regarding current density or durability.[39] In the following, the advances in NMBC research for the OER will be discussed briefly with a focus on composition, structure, and morphology of iridium, ruthenium and other precious-metal-based metals, alloys or oxides.

Tuning the composition of ‘composite’ catalysts generally pursues two targets: reducing the usage of noble metals and increasing the intrinsic activity of active sites. Ruthenium (RuO_2) and iridium oxide (IrO_2) are usually listed as ‘state-of-the-art’ reference materials when new work is published on OER catalysts.[40] The complexity of the OER with countless possible

decisive transition states, however, makes it difficult to define a reference catalyst.[26] *In-situ* XPS studies showed rather recently, that during the OER process Ir^{IV} is oxidized partially to Ir^{V}.[41] Additionally, the surface is partially converted to an iridium oxyhydroxide during operation. Consequently, a purely IrO_xOH_y thin film was synthesized and showed superior activity to both, amorphous and crystalline iridium oxide.[42] Also, (unintentional) foreign metal doping shows significant influence on the activity of catalysts by several magnitudes. If the influence of the microstructure and the morphology of catalysts is taken into account, it is obvious, that referencing the performance of new materials is difficult. McCrory *et al.* published an objective evaluation of the activity of electrocatalysts for the OER in alkaline media which is an excellent starting point for the comparison of activities.[43] Figure 6 shows that, when comparing the catalysts under similar conditions, iridium oxide is superior to a wide variety of oxidic mixed-metal oxides.

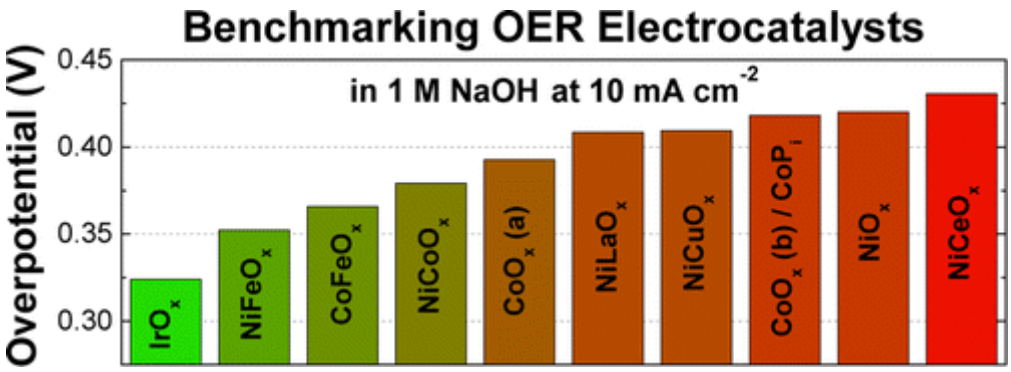

Figure 6: Necessary overpotential of various oxidic OER electrocatalysts to sustain a current density of 10 mAcm^{-2} in alkaline media.(reprinted with permission from the American Chemical Society[43])

As mentioned at the beginning of this chapter, precious metal free catalysts are dominating research efforts regardless of the performance of iridium oxide. For the simple reason that noble-metals are scarce, and if water splitting is to be employed large-scale for hydrogen production, the amount of OER catalysts necessary exceeds the availability of iridium or ruthenium by far. Therefore, precious-metal-free materials need to be, and of course have been, evaluated as potential catalysts and improved regarding activity and stability.

If precious metals are to be avoided, benchmarking OER catalysts at this point are layered hydroxides or oxyhydroxides in various combinations of manganese, iron, cobalt, and nickel. Those, however, will be discussed by their general application in electrochemistry in chapter 3.4. In the following chapter, the photoelectrochemical (PEC) hydrogen production will be discussed. Especially the particularities compared to the electrochemical OER will be in the focus.

3.3. Photoelectrochemical Hydrogen Production

Water splitting by photoelectrochemistry enables the conversion of solar energy into useable and storable energy. According to the Nernst equation, 1.23 V is necessary per electron transferred. Ideally, a single, semiconducting catalyst has a band-gap that is large enough to surpass this energy. Additionally, the band energy needs to span over both electrochemical potentials of H^+/H_2 and O_2/H_2O.[44]

Since the first report on titanium dioxide TiO_2 by Honda and Fujishima in 1972[21] on the electrochemical photolysis of water, the focus of countless researchers has been on the development and testing of new (semiconducting) materials for both half-cell reactions. Unfortunately for later researchers, Honda and Fujishima 'discovered' with TiO_2 an already highly effective catalyst due to its stability under operation, its low cost, and its low-lying valence band, which in return results in highly oxidizing holes upon exciton generation.[45-46] The general mechanism of photocatalysis is shown in Figure 7. In the photolysis of water, the conversion of D^- to D corresponds to the reaction at the valence band, the oxidation of H_2O to O_2. The corresponding reaction at the conduction band is the reductive evolution of H_2 from protons.

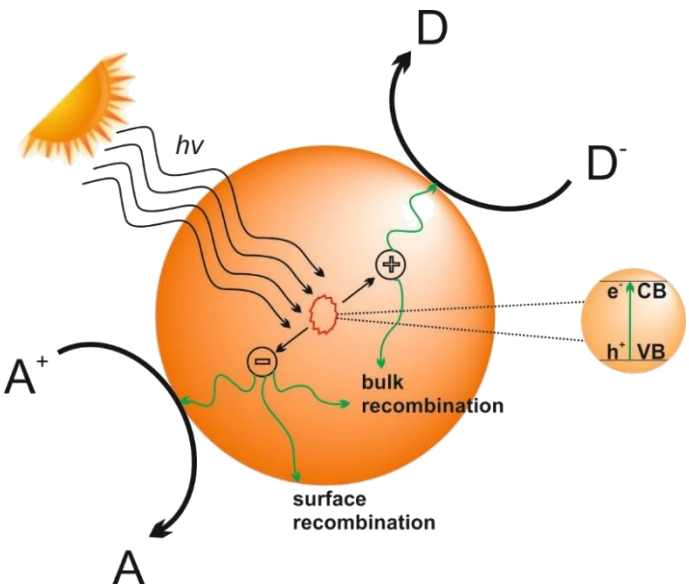

Figure 7: Photocatalysis of a semiconducting material. Photogenerated excitons reduce electron acceptors (A) and reduce electron donors (D). Competing reactions such as bulk recombination or surface recombination lower the incident photon to current efficiency by mainly non-radiative processes. (based on[44])

This illustration, however, is a bit deceiving for TiO_2. The band-gap of TiO_2 is the range of 3.2 eV, corresponding to radiation with a wavelength of 387 nm. If no light above this wavelength is absorbed, the complete visible region is reflected, resulting in its white color and leaving roughly 95% of the solar spectrum idle.[44] While extensive effort has been spent in

decreasing the band gap of TiO_2,[47] many other metal oxides (such as tungsten oxide) with significantly lower band-gap exist and have been employed as photoanodes.

3.3.1. Tungsten oxide photoanodes

Soon after the first reports on photoelectrochemical (PEC) cells with TiO_2, tungsten trioxide (WO_3) has attracted attention as a photoanode due to the aforementioned drawback of TiO_2's large band-gap.[48] The structure of WO_3 is temperature dependent.[49] Except for elaborate synthesis procedures that yield orthorhombic WO_3,[50] monoclinic or triclinic phases are stable at room temperature. The band-gap of WO_3 is roughly 2.7 eV; thus significantly smaller than that of TiO_2 and therefore at least 12% of the solar spectrum can generate excitons.[51] Large band-gap n-type semiconductors (such as TiO_2 or WO_3) suffer from small electron mobility and short hole diffusion lengths.[52] This significantly enhances the recombination rate and lowers incident photon-to-current efficiency drastically. Mainly charge carriers that are generated within the depletion range produce photocurrent. Doping, hydrogen treatment and nanostructuring are means that are usually employed to tackle this issue of bulk materials by augmenting the electrolyte/semiconductor interface or by increasing the charge mobility. An elegant approach to increase the efficiency has arisen by forming heterojunctions of two (or more) different semiconductors. This concept of heterojunctions and co-catalysts as photoanode materials will be discussed in the following

3.3.2. Co-catalysts in photoelectrochemical water splitting

As stated earlier, for semiconducting materials to catalyze the oxidative oxygen evolution, the valence band must be energetically higher (more positive) than the O_2/H_2O potential. If a dual system of two materials is used, there are three major types of heterojunctions (if two semiconducting materials are assumed).[53] Figure 8 shows the three main types of heterojunctions of two semiconducting materials in contact.

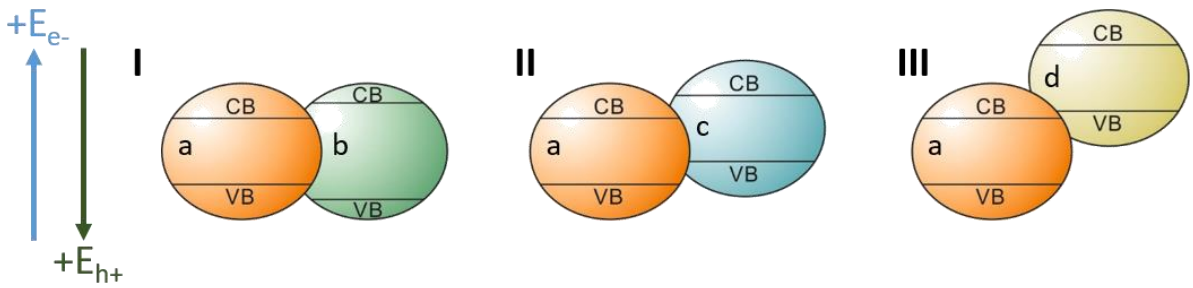

Figure 8: Band position of type I, II, and III heterojunctions. (based on[54])

Depending on the type of semiconductor (p-type: hole as majority charge carriers; n-type: electrons as majority carriers) either electrons or holes / defect electrons contribute mainly to

the total charge passed through the material. Figure 8I shows the energy alignment of a type I heterojunction where conduction band (CB) and the valence band (VB) of material ‘a’ are energetically lower. Therefore, both electrons and holes are collected in ‘a’. For type II, created excitons (or charges) are separated effectively, since holes are transferred to ‘c’ and electrons to ‘a’. A type III heterojunction is rather similar to type II, except that the energetic ‘distances’ of CB and VB of the two semiconductors are far more distinct.

Especially type II heterojunctions have been shown to have promising OER activities when employed as photoanodes (for the above-mentioned reason of improved charge separation).[55-57] Tungsten oxide, for example, has been shown to highly efficient with iron oxides, hydroxide, and oxyhydroxides.[58-59] However, with two- or more fold combinations and countless morphologies, research on semiconducting materials for catalysts and co-catalysts as photoanodes is far from being completed. As mentioned in 3.2.2, layered base metal catalysts are currently top-performing materials for OER and are also used for photoelectrochemistry. The following chapter will give an overview over prominent representatives and applications before focusing on the two iron-based materials green rust and mössbauerite.

3.4. Layered Base Metal Catalysts in Electrochemistry

Layered hydroxides and oxyhydroxides of various compositions are currently the top-performing electrocatalysts for the OER.[60-63] Regardless of the composition, the structures can be described by similar structural features. They consist of brucite-like layers where metal cations (whose charges vary from +2 to +4) are octahedrally coordinated by OH^- or O^{2-} or mixtures of both. Additionally, in some cases anions are grafted to the layers and are therefore accounted as part of the layer.[64-65] Regardless of grafted or non-grafted, the counter ions 'A' are necessary to compensate excess charge in the brucite-like layers. The excess charge results from deviations of the stoichiometries of $M^{2+}(OH)_2$, $M'^{3+}OOH$ or $M''^{4+}O_2$. Figure 9 shows an (probably) incomplete scheme of different representatives of layered materials that are based on the brucite structure.

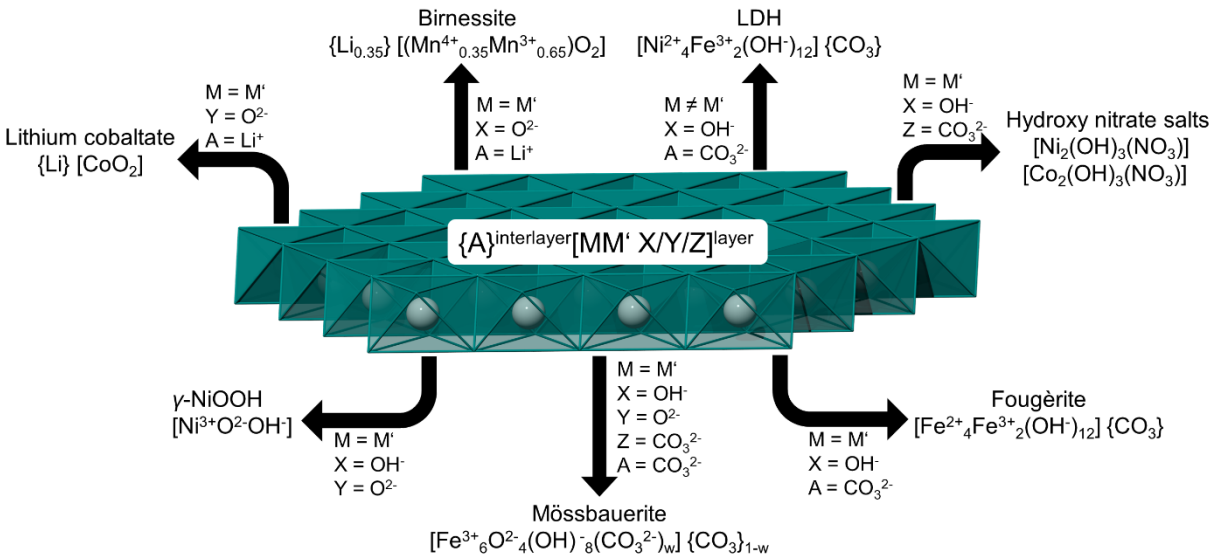

Figure 9: Overview (with no claim of completeness) of brucite-type (hydr-)oxides with one or two different types of metals of equal or different oxidation states and possible anionic or cationic interlayer ions.

In oxidic cobaltate and birnessite, the mean oxidation state of the octahedral cations is below 4+, therefore, lithium cations reside in the interlayer. Consequently, both materials can be used in Li-Ion batteries.[66-67] The γ-phase of nickel doesn't carry a layer charge due to its trivalent charge and the coordination with oxide and hydroxide to equal parts. The redox flexibility of nickel however, allows a net charge of around +3.7 before its electrochemical potential would initiate a reduction of oxygen.[68] If the nickel is overcharged, it has been shown to intercalate alkali metal ions (Li^+, Na^+, K^+) and can be used as electrodes in batteries.[69] Layered double hydroxides (LDH) have been used as passivation layers,[70] flame retardants,[71] adsorbents[72] and many other applications before being discovered as highly efficient electrocatalysts.[73] The depicted nickel-iron LDH is probably the most prominent and efficient OER catalyst. The

majority of the most active materials contain toxic or expensive metals such as cobalt, nickel, manganese or vanadium and are accessible only by costly synthesis procedures.

The 2:1 ratio of bivalent to trivalent metal ion requires a densely packed interlayer of carbonate. A lower ratio than 2:1 can therefore not be achieved without structural changes (deprotonation of hydroxyl groups) or secondary phases.[74] In addition to carbonate, structural water is in the interlayer in smaller voids. The weak interactions in the crystallographic *c* direction (perpendicular to the layer) allow massive planar defects where layers are stacked in random ways.[75] By this turbostratic disorder, structural characterization by X-ray diffraction is gravely complicated.[76]

If applied as electrocatalysts, LDHs have been shown to get partially oxidized.[77] The higher charge of the octahedrally coordinated metals ions has a greater attraction to the binding electrons of the hydroxyl groups and make the protons more acidic. If excess charge is generated, even deprotonation or grafting of interlayer anions are probabilities.[78] These processes are usually the result of applied potential (or temperature) and not observable under standard conditions. The fougèrite group however, is an exception compared to other LDHs. If both, bi- and trivalent metal ions are iron, the flexibility between the two oxidation states allows to study the redox behavior and structural responses of a stable layered ferric iron-only oxyhydroxide. The two representatives of the fougèrite group green rust and mössbauerite will be discussed in the following.

3.5. Iron-Only Layered Hydroxides and Oxyhydroxides

3.5.1. The Fougèrite Group

Fougèrite group minerals are unique among LDHs because iron makes up both, bi- and trivalent ions in the brucite-like layer.[79-83] Members of the group were first discoverer in hydromorphous soil and at the French coast near Fougères in coastal gley.[81] In their mixed-valence state, they show a characteristic but only transient greenish-blue color. Possible interlayer anions are carbonate, chloride, sulfate, oxalate and others. In nature however, the affinity towards and incorporation of carbonate is dominating.[84] Aerial oxidation of green rust results in amorphous ferric oxyhydroxides such as feroxyhyte, lepidocrocite or goethite.[85-87] This transition by dissolution and reprecipitation corresponds to a vertical motion in the Pourbaix diagram from the stability region of green rust. In-situ oxidation using a strong oxidant however, leads to a different result. The crystal structure of the LDH is not dissolved but reacts in a topotactic deprotonation to a phase that was named mössbauerite.[78] Consequently, corrosion of iron and mixed-valence iron phases had to be revisited since the new member in ferric oxyhydroxide species was found.

3.5.2. Green Rust

Green rust is a typical LDH of quintinite structure (2:1 metal ratio), comprising layers of octahedrally coordinated bi- and trivalent metal ions.[88] All ligands being hydroxide groups results in a layer composition of $[Fe^{2+}{}_4Fe^{3+}{}_2(OH)_{12}]$. This results in an excess positive charge of +2 which is compensated by interlayer anions as mentioned in 3.5.1. Depending on the interlayer anion, different modes of layer stacking are observed. If carbonate is intercalated, a *R*-3*m* stacking and if sulfate is present, a *P*-3*m*1 stacking is observed.[89]

Beyond its presence in maritime marshes, green rust has attracted severe interest because of its potential role in the origin of life in Precambrian oceans at hydrothermal vents.[90-91] The redox-flexibility by switching between the ferric and ferrous oxidation state might act as an early, simplified ATP/ADP system. While green rust might have had a crucial role in the early life cycles, the redox behavior has not yet been made use of with one exception. Nitrite and nitrate reduction to ammonium, which is increasingly necessary to avoid over fertilization, have successfully been implemented in testing plants.[92] Usually, the transient nature of green rust towards oxidation prevents the application of the material in other (redox) reactions since they result in amorphous iron oxyhydroxides that can’t be converted back to green rust. Recent reports however, have shown, that green rust can be converted to an oxidation stable structure without losing its structure by rapid oxidation with strong oxidants.[78, 82] The resulting layered

oxyhydroxide named mössbauerite will be discussed in the following part and is the main focus of this work.

3.5.3. Mössbauerite

Originally discovered by Génin *et al.*, mössbauerite was discovered in 2006 after the oxidation of green rust with hydrogen peroxide.[79] The oxidation is accompanied by the deprotonation of hydroxyl groups to compensate for the excess charge induced by the oxidation from mixed-valence to all ferric iron. If no other mechanism (such as dissolution-reprecipitation) is present, the formula of carbonate interlayered mössbauerite is as follows: $[Fe^{3+}{}_6O_4(OH)_8]^{2+}(CO_3^{2-})\cdot 3H_2O$.

The structure of mössbauerite differs in part to the one of green rust and other LDHs. The morphology of hexagonal platelets is mainly conserved during the oxidation – indicating no complete loss of the LDH structure. The first XRD study of mössbauerite however, showed diffraction peaks that indicated a layer spacing of around d = 7 Å which is unusually small for carbonate interlayered structures.[78] This was interpreted as considerable stacking disorder and intergrowths of two- and three-layer structure. While considerable stacking disorder is highly probable, this would not explain the presence of more than one *00l* *d*-spacings in the XRD (if an ordered heterostructure is ruled out. If more than one *d*-spacing is present in a layered material, the *001* is averaged by the X-ray beam and later reflexes shifted to the *d*-value of the majority phase.[93-94] Since two distinct *001* reflexes were observable, probably two different were present in the sample. One with a *d*-spacing of 7.4 Å and one with 7.0 Å.

A *d*-spacing of 7.0 Å has been observed for another layered transition metal oxyhydroxide material: the γ-phase of nickel oxyhydroxide.[68] When γ-NiOOH is used in battery setups, it has been observed, that the material suffers from self-discharge.[95-96] This discharge reaction in return, is related to the oxygen evolution in the electrocatalytic water splitting. Mössbauerite as an iron-only layered structure related to γ-NiOOH, that has not yet been employed as electrocatalyst, makes it an intriguing material to be employed. Both, non-toxic iron oxyhydroxides and mixed-metal LDH structures have been shown to be efficient electrocatalysts. Mössbauerite combines the composition of the first and almost the structure of the latter. Additionally, the role of iron in LDHs is under some discussion whether it is the active acting metal.[97-99] Therefore, mössbauerite poses a promising and untapped material for OER catalysis. The synthesis, structure, and application as electrocatalyst are reported and discussed in this work.

3.6. Scope of Thesis

The necessity for the industrial-scale conversion of renewable to also storable energy is the base from which this work arose. The thrive towards innovative, cheap, non-toxic and stable catalysts was the motivation to synthesize, characterize and apply a material the comprises only of the metal iron and bears the potential to produce molecular hydrogen from water efficiently and sustainably. The naturally-occurring mineral "green rust" of the fougèrite group lays the foundation to access a Fe^{3+}-only material named mössbauerite that has been overlooked so far from many. The transient nature of the precursor green rust, the highly disordered layered structure and its flexibility regarding redox-activity, composition, and morphology make it an equally intriguing and frustrating material. In this regard, no previous work has collectively looked at the synthetic details, compositional and structural details, interlayer state, electronic properties or electrocatalytic properties.

Layered Double Hydroxides (of which the fougèrite group is a part of) with the sum formula $[M^{2+}{}_4M'^{3+}{}_2(OH)_{12}]\ (X^{n-})_{2/n}$ are a very versatile group of materials since the structure tolerates a variety of different metal cations as well as counter anions in the interlayer. The structure of alternating brucite layers ($M(OH)_2$) and layers of counter anions (X^{n-}), however, remains unchanged. This constant is broken by the forced oxidation of oxidation-sensitive green rust ($[Fe^{2+}{}_4Fe^{3+}{}_2(OH)_{12}]^{2+}(CO_3^{2-})\cdot 3H_2O$) to mössbauerite – an iron-only layered oxyhydroxide ($[Fe^{3+}{}_6O_4OH_8](CO_3^{2-})\cdot 3H_2O$).

The concept of this thesis comprises the following contentual parts:

- Synthesis of mössbauerite and application as electrocatalyst in the OER
  - Variation of the crystallinity and its influence on the activity
- The electronic structure of mössbauerite and its application in photoanodes
  - Increase in photocurrent at mössbauerite/WO_3 type II heterojunctions as deduced from the experimental and theoretical matching band positions
- Combined theoretical and experimental study on the structure of mössbauerite
  - Structural resemblance of mössbauerite with layered materials containing grafted anions in diffractometry and spectroscopy
  - Theoretical confirmation for the possibility of grafting in mössbauerite
  - Proposed refined structure of a turbostratic disordered and interstratified mössbauerite

4. Literature

1. Hall, P. J.; Bain, E. J., Energy-storage technologies and electricity generation. *Energy Policy* **2008,** *36* (12), 4352-4355.

2. Yekini Suberu, M.; Wazir Mustafa, M.; Bashir, N., Energy storage systems for renewable energy power sector integration and mitigation of intermittency. *Renewable and Sustainable Energy Reviews* **2014,** *35*, 499-514.

3. Kousksou, T.; Bruel, P.; Jamil, A.; El Rhafiki, T.; Zeraouli, Y., Energy storage: Applications and challenges. *Solar Energy Materials and Solar Cells* **2014,** *120*, 59-80.

4. Kåberger, T., Progress of renewable electricity replacing fossil fuels. *Global Energy Interconnection* **2018,** *1* (1), 48-52.

5. Tour, J. M.; Kittrell, C.; Colvin, V. L., Green carbon as a bridge to renewable energy. *Nature Materials* **2010,** *9*, 871.

6. Trancik, J. E., Back the renewables boom. *Nature* **2014,** *507* (7492), 300-302.

7. Schuur, E. A. G.; McGuire, A. D.; Schädel, C.; Grosse, G.; Harden, J. W.; Hayes, D. J.; Hugelius, G.; Koven, C. D.; Kuhry, P.; Lawrence, D. M.; Natali, S. M.; Olefeldt, D.; Romanovsky, V. E.; Schaefer, K.; Turetsky, M. R.; Treat, C. C.; Vonk, J. E., Climate change and the permafrost carbon feedback. *Nature* **2015,** *520*, 171.

8. Abas, N.; Kalair, A.; Khan, N., Review of fossil fuels and future energy technologies. *Futures* **2015,** *69*, 31-49.

9. Hoel, M.; Kverndokk, S., Depletion of fossil fuels and the impacts of global warming. *Resource and Energy Economics* **1996,** *18* (2), 115-136.

10. Yoon, J.; Sun, Y.; Rogers, J. A., Chapter 6 - Flexible Solar Cells Made of Nanowires/Microwires. In *Semiconductor Nanomaterials for Flexible Technologies*, Sun, Y.; Rogers, J. A., Eds. William Andrew Publishing: Oxford, 2010; pp 159-196.

11. Barber, J., Photosynthetic energy conversion: natural and artificial. *Chem. Soc. Rev.* **2009,** *38* (1), 185-196.

12. Blankenship, R. E.; Tiede, D. M.; Barber, J.; Brudvig, G. W.; Fleming, G.; Ghirardi, M.; Gunner, M. R.; Junge, W.; Kramer, D. M.; Melis, A.; Moore, T. A.; Moser, C. C.; Nocera, D. G.; Nozik, A. J.; Ort, D. R.; Parson, W. W.; Prince, R. C.; Sayre, R. T., Comparing Photosynthetic and Photovoltaic Efficiencies and Recognizing the Potential for Improvement. *Science* **2011,** *332* (6031), 805-809.

13. Ball, M.; Weeda, M., The hydrogen economy – Vision or reality?11This paper is also published as Chapter 11 'The hydrogen economy – vision or reality?' in Compendium of

Hydrogen Energy Volume 4: Hydrogen Use, Safety and the Hydrogen Economy, Edited by Michael Ball, Angelo Basile and T. Nejat Veziroglu, published by Elsevier in 2015, ISBN: 978-1-78242-364-5. For further details see: http://www.elsevier.com/books/compendium-of-hydrogen-energy/ball/978-1-78242-364-5. *International Journal of Hydrogen Energy* **2015,** *40* (25), 7903-7919.

14. Grahame, A.; Aguey-Zinsou, F., *Properties and Applications of Metal (M) dodecahydro-closo-dodecaborates (Mn=1,2B12H12) and Their Implications for Reversible Hydrogen Storage in the Borohydrides*. 2018; Vol. 6, p 106.

15. Xu, J.; Froment, G. F., Methane steam reforming, methanation and water-gas shift: I. Intrinsic kinetics. *AIChE Journal* **1989,** *35* (1), 88-96.

16. Bessarabov, D.; Millet, P., Chapter 2 - Key Performance Indicators. In *PEM Water Electrolysis*, Bessarabov, D.; Millet, P., Eds. Academic Press: 2018; pp 33-60.

17. Trasatti, S., Water electrolysis: who first? *J. Electroanal. Chem.* **1999,** *476* (1), 90-91.

18. Millet, P.; Grigoriev, S., Water electrolysis technologies. *Renewable Hydrogen Technologies: Production, Purification, Storage, Applications and Safety* **2013**, 19-41.

19. Volta, A., XVII. On the electricity excited by the mere contact of conducting substances of different kinds. In a letter from Mr. Alexander Volta, F. R. S. Professor of Natural Philosophy in the University of Pavia, to the Rt. Hon. Sir Joseph Banks, Bart. K.B. P. R. S. *Philosophical Transactions of the Royal Society of London* **1800,** *90*, 403-431.

20. Huggins, R. A., Hydrogen Storage. In *Energy Storage*, Huggins, R. A., Ed. Springer US: Boston, MA, 2010; pp 95-117.

21. Fujishima, A.; Honda, K., Electrochemical Photolysis of Water at a Semiconductor Electrode. *Nature* **1972,** *238* (5358), 37-38.

22. Zeng, K.; Zhang, D. K., Recent progress in alkaline water electrolysis for hydrogen production and applications. *Prog. Energy Combust. Sci.* **2010,** *36* (3), 307-326.

23. Fisher, A. C., *Electrode Dynamics*. Oxford University Press: 1996.

24. Bard, A. J.; Faulkner, L. R.; Leddy, J.; Zoski, C. G., *Electrochemical methods: fundamentals and applications*. wiley New York: 1980; Vol. 2.

25. Schmidt, T. J.; Gasteiger, H. A.; Stäb, G. D.; Urban, P. M.; Kolb, D. M.; Behm, R. J., Characterization of High-Surface-Area Electrocatalysts Using a Rotating Disk Electrode Configuration. *Journal of The Electrochemical Society* **1998,** *145* (7), 2354-2358.

26. Hong, W. T.; Risch, M.; Stoerzinger, K. A.; Grimaud, A.; Suntivich, J.; Shao-Horn, Y., Toward the rational design of non-precious transition metal oxides for oxygen electrocatalysis. *Energy & Environmental Science* **2015,** *8* (5), 1404-1427.

27. Chen, R.; Yang, C.; Cai, W.; Wang, H.-Y.; Miao, J.; Zhang, L.; Chen, S.; Liu, B., Use of platinum as the counter electrode to study the activity of nonprecious metal catalysts for the hydrogen evolution reaction. *ACS Energy Letters* **2017,** *2* (5), 1070-1075.

28. McCrory, C. C. L.; Jung, S.; Ferrer, I. M.; Chatman, S. M.; Peters, J. C.; Jaramillo, T. F., Benchmarking Hydrogen Evolving Reaction and Oxygen Evolving Reaction Electrocatalysts for Solar Water Splitting Devices. *Journal of the American Chemical Society* **2015,** *137* (13), 4347-4357.

29. Garcia, A. C.; Koper, M. T. M., Effect of Saturating the Electrolyte with Oxygen on the Activity for the Oxygen Evolution Reaction. *ACS Catalysis* **2018,** *8* (10), 9359-9363.

30. Kissinger, P. T.; Heineman, W. R., Cyclic voltammetry. *Journal of Chemical Education* **1983,** *60* (9), 702.

31. Dau, H.; Limberg, C.; Reier, T.; Risch, M.; Roggan, S.; Strasser, P., The mechanism of water oxidation: from electrolysis via homogeneous to biological catalysis. *ChemCatChem* **2010,** *2* (7), 724-761.

32. Man, I. C.; Su, H.-Y.; Calle-Vallejo, F.; Hansen, H. A.; Martínez, J. I.; Inoglu, N. G.; Kitchin, J.; Jaramillo, T. F.; Nørskov, J. K.; Rossmeisl, J., Universality in Oxygen Evolution Electrocatalysis on Oxide Surfaces. *ChemCatChem* **2011,** *3* (7), 1159-1165.

33. Shinagawa, T.; Garcia-Esparza, A. T.; Takanabe, K., Insight on Tafel slopes from a microkinetic analysis of aqueous electrocatalysis for energy conversion. *Scientific Reports* **2015,** *5*, 13801.

34. Doyle, R. L.; Lyons, M. E. G., An electrochemical impedance study of the oxygen evolution reaction at hydrous iron oxide in base. *Physical Chemistry Chemical Physics* **2013,** *15* (14), 5224-5237.

35. Lyons, M. E.; Doyle, R. L., Oxygen evolution at oxidised iron electrodes: a tale of two slopes. *International Journal of Electrochemical Science* **2012,** *7*, 9488-9501.

36. Cummings, C. Y.; Bonné, M. J.; Edler, K. J.; Helton, M.; McKee, A.; Marken, F., Direct reversible voltammetry and electrocatalysis with surface-stabilised Fe2O3 redox states. *Electrochemistry Communications* **2008,** *10* (11), 1773-1776.

37. Moir, J.; Soheilnia, N.; Liao, K.; O'Brien, P.; Tian, Y.; Burch, K. S.; Ozin, G. A., Activation of Ultrathin Films of Hematite for Photoelectrochemical Water Splitting via H2 Treatment. *ChemSusChem* **2015,** *8* (9), 1557-1567.

38. Montella, C., Discussion of the potential step method for the determination of the diffusion coefficients of guest species in host materials: Part I. Influence of charge transfer kinetics and ohmic potential drop. *J. Electroanal. Chem.* **2002,** *518* (2), 61-83.

39. Shi, Q.; Zhu, C.; Du, D.; Lin, Y., Robust noble metal-based electrocatalysts for oxygen evolution reaction. *Chem. Soc. Rev.* **2019,** *48* (12), 3181-3192.

40. Eftekhari, A., Tuning the electrocatalysts for oxygen evolution reaction. *Materials Today Energy* **2017,** *5*, 37-57.

41. Sanchez Casalongue, H. G.; Ng, M. L.; Kaya, S.; Friebel, D.; Ogasawara, H.; Nilsson, A., In Situ Observation of Surface Species on Iridium Oxide Nanoparticles during the Oxygen Evolution Reaction. *Angewandte Chemie International Edition* **2014,** *53* (28), 7169-7172.

42. Chandra, D.; Takama, D.; Masaki, T.; Sato, T.; Abe, N.; Togashi, T.; Kurihara, M.; Saito, K.; Yui, T.; Yagi, M., Highly Efficient Electrocatalysis and Mechanistic Investigation of Intermediate IrO x (OH) y Nanoparticle Films for Water Oxidation. *ACS Catalysis* **2016,** *6* (6), 3946-3954.

43. McCrory, C. C. L.; Jung, S.; Peters, J. C.; Jaramillo, T. F., Benchmarking Heterogeneous Electrocatalysts for the Oxygen Evolution Reaction. *Journal of the American Chemical Society* **2013,** *135* (45), 16977-16987.

44. Linsebigler, A. L.; Lu, G.; Yates, J. T., Photocatalysis on TiO2 Surfaces: Principles, Mechanisms, and Selected Results. *Chemical Reviews* **1995,** *95* (3), 735-758.

45. Hashimoto, K.; Irie, H.; Fujishima, A., TiO2 photocatalysis: a historical overview and future prospects. *Japanese journal of applied physics* **2005,** *44* (12R), 8269.

46. Scanlon, D. O.; Dunnill, C. W.; Buckeridge, J.; Shevlin, S. A.; Logsdail, A. J.; Woodley, S. M.; Catlow, C. R. A.; Powell, M. J.; Palgrave, R. G.; Parkin, I. P.; Watson, G. W.; Keal, T. W.; Sherwood, P.; Walsh, A.; Sokol, A. A., Band alignment of rutile and anatase TiO2. *Nature Materials* **2013,** *12*, 798.

47. Khan, S. U. M.; Al-Shahry, M.; Ingler, W. B., Efficient Photochemical Water Splitting by a Chemically Modified n-TiO₂. *Science* **2002,** *297* (5590), 2243-2245.

48. Hodes, G.; Cahen, D.; Manassen, J., Tungsten trioxide as a photoanode for a photoelectrochemical cell (PEC). *Nature* **1976,** *260* (5549), 312-313.

49. Salje, E.; Viswanathan, K., Physical properties and phase transitions in WO3. *Acta Crystallographica Section A* **1975,** *31* (3), 356-359.

50. Schieder, M.; Lunkenbein, T.; Martin, T.; Milius, W.; Auffermann, G.; Breu, J., Hierarchically porous tungsten oxide nanotubes with crystalline walls made of the metastable orthorhombic polymorph. *Journal of Materials Chemistry A* **2013,** *1* (2), 381-387.

51. Irie, H.; Miura, S.; Kamiya, K.; Hashimoto, K., Efficient visible light-sensitive photocatalysts: Grafting Cu(II) ions onto TiO2 and WO3 photocatalysts. *Chemical Physics Letters* **2008,** *457* (1), 202-205.

52. Santato, C.; Ulmann, M.; Augustynski, J., Enhanced Visible Light Conversion Efficiency Using Nanocrystalline WO3 Films. *Advanced Materials* **2001,** *13* (7), 511-514.

53. Low, J.; Yu, J.; Jaroniec, M.; Wageh, S.; Al-Ghamdi, A. A., Heterojunction Photocatalysts. *Advanced Materials* **2017,** *29* (20), 1601694.

54. Opoku, F.; Govender, K.; Gertina Catharina Elizabeth van Sittert, C.; Govender, P., *Recent Progress in the Development of Semiconductor-Based Photocatalyst Materials for Applications in Photocatalytic Water Splitting and Degradation of Pollutants*. 2017; Vol. 1.

55. Resasco, J.; Zhang, H.; Kornienko, N.; Becknell, N.; Lee, H.; Guo, J.; Briseno, A. L.; Yang, P., TiO2/BiVO4 nanowire heterostructure photoanodes based on type II band alignment. *ACS central science* **2016,** *2* (2), 80-88.

56. Lee, M. G.; Kim, D. H.; Sohn, W.; Moon, C. W.; Park, H.; Lee, S.; Jang, H. W., Conformally coated BiVO4 nanodots on porosity-controlled WO3 nanorods as highly efficient type II heterojunction photoanodes for water oxidation. *Nano Energy* **2016,** *28*, 250-260.

57. Cheng, B.-Y.; Yang, J.-S.; Cho, H.-W.; Wu, J.-J., Fabrication of an efficient BiVO4–TiO2 heterojunction photoanode for photoelectrochemical water oxidation. *ACS applied materials & interfaces* **2016,** *8* (31), 20032-20039.

58. Lima, L. V.; Rodriguez, M.; Freitas, V. A.; Souza, T. E.; Machado, A. E.; Patrocinio, A. O.; Fabris, J. D.; Oliveira, L. C.; Pereira, M. C., Synergism between n-type WO3 and p-type δ-FeOOH semiconductors: high interfacial contacts and enhanced photocatalysis. *Applied Catalysis B: Environmental* **2015,** *165*, 579-588.

59. Sivula, K.; Le Formal, F.; Gratzel, M., WO3-Fe2O3 Photoanodes for Water Splitting: A Host Scaffold, Guest Absorber Approach. *Chemistry of Materials* **2009,** *21* (13), 2862-2867.

60. Chen, J. Y. C.; Dang, L. N.; Liang, H. F.; Bi, W. L.; Gerken, J. B.; Jin, S.; Alp, E. E.; Stahl, S. S., Operando Analysis of NiFe and Fe Oxyhydroxide Electrocatalysts for Water Oxidation: Detection of Fe4+ by Mossbauer Spectroscopy. *Journal of the American Chemical Society* **2015,** *137* (48), 15090-15093.

61. Dionigi, F.; Strasser, P., NiFe-Based (Oxy)hydroxide Catalysts for Oxygen Evolution Reaction in Non-Acidic Electrolytes. *Advanced Energy Materials* **2016,** *6* (23), 1600621.

62. Gong, M.; Dai, H., A mini review of NiFe-based materials as highly active oxygen evolution reaction electrocatalysts. *Nano Research* **2015,** *8* (1), 23-39.

63. Song, F.; Hu, X., Exfoliation of layered double hydroxides for enhanced oxygen evolution catalysis. *Nature Communications* **2014,** *5*, 4477.

64. Vaysse, C.; Guerlou-Demourgues, L.; Delmas, C., Thermal evolution of carbonate pillared layered hydroxides with (Ni, L) (L=Fe, Co) based slabs: Grafting or nongrafting of carbonate anions? *Inorganic Chemistry* **2002,** *41* (25), 6905-6913.

65. Costa, D. G.; Rocha, A. B.; Souza, W. F.; Chiaro, S. S. X.; Leitao, A. A., Ab Initio Study of Reaction Pathways Related to Initial Steps of Thermal Decomposition of the Layered Double Hydroxide Compounds. *Journal of Physical Chemistry C* **2012,** *116* (25), 13679-13687.

66. Julien, C.; Massot, M.; Baddour-Hadjean, R.; Franger, S.; Bach, S.; Pereira-Ramos, J. P., Raman spectra of birnessite manganese dioxides. *Solid State Ionics* **2003,** *159* (3), 345-356.

67. Wang, B.; Bates, J. B.; Hart, F. X.; Sales, B. C.; Zuhr, R. A.; Robertson, J. D., Characterization of Thin-Film Rechargeable Lithium Batteries with Lithium Cobalt Oxide Cathodes. *Journal of The Electrochemical Society* **1996,** *143* (10), 3203-3213.

68. Singh, D., Characteristics and Effects of γ-NiOOH on Cell Performance and a Method to Quantify it in Nickel Electrodes. *Journal of the Electrochemical Society* **1998,** *145* (1), 116-120.

69. Faria, I. C.; Torresi, R.; Gorenstein, A., Electrochemical intercalation in NiOx thin films. *Electrochimica Acta* **1993,** *38* (18), 2765-2771.

70. Tedim, J.; Zheludkevich, M.; Salak, A.; Lisenkov, A.; Ferreira, M., Nanostructured LDH-container layer with active protection functionality. *Journal of Materials Chemistry* **2011,** *21* (39), 15464-15470.

71. Edenharter, A.; Breu, J., Applying the flame retardant LDH as a Trojan horse for molecular flame retardants. *Applied Clay Science* **2015,** *114*, 603-608.

72. Zubair, M.; Daud, M.; McKay, G.; Shehzad, F.; Al-Harthi, M. A., Recent progress in layered double hydroxides (LDH)-containing hybrids as adsorbents for water remediation. *Applied Clay Science* **2017,** *143*, 279-292.

73. Lv, L.; Yang, Z.; Chen, K.; Wang, C.; Xiong, Y., Electrocatalysts: 2D Layered Double Hydroxides for Oxygen Evolution Reaction: From Fundamental Design to Application (Adv. Energy Mater. 17/2019). *Advanced Energy Materials* **2019,** *9* (17), 1970057.

74. Khan, A. I.; O'Hare, D., Intercalation chemistry of layered double hydroxides: recent developments and applications. *Journal of Materials Chemistry* **2002,** *12* (11), 3191-3198.

75. Marappa, S.; Kamath, P. V., Water Molecules in Hydrotalcite-like Layered Double Hydroxides: Interplay between the Hydration of the Anions and the Metal Hydroxide Layer. *Zeitschrift Fur Anorganische Und Allgemeine Chemie* **2015,** *641* (5), 927-934.

76. Ramesh, T.; Jayashree, R.; Kamath, P. V., Disorder in layered hydroxides: DIFFaX simulation of the X-ray powder diffraction patterns of nickel hydroxide. *Clays and clay minerals* **2003,** *51* (5), 570-576.

77. Chen, J. Y. C.; Dang, L.; Liang, H.; Bi, W.; Gerken, J. B.; Jin, S.; Alp, E. E.; Stahl, S. S., Operando Analysis of NiFe and Fe Oxyhydroxide Electrocatalysts for Water Oxidation: Detection of Fe4+ by Mössbauer Spectroscopy. *Journal of the American Chemical Society* **2015,** *137* (48), 15090-15093.

78. Génin, J.-M. R.; Mills, S.; Christy, A.; Guérin, O.; Herbillon, A.; Kuzmann, E.; Ona-Nguema, G.; Ruby, C.; Upadhyay, C., Mössbauerite, $Fe^{3+6}O_4(OH)_8[CO_3]\cdot 3H_2O$, the fully oxidized 'green rust' mineral from Mont Saint-Michel Bay, France. *Miner. Mag.* **2014,** *78* (2), 447-465.

79. Génin, J.-M. R.; Ruby, C.; Upadhyay, C., Structure and thermodynamics of ferrous, stoichiometric and ferric oxyhydroxycarbonate green rusts; redox flexibility and fougèrite mineral. *Solid State Sciences* **2006,** *8* (11), 1330-1343.

80. Génin, J.-M. R.; Refait, P.; Bourrié, G.; Abdelmoula, M.; Trolard, F., Structure and stability of the Fe(II)–Fe(III) green rust "fougèrite" mineral and its potential for reducing pollutants in soil solutions. *Applied Geochemistry* **2001,** *16* (5), 559-570.

81. Génin, J.-M.; Christy, A.; Kuzmann, E.; Mills, S.; Ruby, C., Structure and occurrences of≪ green rust≫ related new minerals of the≪ fougérite≫ group, trébeurdenite and mössbauerite, belonging to the≪ hydrotalcite≫ supergroup; how Mössbauer spectroscopy helps XRD. *Hyperfine Interactions* **2014,** *226* (1-3), 459-482.

82. Génin, J.-M. R.; Guérin, O.; Herbillon, A.; Kuzmann, E.; Mills, S.; Morin, G.; Ona-Nguema, G.; Ruby, C.; Upadhyay, C., Redox topotactic reactions in FeII−III (oxy) hydroxycarbonate new minerals related to fougèrite in gleysols:"trébeurdenite and mössbauerite". *Hyperfine Interactions* **2012,** *204* (1-3), 71-81.

83. Génin, J.-M. R.; Aïssa, R.; Géhin, A.; Abdelmoula, M.; Benali, O.; Ernstsen, V.; Ona-Nguema, G.; Upadhyay, C.; Ruby, C., Fougerite and Fe II–III hydroxycarbonate green rust; ordering, deprotonation and/or cation substitution; structure of hydrotalcite-like compounds and mythic ferrosic hydroxide Fe (OH)(2+ x). *Solid State Sciences* **2005,** *7* (5), 545-572.

84. Mullet, M.; Khare, V.; Ruby, C., XPS study of Fe (II)□ Fe (III)(oxy) hydroxycarbonate green rust compounds. *Surface and Interface Analysis: An International Journal devoted to the development and application of techniques for the analysis of surfaces, interfaces and thin films* **2008,** *40* (3-4), 323-328.

85. Ruby, C.; Abdelmoula, M.; Naille, S.; Renard, A.; Khare, V.; Ona-Nguema, G.; Morin, G.; Génin, J.-M. R., Oxidation modes and thermodynamics of FeII–III oxyhydroxycarbonate green rust: dissolution–precipitation versus in situ deprotonation. *Geochimica et Cosmochimica Acta* **2010,** *74* (3), 953-966.

86. Misawa, T.; Hashimoto, K.; Shimodaira, S., The mechanism of formation of iron oxide and oxyhydroxides in aqueous solutions at room temperature. *Corrosion Science* **1974,** *14* (2), 131-149.

87. Srinivasan, R.; Lin, R.; Spicer, R. L.; Davis, B. H., Structural features in the formation of the green rust intermediate and γ-FeOOH. *Colloids and Surfaces A: Physicochemical and Engineering Aspects* **1996,** *113* (1-2), 97-105.

88. Mills, S. J.; Christy, A. G.; Génin, J.-M.; Kameda, T.; Colombo, F., Nomenclature of the hydrotalcite supergroup: natural layered double hydroxides. *Miner. Mag.* **2012,** *76* (5), 1289-1336.

89. Génin, J.-M.; Abdelmoula, M.; Aissa, R.; Ruby, C., Ordering in Fe II–III hydroxysalt green rusts from XRD and Mössbauer analysis (chloride, carbonate, sulphate, oxalate...); about the structure of hydrotalcite-like compounds. In *ICAME 2005*, Springer: 2006; pp 391-396.

90. Russell, M., Green rust: the simple organizing 'seed'of all life? *Life* **2018,** *8* (3), 35.

91. Halevy, I.; Alesker, M.; Schuster, E.; Popovitz-Biro, R.; Feldman, Y., A key role for green rust in the Precambrian oceans and the genesis of iron formations. *Nature Geoscience* **2017,** *10* (2), 135.

92. Hansen, H. C. B.; Koch, C. B.; Nancke-Krogh, H.; Borggaard, O. K.; Sørensen, J., Abiotic nitrate reduction to ammonium: key role of green rust. *Environmental Science & Technology* **1996,** *30* (6), 2053-2056.

93. Stöter, M.; Biersack, B.; Reimer, N.; Herling, M.; Stock, N.; Schobert, R.; Breu, J., Ordered Heterostructures of Two Strictly Alternating Types of Nanoreactors. *Chemistry of Materials* **2014,** *26* (18), 5412-5419.

94. Rajamathi, M.; Vishnu Kamath, P.; Seshadri, R., Polymorphism in nickel hydroxide: role of interstratification. *Journal of Materials Chemistry* **2000,** *10* (2), 503-506.

95. Bouessay, I.; Rougier, A.; Poizot, P.; Moscovici, J.; Michalowicz, A.; Tarascon, J.-M., Electrochromic degradation in nickel oxide thin film: A self-discharge and dissolution phenomenon. *Electrochimica Acta* **2005,** *50* (18), 3737-3745.

96. Deabate, S.; Henn, F., Structural modifications and electrochemical behaviour of the β (II)-Ni (OH) 2/β (III)-NiOOH redox couple upon galvanostatic charging/discharging cycling. *Electrochimica acta* **2005,** *50* (14), 2823-2835.

97. Hunter, B.; Winkler, J.; Gray, H., Iron is the active site in nickel/iron water oxidation electrocatalysts. *Molecules* **2018,** *23* (4), 903.

98. Burke, M. S.; Kast, M. G.; Trotochaud, L.; Smith, A. M.; Boettcher, S. W., Cobalt–iron (oxy) hydroxide oxygen evolution electrocatalysts: the role of structure and composition on activity, stability, and mechanism. *Journal of the American Chemical Society* **2015,** *137* (10), 3638-3648.

99. Friebel, D.; Louie, M. W.; Bajdich, M.; Sanwald, K. E.; Cai, Y.; Wise, A. M.; Cheng, M. J.; Sokaras, D.; Weng, T. C.; Alonso-Mori, R.; Davis, R. C.; Bargar, J. R.; Norskov, J. K.; Nilsson, A.; Bell, A. T., Identification of Highly Active Fe Sites in (Ni,Fe)OOH for Electrocatalytic Water Splitting. *Journal of the American Chemical Society* **2015,** *137* (3), 1305-1313.

5. Synopsis

The presented cumulative thesis consists of three manuscripts. The first two focus on the catalytic properties of the layered iron oxyhydroxide mössbauerite. Herein, mössbauerite was synthesized, characterized and employed as electrocatalyst in the oxygen evolution reaction for the production of molecular hydrogen. The third manuscript is a combined theoretical and experimental work on the structure of mössbauerite and other members of the fougèrite group that all consist of brucite layers separated by counter ions. Thereby, this work describes a possible transition of an academically developed catalyst into scalable and economically reasonable energy storage. The graphical synopsis is shown in Figure 10.

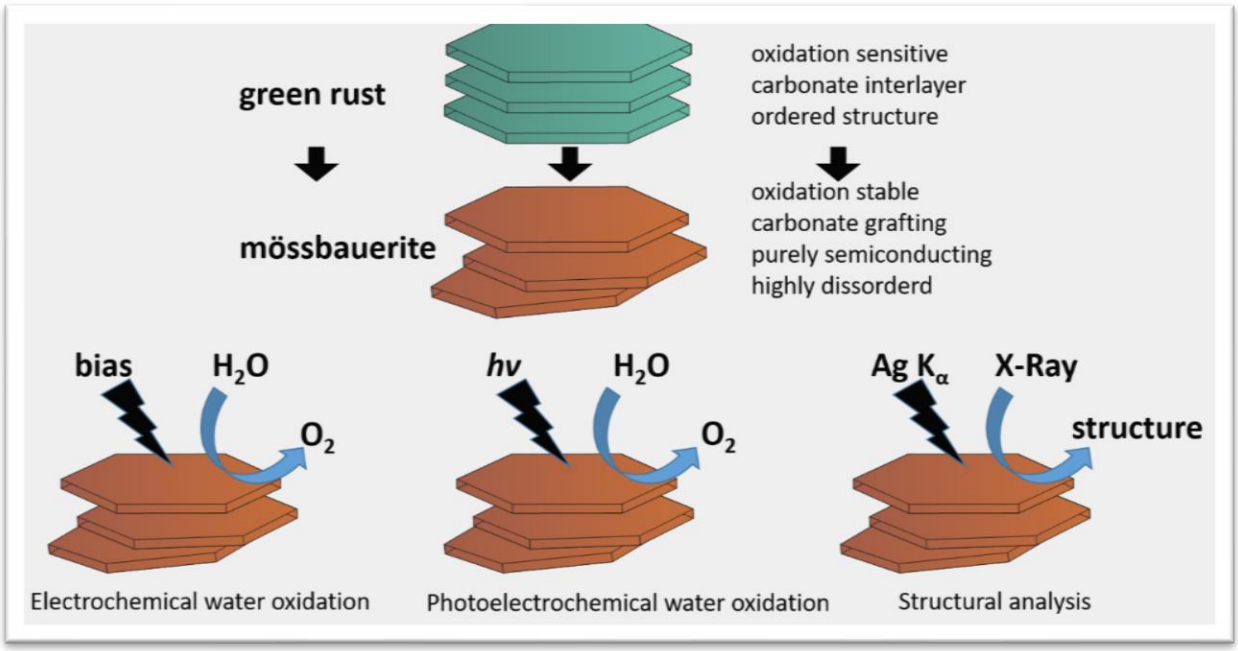

Figure 10: Graphical synopsis of this work containing the electrochemical, photoelectrochemical oxidation of water with mössbauerite and a structural analysis of the layered oxyhydroxide.

Chapter 6.1. describes the overall first employment of the iron-only layered oxyhydroxide mössbauerite as an electrocatalyst for the oxygen evolution reaction in basic media. During the work on the manuscript, it was found that the material shows purely semiconducting behavior and strong absorption in the visible range of light which are prerequisites for photoanode materials in the oxygen evolution reaction.

Therefore, the second manuscript, depicted in chapter 6.2., is a study about the electronic structure and the photoelectrochemical behavior of mössbauerite. After identifying the material as an n-type semiconductor with band positions that should allow improved charge separation at a heterojunction with WO_3, the combination of both materials was successfully employed as

photoanode in neutral media. During the work on these manuscripts, several inconsistencies were discovered regarding the structure of mössbauerite in comparison to LDHs from standard synthesis protocols.

These inconsistencies were investigated and confirmed by a combined computational and experimental approach as described in chapter 6.3. DFT+U calculations and Rietveld refinement were employed on synchrotron X-ray diffraction data to investigate the turbostratic disorder and interstratification of the layered mössbauerite. This investigation confirmed that mössbauerite is indeed a layered oxyhydroxide with partially grafted carbonate in the interlayer – resulting in a shrinkage of the *d*-spacing as the most distinctive structural feature.

Assuming the application of the iron-only layered oxyhydroxide in electrolyzers, electrochemical deposition of the material on steel plates in carbonate-containing solution was developed. Without the addition of cost-intensive chemicals, highly crystalline material was synthesized in direct contact on the conductive steel plates and applied as OER catalyst. Additionally, the influence of the steel composition, oxidation method and synthesis temperature on crystallinity, morphology, and activity was investigated.

5.1. Electrocatalytic Water Oxidation with an Iron-Only Layered Oxyhydroxide

In order to reduce the negative impact of greenhouse gas emissions on which the global energy economy is still highly dependent, carbon-free alternatives to fossil fuels are necessary. Hydrogen is currently considered a promising energy carrier that could be easily implemented as a partial replacement due to is unprecedented efficiency in *e.g.* fuel cells. However, a significant drawback that hinders is extensive usage at the moment is the cost-intensive hydrogen-production. Ideally, hydrogen is generated from water through electrolysis. High-performing, state-of-the-art catalysts are layered NiFe-based (oxy-)hydroxides where iron plays a crucial role. Our aim was to investigate an iron-only layered (oxy-)hydroxide as OER electrocatalyst that would be favorable since an iron-only catalyst would be non-toxic, earth-abundant and additionally an ideal model system to gain mechanistic insight in the role of iron during the OER.

Fougèrites are natural minerals that can be found under certain geological conditions and are the only LDHs where divalent and trivalent metal ions are of the same element – which is iron. The mineral green rust with the following sum formula $[Fe^{2+}_4Fe^{3+}_2(OH)_{12}]^{2+}$ $(CO_3)^{2-}$ is of transient nature and plays an important role in natural redox cycles and in the purification of aquifers. Aerial oxidation of this LDH results in a mixture of several ferric oxyhydroxide species such as goethite, feroxyhyte or lepidocrocite. Rapid oxidation, however, with a strong oxidant such as hydrogen peroxide preserves the layered structure. The additional charge that is generated by the oxidation to only ferric iron is compensated by deprotonation of a third if the hydroxide groups. The resulting material is phase-pure mössbauerite, an oxidation-stable ferric oxyhydroxide. This transition from green rust to mössbauerite resembles the electrochemical oxidation of α-$Ni(OH)_2$ to γ-NiOOH during the charging mechanism in batteries. The γ-phase of nickel suffers from self-discharge which proceeds via a reaction similar to the OER and therefore makes mössbauerite a promising electrocatalyst.

To test this hypothesis, carbonate-interlayered mössbauerite was synthesized via forced oxidation of carbonate interlayered green rust. Two different synthesis protocols were applied to yield samples of different crystallinity. The materials were thoroughly characterized by synchrotron high-energy X-ray diffraction, Mössbauer spectroscopy, thermogravimetric analysis and the sum formula $[Fe^{3+}_6O_4OH_8](CO_3^{2-})\cdot 3H_2O$ for mössbauerite was proposed. Interestingly and in contrast to all other iron oxyhydroxides, mössbauerite was shown to be an ordinary semiconductor with a band-gap in the visible region.

Finally, mössbauerite was evaluated as an electrocatalyst for the OER in basic media where iron is the active species and no synergistic effects can be present from other metals. Mössbauerite was synthesized according to two different synthesis procedures where the main difference is the reaction temperature, *i.e.* 50 °C and room temperature (RT). The material synthesized at 50 °C achieves an overpotential of 10 $mAcm^{-2}$ at an overpotential of 400 mV. The sample synthesized at RT requires a significantly higher overpotential of 540 mV. In iron-only electrocatalysts, the performance is usually hindered by conductivity limitations. Therefore, galvanostatic impedance spectroscopy at a current density of 2 $mAcm^{-2}$ was measured. In the sample synthesized at 50 °C, the total charge transfer resistance is significantly lower compared to the sample synthesized at RT, which strongly indicates a faster electron transfer. In catalysis in general, higher activity if often achieved by a higher surface area through micro-, meso-, or nanostructuring. BET measurements and the electrochemically active surface area, however, show that in this case, the material with the higher surface area is inferior due to its conductive limitations. The Tafel slope in the sample synthesized at 50 °C, is close to the theoretical value of 2.303RT/αF and in good agreement with previous work on bulk LDHs.

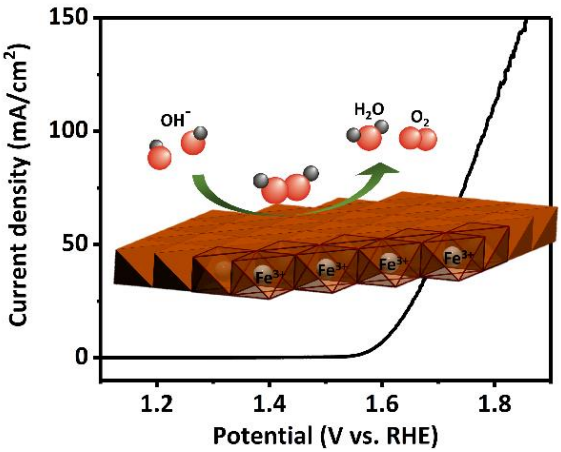

Figure 11: Schematic depiction of the oxygen evolution reaction in basic media at mössbauerite as electrocatalyst.

The stability of catalysts is besides activity the most important criteria. Iron oxyhydroxides are slightly soluble in basic media which could result in a transformation of mössbauerite to other iron oxyhydroxide species. To evaluate the stability of mössbauerite, the sample was investigated galvanostatically by applying a steady current of 0.0078 A which corresponds to a current density of 10 $mAcm^{-2}$. The necessary potential to sustain this current was recorded and showed an increase of 14 mV after 4 hours of constant hydrolysis. *Post-electrolysis* analysis of the material indicates, that some of the catalyst was dissolved during the experiment and reprecipitated as amorphous akaganeite. The layered structure of the material, however, was preserved as indicated by the still present sharp diffraction peak at 7.0 Å.

This work represents the first application of the oxidation stable iron-only layered oxyhydroxide mössbauerite as electrocatalyst for the oxygen evolution reaction. In addition to the catalysis, the structure of the material was investigated and similarities to grafted layered nickel phases were found. In-depth structural studies will be discussed in chapter 5.3 and 6.3. Whereas the semiconducting nature of mössbauerite, that was found by UV Vis diffuse reflectance spectroscopy and renders the material a promising candidate for the application in photochemistry, will be the topic of the following chapter.

5.2. Mössbauerite/WO_3 Heterojunction Photoanodes

As described in the previous chapter, energy conversion is essential for a sustainable energy economy based on non-carbonaceous forms of storage. Mössbauerite was shown to be an ordinary semiconductor with a band gap in the range of visible light. This can be exploited by the use of sunlight for the conversion of water to hydrogen. Since the sun provides approximately ten thousand times the power consumed by Earth's population during the same time, it is not only reasonable but necessary. Photoelectrochemical (PEC) water oxidation allows the conversion of solar energy. Two separate half-cell reactions need to be catalyzed in order to lower the overpotentials. Noble metals are employed to generate H_2 from protons at the cathode side, the oxygen evolution reaction, however, is more demanding since it proceeds via a coupled multistep electron transfer reaction. Oxidic n-type semiconducting materials have been in the focus of PEC research for energy storage. Pore hole transfer efficiency and low charge carrier mobility, however, decrease the performance significantly. The concept of OER co-catalysts has proven to be a promising approach to increase the activity/stability/efficiency significantly. A prerequisite for PEC water oxidation to gain an economically significant role, among other energy storage systems, would be a combination of materials that are highly efficient, highly stable, environmentally friendly and cheap. Since iron-based coatings have been shown to increase the photocurrent of several photoanodes significantly, we investigated mössbauerite as potential co-catalyst.

In this work, mössbauerite was characterized regarding its electronic and photoelectronic properties to evaluate its feasibility with monoclinic tungsten oxide. The chemical state of the layered iron (oxy-)hydroxide was analyzed for the first time with X-ray photoemission spectroscopy (XPS). In mössbauerite, all ferric cations are octahedrally coordinated with either O^{2-} or OH^- comparable to α-FeOOH goethite. Indeed, the Fe 2p region of the XP spectra is in close resemblance with data reported for goethite. Additionally, the O 1s spectrum of the sample shows peaks that can be assigned to both oxidic Fe-O and hydroxide Fe-OH in a ratio that is in close agreement with the sum formula proposed in chapter 6.1. The band positions of mössbauerite were determined with a combination of UV Vis diffuse reflectance spectroscopy (DRS) and Mott Schottky (MS) analysis. The flatband of mössbauerite was put at 0.34 V vs RHE whereas the positive slope in the MS plot shows that the material is an n-type semiconductor. The experimental results of the electronic structure were confirmed by quantum mechanics. The partial and total density of states projected on Fe 3d and O 2p in a DFT optimized structure confirm mössbauerite to exhibit semiconducting behavior. The band gap between spin-up valence band and spin-down conduction band is 1.8 V and therefore in

excellent agreement with the experimental results. A combination of mössbauerite with WO_3 – a standard material for photoanodes – would therefore yield a type-II heterojunction. The formation of such interfaces with the same type of semiconduction but different band edge positions has been shown to improve the charge separation and was therefore tested in PEC water oxidation experiments.

At first, mössbauerite was tested if the iron-only material itself produces significant photocurrent at low overpotentials which was not the case. Presumably due to low electronic conductivity and therefore high recombination rates. Therefore, neat WO_3 thin film electrodes with significant photocurrent (1.44 $mAcm^{-2}$ at 1.23 V vs RHE) were prepared. After functionalization of these photoanodes by electrophoretic deposition with mössbauerite, the heterojunction photoanode produces an increased photocurrent. The photocurrent of the WO_3/mössbauerite composite photoanode is among the highest reported for WO_3 photoanodes. Chronoamperometry at the thermodynamically necessary overpotential of 1.23 V vs RHE under interrupted illumination shows that the current density with mössbauerite was increased by 10% when compared to the neat WO_3 anode. In contrast to the similar ferrihydrite, which has been shown to act as hole storage layer, mössbauerite does not produce a cathodic overshoot when illumination is interrupted. Therefore, the increased photocurrent with mössbauerite originates from either improved charge carrier separation at the type II heterojunction or an improved hole collection efficiency since mössbauerite acts as an electrocatalyst itself.

In the course of this work, the electronic structure of mössbauerite was investigated from both an experimental and theoretical point of view. The band positions were determined with surprisingly good agreement and were successfully tested for PEC water oxidation in a combination with a highly active monoclinic WO_3 photoanode.

5.3. In-depth Study on the Structure of Iron-Only Layered (Oxy-)hydroxides

Chapter 4.1. and chapter 4.2. were focused on the synthesis, characterization, and application of the iron-only layered (oxy-)hydroxide mössbauerite. The synthesis of the material is based on the rapid oxidation of a 2:1 Fe^{2+}:Fe^{3+} LDH called green rust (or fougèrite) that is a member of the hydrotalcite group. As such it comprises of edge-sharing $Fe^{x+}(OH)_6$ where counter anions compensate the excess charge induced by ferric iron. During the rapid oxidation to mössbauerite however, there have been observed several changes in the material that would disqualify it as a member of the hydrotalcite group such as shrinkage of the interlayer spacing, deprotonation of hydroxyl groups and possible grafting of carbonate in the interlayer. Therefore, this systematic study on the structure of these two phases was conducted from both, a theoretic and an experimental approach combined.

Firstly, a unit cell for green rust with the sum formula $[Fe^{2+}{}_4Fe^{3+}{}_2(OH)_{12}]^{2+}(CO_3^{2-})\cdot 3H_2O$ has been adopted. Then grafting of carbonate to the brucite layers was simulated what led to a shrinkage of the *d*-spacing from 7.43 Å to 7.19 Å which is far from the experimentally found 7.53 Å. Additionally, the grafted structure was found to be significantly higher than non-grafted fougèrite. Therefore, grafting is highly unlikely in the mixed-valence form.

For mössbauerite with the proposed sum formula $[Fe^{3+}{}_6O_4(OH)_8]^{2+}(CO_3^{2-})\cdot 3H_2O$, there exist several possible configurations, depending on the distribution of hydrogen. A 5H/3H distribution was found to be energetically most stable by at least 32 $kJmol^{-1}$ compared to 6H/2H and 4H/4H and was used for the following calculations. Simulated patterns of grafted and non-grafted mössbauerite resulted in layer separations of 7.17 Å and 6.90 Å, respectively. The experimental *d*-spacing was found in between both which led us to the conclusion, that a mixture of both is present in the measured samples. Consequently, a quantitative Rietveld was calculated to match the experimental results by a mixture of turbostratically disordered stacks of grafted and non-grafted layers. Shifting the layers with $\Delta \neq 1/3$ to avoid creating supercells successfully resulted in a broadening of the Bragg peaks. Unfortunately, it was not possible to create a completely random sequence of grafted and non-grafted. This interstratification would avoid integral *00l* series, therefore the *002* Bragg peak was present in the refinement.

There are two possibilities for the grafting of carbonate to brucite layers: monodentate and bidentate. FTIR spectroscopy indicated, according to the splitting of the ν_3 band by 120 cm^{-2}, that a monodentate carbonate species is present. Monodentate grafted was also shown by the calculations to be plausible at the reaction temperature of 50 °C and with excess hydrogen peroxide for the oxidation from green rust to mössbauerite. Bidentate grafting would require

significantly more energy and is inhibited under the reaction conditions. Energy profiles for the grafting process have been calculated where HCO_3^- plays an important role, but the driving force for the grafting process remains unclear at this moment. The transformation of fougèrite to mössbauerite, however, proceeds exothermically with a reaction energy of -154 $kJmol^{-1}$ and once the grafted mössbauerite is formed, it is reasonable to assume that the grafted surface is kinetically stable.

6. Results

6.1. Electrocatalytic Water Oxidation with an Iron-Only Layered Oxyhydroxide

Michael Ertl,[†,+] Corina Andronescu,[‡,+] Jonathon Moir,[§,+] Mirijam Zobel,[‖] Friedrich E. Wagner,[«] Stefan Barwe,[‡] Geoffrey Ozin,[*,§] Wolfgang Schuhmann,[*,‡] and Josef Breu[*,†]

Oxygen Evolution Catalysis with Mössbauerite – A Trivalent Iron-only Layered Double Hydroxide

Published: *Chemistry – A European Journal* **2018**, *24*, 9004-9008.
Reprinted with permission, Copyright (2018) John Wiley and Sons.
Impact Factor (2018) Chem. Eur. J.: 5.16
https://doi.org/10.1002/chem.201801938

† Bavarian Polymer Institute and Department of Chemistry, University of Bayreuth, Universitätsstr. 30, 95440 Bayreuth, Germany
‡ Analytical Chemistry – Center for Electrochemical Sciences, Ruhr-University Bochum, Universitätsstr. 150, 44780 Bochum, Germany
§ Department of Chemistry, University of Toronto, 80 St. George Street, M5S3H6 Toronto, Canada
‖ Solid State Chemistry – Mesostructured Materials, University of Bayreuth, Universitätsstr. 30, 95440 Bayreuth, Germany
« Physics Department e15, Technical University Munich, 85748 Garching, Germany

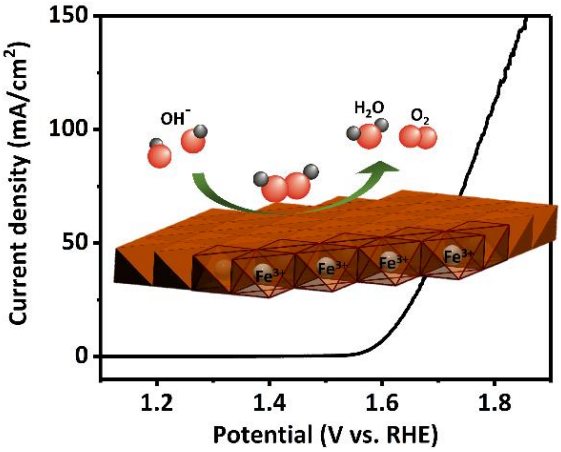

Individual Contributions:

The concept of the publication was developed by myself, Jonathon Moir and Prof. Geoffrey Ozin. The manuscript was written by myself and Prof. Josef Breu with contribution from the other co-authors. Initial experiments for the electrocatalytic water oxidation were performed by Jonathon Moir and myself. The synthesis and most characterization of the catalysts were done by myself. Prof. Corina Andronescu performed most of the electrochemical experiments. Prof. Friedrich Wagner performed the Mössbauer spectroscopy. Prof. Mirijam Zobel helped with the synchrotron measurements and the data interpretation. Stefan Barwe helped with the electrochemical experiments. Prof. Wolfgang Schuhmann and Prof. Geoffrey Ozin helped with the interpretation of the results in the manuscript.

ChemPubSoc Europe
DOI: 10.1002/chem.201801938
CHEMISTRY A European Journal
Communication

Layered compounds

Oxygen Evolution Catalysis with Mössbauerite—A Trivalent Iron-Only Layered Double Hydroxide

Michael Ertl+,[a] Corina Andronescu+,[b] Jonathon Moir+,[c] Mirijam Zobel,[d] Friedrich E. Wagner,[e] Stefan Barwe,[b] Geoffrey Ozin,*[c] Wolfgang Schuhmann,*[b] and Josef Breu*[a]

Abstract: Mössbauerite is investigated for the first time as an "iron-only" mineral for the electrocatalytic oxygen evolution reaction in alkaline media. The synthesis proceeds via intermediate mixed-valence green rust that is rapidly oxidized in situ while conserving the layered double hydroxide structure. The material catalyzes the oxygen evolution reaction on a glassy carbon electrode with a current density of 10 mA cm^{-2} at 1.63 V versus the reversible hydrogen electrode. Stability measurements, as well as post-electrolysis characterization are presented. This work demonstrates the applicability of iron-only layered double hydroxides as earth-abundant oxygen evolution electrocatalysts. Mössbauerite is of fundamental importance since as an all Fe^{3+} material its performance has no contributions from unknown synergistic effects as encountered for mixed valence Co/Ni/Fe LDH.

The high overpotential of the oxygen evolution reaction (OER) represents the critical issue in electrocatalytic water splitting, which ideally should be tackled by base metal oxides or (oxy)-hydroxide catalysts.[1–5] In particular, NiFe-based (oxy)hydroxides and layered double hydroxides (LDH) have been shown to be among the most active OER catalysts in alkaline electrolyte solutions; the best even surpassing state-of-the-art noble-metal oxides.[6–8] Iron was shown to play a crucial role which, however, is not yet fully understood. Trotochaud et al. hypothesized that the activation is due to a Ni-Fe partial charge transfer.[9]

Fougèrites are abundant natural minerals found under specific geological conditions (low *T*, moderate CO_2 fugacity, alkaline pH).[10,11] Minerals of the fougèrite group are the only members of the hydrotalcite (LDH) supergroup where divalent and trivalent cations are of the same element (iron).[12] The mixed-valence mineral green rust (idealized formula $Fe_4^{2+}Fe_2^{3+}(OH)_{12}CO_3{\cdot}3H_2O$) is found in large quantities in maritime marshes in northern France (Figure 1 A). Green rusts have been intensively studied by geologists and typically show a greenish-blue color, which is transient due to the propensity of Fe^{2+} towards oxidation. Green rust plays an important role in the natural purification of aquifers and reduces nitrate to molecular nitrogen.[13,14]

Upon aerial oxidation the material usually transforms into a variety of ferric oxyhydroxides like goethite, feroxyhyte, and lepidocrocite.[15,16] Additionally, in a narrow zone around green rust some 16–31 % are transformed in a topotactic conversion into an all-ferric compound, named mössbauerite (idealized formula $Fe_6^{3+}(O)_4(OH)_8CO_3{\cdot}3H_2O$).[10] Charge compensation upon oxidation is achieved by partial deprotonation whilst the interlayer carbonate remains in the structure. The natural process can be mimicked in the laboratory by a one-step oxidation of synthetic green rust by the use of hydrogen peroxide, resulting in phase-pure mössbauerite.[17,18]

The conversion can be observed by the naked eye by the abrupt change in the color from green-blue to brownish red (Figure 1 B). The topotactic nature of this oxidation process is evident from the retention of the hexagonal platelet morphology of the precursor green rust in the product mössbauerite.[17]

The conversion of green rust to mössbauerite resembles the electrochemical oxidation of α-$Ni(OH)_2$ to γ-NiOOH.[19,20] This conversion has been intensively studied by battery technologists in the context of Ni-based alkaline secondary batteries. While the α-/γ-couple delivers more than 100 % charge storage capacity, it unfortunately suffers from a high self-discharge rate.[21,22] This self-discharge is related to the catalysis of the OER by the charged phase, γ-NiOOH.

[a] M. Ertl,+ Prof. Dr. J. Breu
Bavarian Polymer Institute and Department of Chemistry
University of Bayreuth, Universitätsstr. 30
95440 Bayreuth (Germany)
E-mail: josef.breu@uni-bayreuth.de

[b] Dr. C. Andronescu,+ Dr. S. Barwe, Prof. Dr. W. Schuhmann
Analytical Chemistry—Center for Electrochemical Sciences
Ruhr-University Bochum, Universitätsstr. 150
44780 Bochum (Germany)
E-mail: wolfgang.schuhmann@rub.de

[c] Dr. J. Moir,+ Prof. Dr. G. Ozin
Department of Chemistry, University of Toronto
80 St. George Street, M5S3H6, Toronto (Canada)
E-mail: gozin@chem.utoronto.ca

[d] Prof. Dr. M. Zobel
Solid State Chemistry—Mesostructured Materials
University of Bayreuth, Universitätsstr. 30
95440 Bayreuth (Germany)

[e] Prof. Dr. F. E. Wagner
Physics Department e15, Technical University Munich
James-Franck-Str., 85748 Garching (Germany)

[+] These authors contributed equally to this work.

Supporting information and the ORCID identification number(s) for the author(s) of this article can be found under: https://doi.org/10.1002/chem.201801938.

© 2018 Wiley-VCH Verlag GmbH & Co. KGaA, Weinheim

ChemPubSoc Europe

CHEMISTRY A European Journal Communication

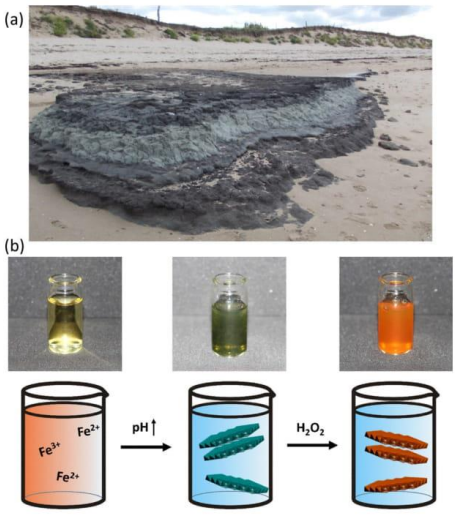

Figure 1. (a) Natural green rust deposit at the beach of northern Brittany. (b) Synthesis of mössbauerite by in situ oxidation of green rust. A mixture of Fe^{2+} and Fe^{3+} salts is precipitated by increasing the pH in an oxygen-free atmosphere. Consecutively, the precipitating green rust is oxidized by hydrogen peroxide.

More recently, Fe-substituted γ-$Ni_{1-x}Fe_xOOH$ was reported to be 500 times more active for OER in alkaline media as their pure Ni and Fe parent compounds.[23] By operando X-ray absorption measurements, moreover, the Ni-sites were shown not to be active sites in the OER. In contrast to the OER, Scavetta et al. reported that for the electrochemical oxidation of glucose, the Fe sites in $Ni^{II}_3Fe^{III}$-LDHs were found not to be electroactive whilst influencing the electroactivity of Ni sites by shifting the redox potential to less anodic values and by increasing the percentage of electroactive Ni sites.[24] Since NiFe-LDHs are structurally closely related to γ-NiOOH by having the same brucite type layers (which for LDH carry a positive charge), this contradiction strongly suggests that a deeper understanding of the crucial role of Fe is needed.

In this communication, we synthesized mössbauerite, a trivalent iron-only compound with the structure of LDHs. Having a defined material containing only iron is of great importance for understanding OER catalysts. Investigations of a pure phase, with no synergistic effects between different metals, are possible. The iron-only electrocatalyst for the OER furthermore possesses the potential to replace other catalysts comprising less abundant, more expensive, or higher toxicity catalysts. Moreover, mössbauerite represents a missing link between γ-NiOOH and LDHs, in as much as it represents an (oxy)hydroxide like in γ-NiOOH but the brucite type layers are positively charged as for LDHs.

The co-precipitation with Na_2CO_3 of a 2:1 mixture of ferrous and ferric chloride, dissolved in Ar-saturated water, yielded carbonate-interlayered green rust with a *d*-spacing of 7.5 Å, as evidenced by powder X-ray diffraction (XRD, Figure S1 A in Supporting Information). The 00*l* series of green rust is integral, indicating a well-defined, regular basal spacing. To vary the crystallinity, the synthesis was conducted at room temperature (RT) following literature procedures,[18,25] and also at elevated temperature (50 °C).

Upon addition of hydrogen peroxide, the color of the crystals change to brownish-red and phase-pure mössbauerite is obtained, labeled **M** and **M-50** for RT and 50 °C synthesized samples, respectively. Details of the synthesis procedure are in the Supporting Information.

Not surprising for a layered compound, the diffractogram (Figure 2, Figure S1 B) is rather featureless, indicating turbostratically disordered stacking of adjacent layers. The few peaks observed are labeled according to Génin et al.[10] A sharp

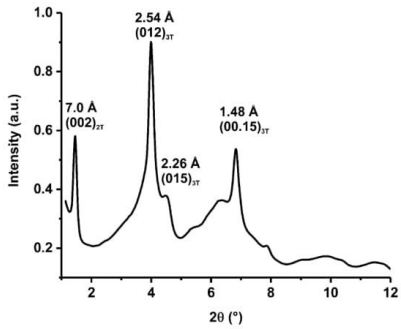

Figure 2. Synchrotron X-ray diffraction data of **M-50**, indexed according to Génin et al.[10] The *d*-spacing is 7.0 Å ($2\theta = 1.45°$), corresponding to the basal distance of the 2T polytype of mössbauerite ($\lambda = 0.1771$ Å).

peak at $2\theta = 1.45°$ (002) corresponds to the basal distance of what Génin et al. indexed as the 002 reflex of the 2T polytype.[10] No integral 00*l* series of the 2T polytype is observed, neither in this work, nor by Génin et al., indicating that the layers are stacked with slightly varying basal spacing (interstratification). For γ-Ni-oxyhydroxide a comparable basal spacing of 6.9 Å was reported,[20,26] whereas for α-Ni-oxyhydroxide a slightly larger basal spacing of 7.5 Å was reported,[27] which is more in the line with other carbonate-LDHs (typically 7.5 Å),[28] and with that of green rust (7.5 Å). Gravimetric analysis of the interlayer carbonate content as $BaCO_3$[29] indicates a lower carbonate content of **M** and **M-50** as compared to the idealized formula. Assuming that charge neutrality is assured by adjusting the O^{2-}/OH^- ratio through deprotonation, the following formula can be given for these synthetic mössbauerites: $Fe_6^{3+}(O)_{4.4}(OH)_{7.6}(CO_3)_{0.8}\cdot 3H_2O$. Within experimental error, both **M-50** and **M** have the same formula. Upon thermal decomposition of mössbauerite to produce hematite, a total mass loss of 21 wt.% (**M-50**) and 22 wt.% (**M**), due to loss of H_2O and CO_2, was observed (Figure S2), which is in close agreement to what is expected from this formula (24.7 wt.%).

At both temperatures, hexagonally-shaped platy crystals are obtained. At 50 °C the crystals are, however, more uniform,

© 2018 Wiley-VCH Verlag GmbH & Co. KGaA, Weinheim

ChemPubSoc Europe

CHEMISTRY A European Journal Communication

larger, and show sharper edges (Figure 3 and Figure S3). The morphology of green rust and mössbauerite are very similar (Figure 3 and Figure S3 D), indicating a topotactic conversion as previously suggested by Génin et al.[30] The disordered crystals are approximately hexagonal prisms with large aspect ratio of >20. The thickness of the platy crystals is 20 nm on average in both samples, **M** and **M-50**, as derived from TEM images and by means of AFM (Figure S4 in Supporting Information). In both mössbauerite samples, the interlayer anion is carbonate, as evidenced by FTIR (Figure S5). Of course, many other mixed valence Fe-containing LDHs containing various amounts of for example, Co and Ni, have been studied previously where iron has been shown to be the active center.[31] Mössbauerite is, however, an iron-only LDH with solely trivalent iron, and for which charge balance upon oxidation is achieved by partial deprotonation of the structural hydroxyl ions. The exclusion of other metals and potential synergistic effects will render fundamental studies about intermediates and intermediate oxidation states of iron easier.

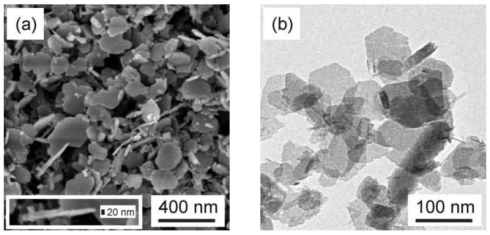

Figure 3. (a) SEM and (b) TEM images of **M-50** displaying thin, hexagonally-shaped platelets. Typical platelet diameters in the range of 50–200 nm are observed, while the SEM image suggests thin platelets of <10 nm thickness.

Interestingly, contrary to the other known iron (oxy)hydroxides, mössbauerite is an ordinary semiconductor, with no localized transitions observable, but with a band-gap of 2.4 eV (Figure S6). Mössbauer spectra of **M** and **M-50** are very similar (Figure S7). At RT the ^{57}Fe spectra consist of a single, broad doublet with a mean quadrupole splitting of 0.69 mm s^{-1} and an isomer shift of 0.38 mm s^{-1} with respect to metallic iron. At 4.2 K a sextet pattern with broad lines, a hyperfine field of 49.4 T, and a very small electric quadrupole interaction of only −0.09 mm s^{-1} is observed. These values agree well with those expected for mössbauerite.[10,32] Clearly, no residual ferrous doublet was observed in the RT spectra, indicating complete oxidation to ferric iron in both mössbauerite samples. The specific surface area of the two samples were determined by the Brunauer–Emmett–Teller method (BET).[33] Sample **M** has a surface area of 105 m^2 g^{-1} whereas sample **M-50** has a slightly lower surface area of 86 m^2 g^{-1} (Figure S8, Table S1).

Inspired by the analogy to γ-NiOOH, the mössbauerite was evaluated as an electrocatalyst for the OER. Mössbauerite as an iron-only LDH, is the only material where the brucite type layers, as found in γ-NiOOH and LDHs, are realized by only ferric iron ions. Moreover, by X-ray analysis no other iron (oxy)-hydroxides were observed. Therefore, this material could serve as ideal catalyst to study the OER reaction in depth without synergistic effects. **M-50** achieves a current density of 10 mA cm^{-2} at an applied potential of 1.63 V versus the reversible hydrogen electrode (RHE), whereas **M** requires a much higher potential of 1.77 V versus RHE (Figure 4). The overpotentials of the two mössbauerites differ significantly (540 mV and 400 mV, respectively, for **M** and **M-50**) indicating that there might be plenty of room for further improvement by varying synthesis conditions. The **M-50** overpotential is, however, already comparable to the best values reported in the literature for thoroughly optimized iron-only based catalysts.[34,35] Since there is plenty of space for optimization of the synthesis, for example, with respect to crystallinity and microstructure, we expect that lower overpotentials should become accessible for the OER.

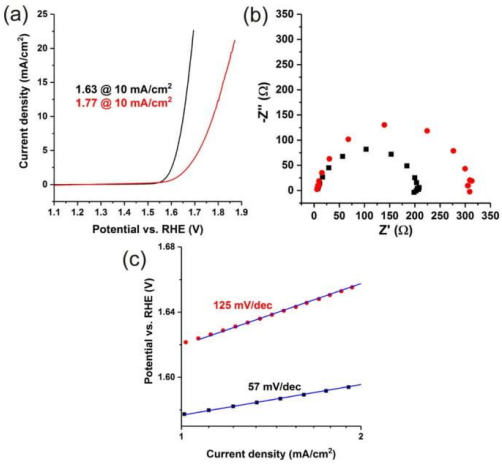

Figure 4. Electrochemical data of **M-50** (black) and **M** (red). (a) Linear sweep voltammograms registered at 5 mV s^{-1} (b) Nyquist plots registered under oxygen evolution at 0.156 mA (2 mA cm^{-2}) (c) Tafel slopes calculated from LSV.

The performance of iron-only based catalysts is considered to be closely related to the conductivity limitations of these materials.[36,37] Mass activities (mA μg^{-1}) were determined by measuring linear sweep voltammograms (LSV) for **M-50**, using different mass loadings (0.1, 0.125, 0.25, and 0.5 mg cm^{-2}). The highest catalytic activity was found for 0.25 mg cm^{-2} (Figure S9 in Supporting Information). Despite the semi-conducting nature of mössbauerite, a maximum is observed suggesting that after complete coverage of the electrode, conductivity of grain boundaries limits the activity.

Since due to the high local concentration of H_2O, the OER current is not limited by mass transport, the LSV at sufficiently slow scan rates represents the current increase with increasing driving force diminished by potential Ohmic drop due to electron-transfer resistance such as, for example, that caused by

 © 2018 Wiley-VCH Verlag GmbH & Co. KGaA, Weinheim

ChemPubSoc Europe

CHEMISTRY A European Journal Communication

inter-particle electron transfer. Hence, the LSV slope is considered to provide a hint on the intrinsic conductivity of a catalyst layer. The difference in the slope of the LSVs furthermore indicates a difference in the electrical conductivity of the two mössbauerites, which can explain the OER activity difference of both materials.

Galvanostatic electrochemical impedance spectroscopy at a current density of 2 mA cm^{-2} was performed. The total charge transfer resistance evaluated from the Nyquist plots is significantly lower for **M-50** compared to **M**, indicating a faster electron transfer of the oxygen evolution reaction on **M-50** than on **M**, which can also induce the differences observed in the LSVs. (Figure S10, Table S2).

Electrochemically active surface areas were additionally evaluated from the electrochemical impedance spectra, following a procedure by McCrory et al.[38] The **M** to **M-50** electrochemical surface areas ratio is 1.83 (Table S2), exhibiting a similar trend to the BET surface areas, where a higher surface area was determined for **M** than for **M-50**. The Tafel slopes of both catalysts were investigated in the range of 1 to 2 mA cm^{-2} current densities. The Tafel slope observed for **M-50** is much smaller than that of **M** (57 and 125 mV dec^{-1}, respectively). For iron-only catalysts, previous work conducted by Lyons and Doyle reported values ranging from 40 to 60 mV dec^{-1} in the low overpotential region to 120 mV dec^{-1} in the high overpotential region.[39] These differences were attributed to the formation of dissimilar FeOOH films on the iron electrode as a consequence of the different cycling methods used.[39] The **M-50** Tafel slope of 57 mV dec^{-1} is close to the theoretical value of $2.303RT/\alpha F$ (F—Faraday constant, T—temperature, R—universal gas constant, α—transfer coefficient) and is also in good agreement with previous results from bulk LDHs.[7] For **M-50**, the calculated Faradaic efficiency is 94% (Figure S11) which is in good agreement with values reported for base metal catalysts in 1 M basic electrolyte.[38]

Beside activity, catalyst stability, especially during the application of high anodic potentials required for the OER, is equally important. Moreover, the slight solubility of iron oxyhydroxides in basic media could lead to re-precipitation of FeOOH on the electrode surface. Hence, it needs to be ruled out that this is responsible for the observed electrocatalytic activity. We recorded LSVs for the same electrode before and after conditioning. A slightly increased activity was observed after the conditioning process which can be induced by the modification of the catalyst surface in contact with the electrolyte (Figure S12 in Supporting Information).

Different protocols have been established in literature to evaluate catalyst stability.[37,38,40] McCrory et al. employed controlled-current electrolysis for 2 h and a change of 0.03 V in the registered potential was used as criteria to determine the catalyst stability.[38]

Following the reported protocol, we investigated the stability of **M-50** galvanostatically by applying a current of 0.0078 A (corresponding to a current density of 10 mA cm^{-2}) for 4 h in 1 M KOH. During this time, the necessary overpotential to sustain this current was recorded. An increase of the potential by 0.014 V was registered after 4 h electrolysis (Figure 5 A). The recorded relatively small change of the potential could be caused by different factors, like activity loss of the catalyst or its physical detachment from the electrode surface. SEM images of the electrode after the 4 h electrolysis show that the catalyst is still present on the electrode surface, but not as homogeneously distributed, which could indicate a partial loss of the catalyst (Figure S13). The EDX spectrum indicates that iron is the only metal present on the electrode surface (Figure S13).

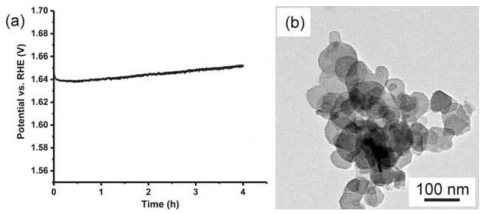

Figure 5. Stability test and post-electrolysis characterization of **M-50**. (a) Chronoamperometric measurement of **M-50** in 1 M KOH at 10 mA cm^{-2}. (b) TEM image of **M-50** after 4 h long term measurement (**M-50 4 h**) displaying thin platelets.

Post-electrolysis characterization of the catalyst shows that the platelet morphology is maintained throughout the stability test (Figure 5 B). The edges of the hexagonal platelets were, however, rounded. This might indicate a partial dissolution and re-precipitation of the catalyst during long-term operation. The post-electrolysis diffractogram of **M-50** showed little change (Figure S14). Most importantly, the sharp peak at $2\theta = 1.45^\circ$ is still clearly present. The basal spacing of the layered structure has not been modified, as would be expected if the composition of the interlayer space would have changed throughout the long term stability measurement. Some additional sharp reflections are observed that can be assigned to $KHCO_3$. The broad reflection at $\approx 2\theta = 2^\circ$ ($d = 5.3$ Å) could indicate the presence of small amounts of akaganeite ($d_{020} = 5.3$ Å, PDF# 00-034-1266). It is, however, very unlikely that this trace impurity significantly contributes to the activity of the mössbauerite catalyst, in particular since akaganeite was reported to exhibit low catalytic activity for the OER.[41]

In conclusion, we have synthesized an iron-only mössbauerite with LDH structure that shows considerable activity for the OER. The synthesis proceeds by fast oxidation of the labile precursor, green rust. The LDH structure is preserved throughout the oxidation process resulting in carbonate-interlayered LDHs. By simply varying the synthesis temperature the performance of the mössbauerite as an oxygen evolution electrocatalyst could already be drastically improved in this work. This indicates that a thorough systematic optimization of the dependence of the oxygen evolution activity on the size, shape, and crystallinity of the materials could yield a highly efficient electrocatalyst for oxidizing water. For the material synthesized at 50 °C, a current density of 10 mA cm^{-2} was recorded at an overpotential of 400 mV versus RHE, with an initial Tafel slope of 57 mV dec^{-1}. Morphology, doping, and processing method of the catalyst, electrolyte, type of electrodes etc. have a pro-

 © 2018 Wiley-VCH Verlag GmbH & Co. KGaA, Weinheim

ChemPubSoc Europe

CHEMISTRY A European Journal Communication

nounced influence on performance data and make comparison difficult. Nevertheless, **M-50** is among the best iron-based OER catalysts (Table S3 in Supporting Information).

A slight change of the catalyst is noticed after a 4 h stability test, but without a negative impact on the potential required to generate a current density of 10 mA cm^{-2}. Besides good activity, the iron-only LDH mössbauerite offers the opportunity to investigate the OER of iron LDHs without synergistic effects from other transition metals. The mixed valence intermediate green rust, with ferrous and ferric iron, will moreover allow doping with a variety of transition metal ions while preserving the brucite-type structure of LDHs. This compositional flexibility will enable expansion and enrichment of the application opportunities of mössbauerite by material chemists; a naturally occurring material, which has so far been the exclusive playground for mineralogists and geologists.

Acknowledgements

J.B. is grateful to the Deutsche Forschungsgemeinschaft (DFG) in the framework of the SFB 840. M.E. thanks the Hanns-Seidel foundation for a doctoral scholarship. We thank Prof. J.-M. R. Génin for the photograph of natural green rust used in Figure 1. Beamtime at the European Synchrotron Radiation Facility (ESRF, ID31) is gratefully acknowledged. G.A.O. is a Government of Canada Research Chair in Materials Chemistry and Nanochemistry. Financial support for this work was provided by the Ministry of the Environment and Climate Change; Connaught Global Challenge Fund; and the Natural Sciences and Engineering Research Council of Canada (NSERC). W.S. is grateful to the DFG in the framework of the cluster of excellence "RESOLV", EXC 1069.

Conflict of interest

The authors declare no conflict of interest.

Keywords: all-iron layered double hydroxide · electrochemistry · heterogeneous catalysis · oxygen evolution reaction · water splitting

[1] Q. Wang, L. Shang, R. Shi, X. Zhang, Y. F. Zhao, G. I. N. Waterhouse, L. Z. Wu, C. H. Tung, T. R. Zhang, *Adv. Energy Mater.* **2017**, *7*, 1700467.
[2] Y. F. Zhao, X. D. Jia, G. B. Chen, L. Shang, G. I. N. Waterhouse, L. Z. Wu, C. H. Tung, D. O'Hare, T. R. Zhang, *J. Am. Chem. Soc.* **2016**, *138*, 6517–6524.
[3] Y. X. Zhao, C. Chang, F. Teng, Y. F. Zhao, G. B. Chen, R. Shi, G. I. N. Waterhouse, W. F. Huang, T. R. Zhang, *Adv. Energy Mater.* **2017**, *7*, 1700005.
[4] P. F. Liu, S. Yang, B. Zhang, H. G. Yang, *ACS Appl. Mater. Interfaces* **2016**, *8*, 34474–34481.
[5] R. Liu, Y. Y. Wang, D. D. Liu, Y. Q. Zou, S. Y. Wang, *Adv. Mater.* **2017**, *29*, 1701546.
[6] F. Dionigi, P. Strasser, *Adv. Energy Mater.* **2016**, *6*, 1600621.
[7] F. Song, X. Hu, *Nat. Commun.* **2014**, *5*, 4477.
[8] M. Gong, Y. Li, H. Wang, Y. Liang, J. Z. Wu, J. Zhou, J. Wang, T. Regier, F. Wei, H. Dai, *J. Am. Chem. Soc.* **2013**, *135*, 8452–8455.
[9] L. Trotochaud, S. L. Young, J. K. Ranney, S. W. Boettcher, *J. Am. Chem. Soc.* **2014**, *136*, 6744–6753.
[10] J.-M. R. Génin, S. Mills, A. Christy, O. Guérin, A. Herbillon, E. Kuzmann, G. Ona-Nguema, C. Ruby, C. Upadhyay, *Mineral. Mag.* **2014**, *78*, 447–465.
[11] S. Drissi, P. Refait, M. Abdelmoula, J.-M. R. Génin, *Corros. Sci.* **1995**, *37*, 2025–2041.
[12] J.-M. R. Génin, R. Aïssa, A. Géhin, M. Abdelmoula, O. Benali, V. Ernstsen, G. Ona-Nguema, C. Upadhyay, C. Ruby, *Solid State Sci.* **2005**, *7*, 545–572.
[13] H. C. B. Hansen, C. B. Koch, H. Nancke-Krogh, O. K. Borggaard, J. Sørensen, *Environ. Sci. Technol.* **1996**, *30*, 2053–2056.
[14] J.-M. R. Génin, P. Refait, G. Bourrié, M. Abdelmoula, F. Trolard, *Appl. Geochem.* **2001**, *16*, 559–570.
[15] M. Abdelmoula, P. Refait, S. Drissi, J. Mihe, J.-M. Génin, *Corros. Sci.* **1996**, *38*, 623–633.
[16] U. Schwertmann, H. Fechter, *Clay Miner.* **1994**, *29*, 87–92.
[17] J.-M. R. Génin, C. Ruby, C. Upadhyay, *Solid State Sci.* **2006**, *8*, 1330–1343.
[18] K. Barthélémy, S. Naille, C. Despas, C. Ruby, M. Mallet, *J. Colloid Interface Sci.* **2012**, *384*, 121–127.
[19] P. Oliva, J. Leonardi, J. Laurent, C. Delmas, J. Braconnier, M. Figlarz, F. Fievet, A. De Guibert, *J. Power Sources* **1982**, *8*, 229–255.
[20] P. V. Kamath, N. Vasanthacharya, *J. Appl. Electrochem.* **1992**, *22*, 483–485.
[21] T. N. Ramesh, P. V. Kamath, *J. Power Sources* **2008**, *175*, 625–629.
[22] R. Barnard, G. Crickmore, J. Lee, F. Tye, *J. Appl. Electrochem.* **1980**, *10*, 61–70.
[23] D. Friebel, M. W. Louie, M. Bajdich, K. E. Sanwald, Y. Cai, A. M. Wise, M. J. Cheng, D. Sokaras, T. C. Weng, R. Alonso-Mori, R. C. Davis, J. R. Bargar, J. K. Norskov, A. Nilsson, A. T. Bell, *J. Am. Chem. Soc.* **2015**, *137*, 1305–1313.
[24] E. Scavetta, Y. Vlamidis, T. Posati, M. Nocchetti, D. Tonelli, *ChemElectroChem* **2016**, *3*, 1320–1328.
[25] F. Bocher, A. Géhin, C. Ruby, J. Ghanbaja, M. Abdelmoula, J.-M. R. Génin, *Solid State Sci.* **2004**, *6*, 117–124.
[26] D. Singh, *J. Electrochem. Soc.* **1998**, *145*, 116–120.
[27] P. V. Kamath, M. Dixit, L. Indira, A. Shukla, V. G. Kumar, N. Munichandraiah, *J. Electrochem. Soc.* **1994**, *141*, 2956–2959.
[28] V. R. L. Constantino, T. J. Pinnavaia, *Inorg. Chem.* **1995**, *34*, 883–892.
[29] W. M. Martin, J. R. Green, *Ind. Eng. Chem. Anal. Ed.* **1933**, *5*, 114–118.
[30] J.-M. R. Génin, O. Guérin, A. Herbillon, E. Kuzmann, S. Mills, G. Morin, G. Ona-Nguema, C. Ruby, C. Upadhyay, *Hyperfine Interact.* **2012**, *204*, 71–81.
[31] M. S. Burke, L. J. Enman, A. S. Batchellor, S. Zou, S. W. Boettcher, *Chem. Mater.* **2015**, *27*, 7549–7558.
[32] J.-M. Génin, A. Christy, E. Kuzmann, S. Mills, C. Ruby, *Hyperfine Interact.* **2014**, *226*, 459–482.
[33] S. Brunauer, P. H. Emmett, E. Teller, *J. Am. Chem. Soc.* **1938**, *60*, 309–319.
[34] W. Luo, C. Jiang, Y. Li, S. A. Shevlin, X. Han, K. Qiu, Y. Cheng, Z. Guo, W. Huang, J. Tang, *J. Mater. Chem. A* **2017**, *5*, 2021–2028.
[35] B. C. M. Martindale, E. Reisner, *Adv. Energy Mater.* **2016**, *6*, 1502095.
[36] S. Zou, M. S. Burke, M. G. Kast, J. Fan, N. Danilovic, S. W. Boettcher, *Chem. Mater.* **2015**, *27*, 8011–8020.
[37] M. S. Burke, M. G. Kast, L. Trotochaud, A. M. Smith, S. W. Boettcher, *J. Am. Chem. Soc.* **2015**, *137*, 3638–3648.
[38] C. C. L. McCrory, S. Jung, J. C. Peters, T. F. Jaramillo, *J. Am. Chem. Soc.* **2013**, *135*, 16977–16987.
[39] M. E. Lyons, R. L. Doyle, *Int. J. Electrochem. Sci.* **2012**, *7*, 9488–9501.
[40] R. Frydendal, E. A. Paoli, B. P. Knudsen, B. Wickman, P. Malacrida, I. E. L. Stephens, I. Chorkendorff, *ChemElectroChem* **2014**, *1*, 2075–2081.
[41] X. Zhang, L. An, J. Yin, P. Xi, Z. Zheng, Y. Du, *Sci. Rep.* **2017**, *7*, 43590–43598.

Manuscript received: April 18, 2018
Accepted manuscript online: April 20, 2018
Version of record online: May 25, 2018

 © 2018 Wiley-VCH Verlag GmbH & Co. KGaA, Weinheim

6.1.1. Supporting Information

CHEMISTRY
A European Journal

Supporting Information

Oxygen Evolution Catalysis with Mössbauerite—A Trivalent Iron-Only Layered Double Hydroxide

Michael Ertl+,[a] Corina Andronescu+,[b] Jonathon Moir+,[c] Mirijam Zobel,[d] Friedrich E. Wagner,[e] Stefan Barwe,[b] Geoffrey Ozin,*[c] Wolfgang Schuhmann,*[b] and Josef Breu*[a]

chem_201801938_sm_miscellaneous_information.pdf

Supporting Information

1.0. Materials

Iron (II) chloride tetrahydrate, iron (III) chloride hexahydrate, sodium carbonate decahydrate, iron (III) sulfate, sodium hydroxide, barium chloride, ethanol and Nafion 117 sol. 5% were purchased from Sigma Aldrich. Hydrogen peroxide solution (30 %) and iron (II) sulfate was supplied by VWR chemicals.

2.0. Methods

2.1. Synthesis of mössbauerite (M)

This sample of mössbauerite was synthesized at room temperature according to the work of Génin[1] and Barthélémy et *al.*[2] A 2:1 mixture of ferrous (7.42 g) and ferric sulphate (6.52g) hydrate were dissolved in 95 mL Ar-saturated water yielding a total iron concentration of 0.4 M. In a second flask, 3.2 g of NaOH and 13.3 g of Na_2CO_3*$10H_2O$ were dissolved in 92 mL of Ar-saturated water (0.8 M in NaOH and 0.466 M in Na_2CO_3). The alkaline solution was added rapidly to the iron salt solution resulting in a pH of 7.6. The green rust that precipitated was then oxidized by adding stoichiometric amounts of a 30 wt% H_2O_2 solution whereupon the color changed to brownish-red. The mössbauerite suspension was finally stirred for another 10 minutes before being washed five times with distilled water before being freeze-dried.

2.2. Synthesis of mössbauerite using the modified procedure (M-50)

A 2:1 mixture of ferrous (2.65 g) and ferric chloride (1.75 g) hydrate were dissolved in 48 mL Ar-saturated water yielding a total iron concentration of 0.4 M. To this solution 40 mL of a 1.0 M Na_2CO_3 solution in Ar-saturated water was quickly added resulting in a pH of 7.5. Both solutions were heated to 50 °C before mixing them. Under continuous Ar-flow the green rust suspension was stirred vigorously at 50 °C for 30 minutes. Then an excess of 30 wt% H_2O_2 solution (2 mL) was added whereupon the color changed to brownish-red. The mössbauerite suspension was finally stirred for another 10 minutes before being washed five times with distilled water followed by freeze-drying.

2.2. Determination of the carbonate content of mössbauerite

To determine the carbonate content of mössbauerite, the sample was dissolved in Ar-saturated 1 M hydrochloric acid in a sealed flask. The flask was flushed with Ar and the CO_2 exhausted was captured in an alkaline solution of 1 M barium chloride. The resulting precipitate was filtered, dried and analyzed gravimetrically.

1 g of mössbauerite yielded 243 mg $BaCO_3$ (**M-50**) and 245 mg $BaCO_3$ (**M**), respectively. The following formula can be given for these synthetic mössbauerites: $Fe(III)_6O_{4.4}(OH)_{7.6}(CO_3)_{0.8}$.

2.3. Physico-chemical characterization

Powder X-ray difffraction (PXRD) pattern of green rust were recorded using a Bragg-Brentano-type diffractometer (X'PERT-Pro, PANalytical with CuKα-radiation (λ = 1.541 Å), equipped with a secondary monochromator to suppress fluorescence. The oxidation sensitive green rust sample was additionally washed with ethanol and acetone and placed in a flowing nitrogen atmosphere in a XRK chamber during the measurement. Thermogravimetric analysis (TGA) measurements were performed using a Netzsch STA 449c in Ar atmosphere with a heating rate of 10 K/min. Transmission electron microscopy (TEM) images were acquired using a Zeiss / LEO EM922 Omega Transmission Electron Microscope. Scanning Electron Microscopy (SEM) images were acquired using a Zeiss / LEO 1530. Fourier transform infrared spectroscopy (FT-IR) spectra were recorded with a JASCO FT/IR 6100 spectrometer. UV Vis diffuse reflectance spectra were recorded with an Agilent Cary 3 spectrophotometer equipped with an integrating sphere. A $^{57}Co/Rh$ (~25 mCi) source was used for Mössbauer spectroscopy. The specific surface area was measured with a Quantochrome Nova A with N_2 as adsorbate at 77 K according to the Brunauer-Emmet-Teller (BET) method.[3] Atomic force microscopy was performed with a commercial AFM (Dimension™ 3100, Veeco Instruments Inc., USA) equipped with a NanoScope® V SPM controller and a hybrid XYZ closed-loop scanner. Synchrotron high-energy X-ray diffraction measurements in capillary transmission mode were carried out at beamline ID-31 at the ESRF, Grenoble, with an X-ray energy of 70 keV (λ = 0.1771 Å), using a Pilatus X CdTe 2M detector and NIST CeO_2 for distance calibration.

2.4. Electrochemical characterization

Electrochemical measurements were carried out with a standard rotating disk electrode (RDE) set-up using a Ag/AgCl/3 M KCl as reference electrode, a Pt mesh as counter electrode and the

catalyst deposited on a glassy carbon electrode as working electrode, using an Autolab potentiostat / galvanostat (Methrom - Autolab, The Netherlands). In a typical experiment, 5 mg of the catalyst were dispersed in a mixture of Milli-Q water (490 µL), ethanol (490 µL) and 5 % sol. Nafion (20 µL). A specific volume of the suspension was pipetted on a glassy carbon electrode with an electrode surface of 0.078 cm^2 to form a catalyst film with a certain mass loading. The influence of the mass activity was studied (Figure S7). The highest catalytic activity was registered when 0.25 mA/cm^2 mass loading was used. Further electrochemical characterization was performed using this mass loading. The resulting films were left to dry in air under ambient conditions. The OER activity was investigated in O_2 saturated 1 M KOH solution. The catalyst surface was conditioned by performing 10 cyclic voltammograms between 0 – 0.5 V vs. Ag/AgCl/3 M KCl with a scan rate of 100 mV/s. Linear sweep voltammetry was performed from 0 vs. Ag/AgCl/3 M KCl to the potential corresponding to a current density of 20 mA/cm^2 (to prevent the detachment of the catalyst from the electrode due to the mechanical stress induced by the formed O_2 bubbles on the catalyst film) using a scan rate of 5 mV/s and 1600 rpm. Electrochemical impedance spectroscopy (EIS) was recorded under OER conditions. For this, 0.156 mA (2 mA/cm^2) was applied for 2 min in order to achieve a steady state potential. EIS was registered by applying 0.156 mA in the 10000 – 0.1 Hz frequency range.

All potentials were converted from the used RE: Ag/AgCl/3 M KCl to the reversible hydrogen electrode (RHE) using the following formula:

$$E_{RHE} = E_{measured} + 0.21 + 0.059\ pH, \text{ where } pH = 13.89.$$

LSVs were also corrected for the ohmic drop using the resistance of the electrolyte (R) obtained in the EIS at high frequency. Thus, the corrected potential was calculated using the following formula:

$$E_{RHE}\ (\text{corrected}) = E_{measured} + 1.03 - i \cdot R$$

where i is the current.

Long term measurements were performed galvanostatically by applying a current of 0.0078 A (corresponding to a current density of 10 mA/cm^2) for 4 h. The experimental conditions are similar to the ones described above.

The Faradaic efficiency (FE) of the catalyst was evaluated using rotating ring disk electrode (RRDE) measurements. The experiments were performed in Ar-saturated 1 M KOH solution. The potential of the Pt ring electrode was set at -0.7 V vs. Ag/AgCl/3M KCl. Initially, the open-

circuit potential (OCP) was applied to the disk electrode for ~ 300 s to establish the background currents for both ring and disk electrodes. The potential of the disk electrode was further increased to 0.66 V vs. Ag/AgCl/3M KCl and kept at this potential for ~ 300 s. The FE was calculated using the following formula: $FE = i_{ring}/(i_{disk} \cdot N)$, where N is the collection efficiency. The collection efficiency was determined using a solution of 5 mM $K_3[Fe(CN)_6]$ in 1 M KOH. The potential of the Pt ring electrode was kept at 0.4 V vs. Ag/AgCl/3M KCl, while the potential of the disk electrode was swept from +0.4 to -0.1 V vs. Ag/AgCl/3M KCl with a scan rate of 5 mV/s. The calculated collection efficiency (N) is 0.2.

3.0. Supplementary results and discussion

3.1. Powder X-ray Diffraction

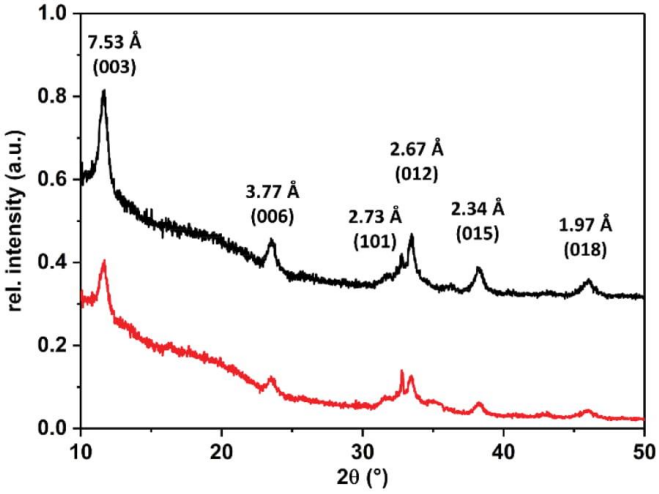

Figure S1A. PXRD (Cu Kα radiation (λ=1.541 Å)) of green rust synthesized at room temperature (red, **M**) and 50 °C (black, **M-50**). The diffractogram of green rust shows a rational *00l* series with a d_{003}-spacing of 7.53 Å (2θ = 11.6°). Although the material is turbostratically disordered, we assume the 3T polytype for indexing to be consistent with the literature. All peaks can be indexed with the unit cell published by Génin et *al.*[4] for green rust indicating that no other crystalline phases are present.

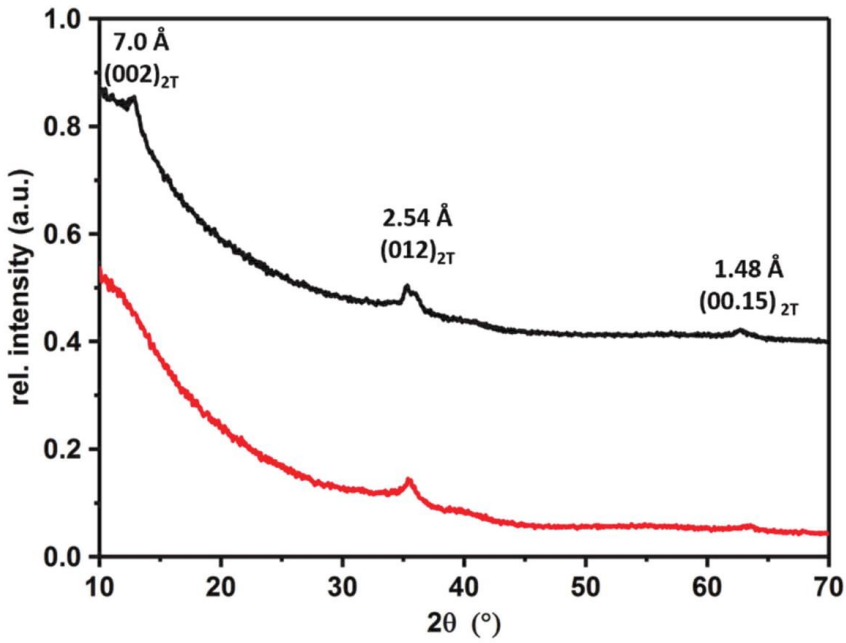

Figure S1B. PXRD (Cu Kα radiation (λ=1.541 Å)) of mössbauerite synthesized according to established literature procedures,[1, 2] at room temperature (**M**, red) and at 50 °C (**M-50**, black). Only for **M-50** a basal reflection is observed d ~ 7.0 Å (2θ = 12.6°), which is in good agreement with the d-spacing reported for the T2 polymorph by Génin et *al*. (d ~ 7.1 Å).[5] The low intensity is related to the fluorescence which results in high background intensity despite the secondary monochromator applied. The lack of the basal reflection for the sample **M** most likely is related to a more pronounced interstratification of slightly different basal spacings.

S5

3.2. Thermogravimetric analysis (TGA)

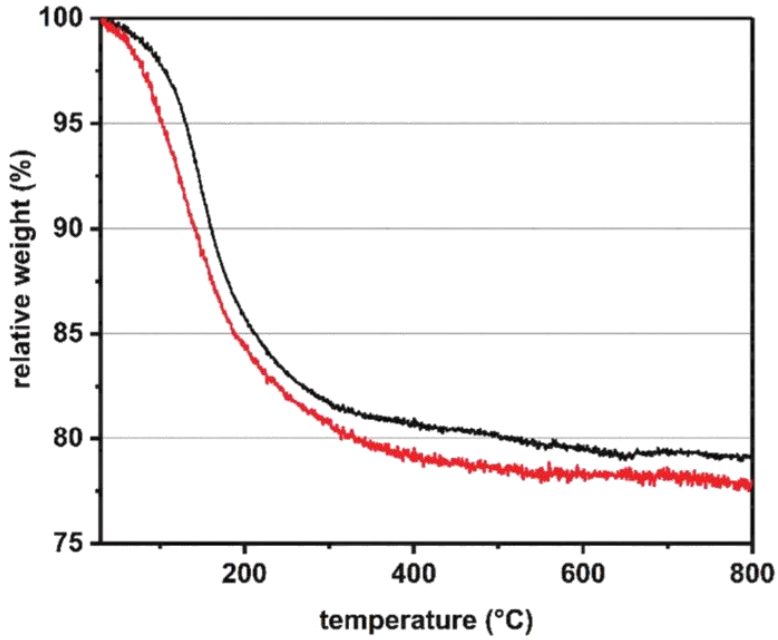

Figure S2. TGA analysis of **M** (red) and **M-50** (black).

The TG curves of the mössbauerite samples show a continuous weight loss of 21 % (**M-50**) and 22 % (**M**) up to 800 °C. Upon thermal decomposition of mössbauerite producing hematite a total mass loss of 24.7 wt% is expected:

$$Fe(III)_6O_{4.4}(OH)_{7.6}(CO_3)_{0.8}*3\ H_2O \rightarrow 3\ Fe_2O_3 + 0.8\ CO_2 + 6.8\ H_2O$$

$M_{mössbauerite}$ = 638 g/mol

$M_{hematite}$ = 160 g/mol

For 1 mol mössbauerite the weight loss amounts to

$$\Delta m = m_{mössbauerite} - 3 \cdot m_{hematite} = 158\ g$$

$$wt\%_{H2O,CO2} = \Delta m\ /\ m_{mössbauerite} = 158\ g\ /\ 638\ g = 24.7\ \%$$

The observed weight losses are in good agreement with expectations confirming the above formula for the synthetic mössbauerite.

S6

3.3. Electron micrographs

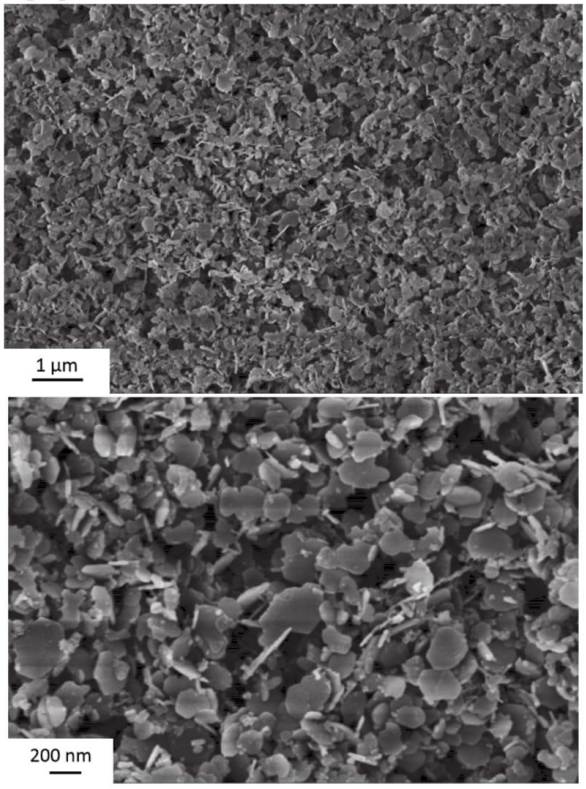

Figure S3A. SEM images of **M-50** recorded at different magnifications.

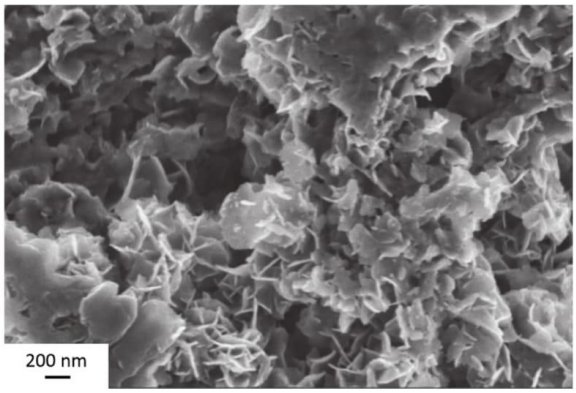

Figure S3B. SEM image of M.

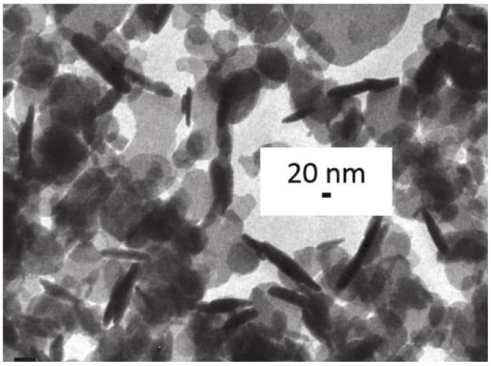

Figure S3B. TEM image of M-50.

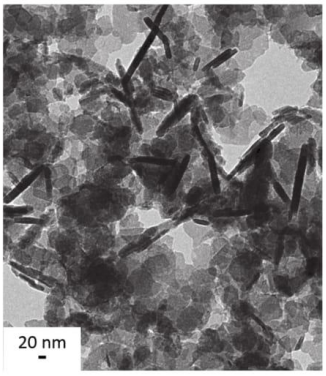

Figure S3C. TEM image of M.

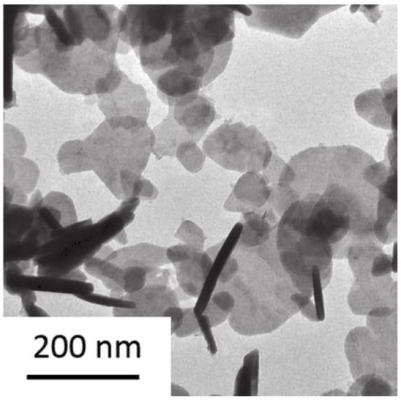

Figure S3D. TEM images of the intermediate green rust synthesized at 50 °C.

SEM and TEM images of both the intermediate and **M** and **M-50** show thin hexagonally shaped platelets. Typical platelet diameters in the range of 50-200 nm are observed. The thickness of LDH stacks is in both cases (**M-50** and **M)** 20 nm on average measured on 20 different stacks. The crystal edges of **M** are less sharp and the shapes are irregular.

3.4. Atomic Force Microscopy (AFM)

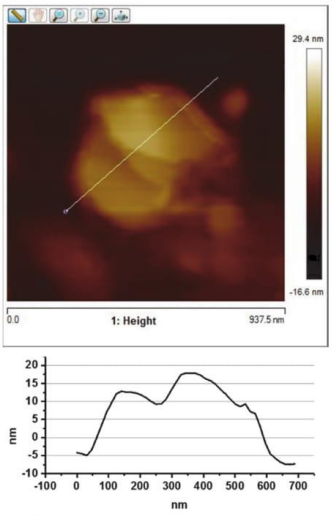

Figure S4A. AFM image and height analysis of of **M-50**.

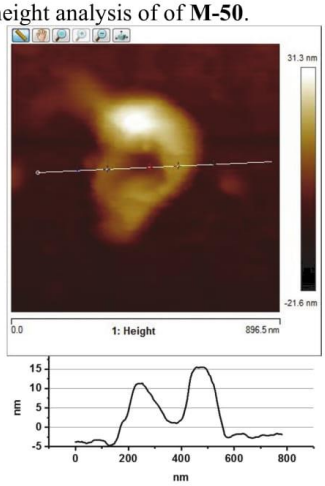

Figure S4B. AFM image and height analysis of **M**.

3.5. Fourier transform infrared spectroscopy (FT-IR)

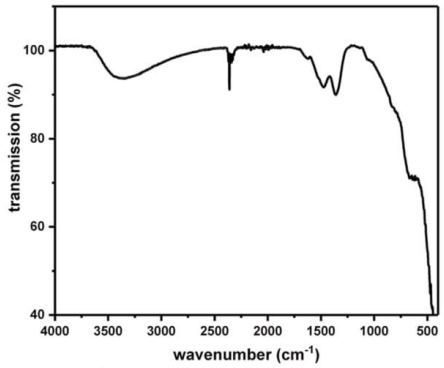

Figure S5A. FT-IR spectroscopy of **M-50**.

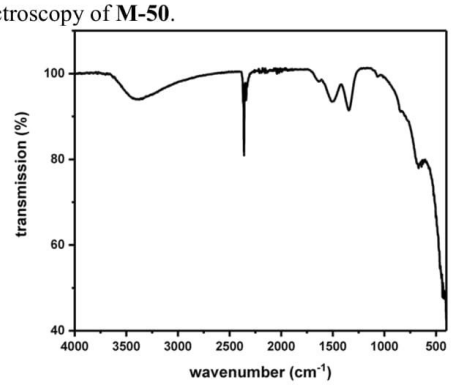

Figure S5B. FT-IR spectroscopy of **M**.

The FT-IR spectra of **M** and **M-50** are identical and show a broad absorption at 3400 cm^{-1} originating from the excitation of O-H stretching. Absorption bands at 1473 and 1350 cm^{-1} are characteristic for carbonate. Weak bands at lower wavenumbers can be assigned to different Fe-O streching.[6] The characterizing vibrational band of sulfate (1160 cm^{-1})[7] is not visible in the spectra of **M**. Clearly, carbonate is the only interlayer anion for both **M** and **M-50.**

3.6. UV Vis Diffuse reflectance spectroscopy (UV Vis/DRS)

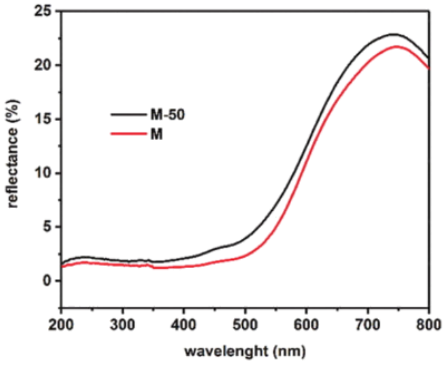

Figure S6A. UV Vis diffuse reflectance spectra of **M-50** (black) and **M** (red).

The DRS spectra of both **M-50** and **M** show a band-gap transition at ~2.4 eV. While the semiconductor transition is prominent, no localized transitions can be observed.

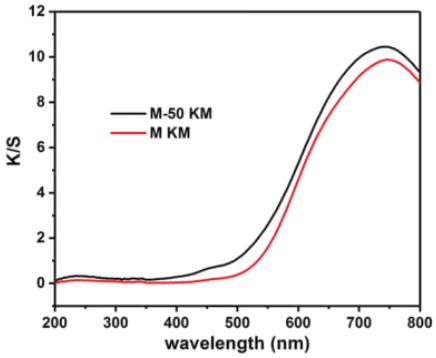

Figure S6B. Kubelka-Munk function of the measured UV-Vis DRS of **M-**50 (black) and **M** (red) spectra plotted versus the wavelength. From the KM plot a band-gap of 2.4 eV can be estimated.

3.7. Mössbauer spectroscopy

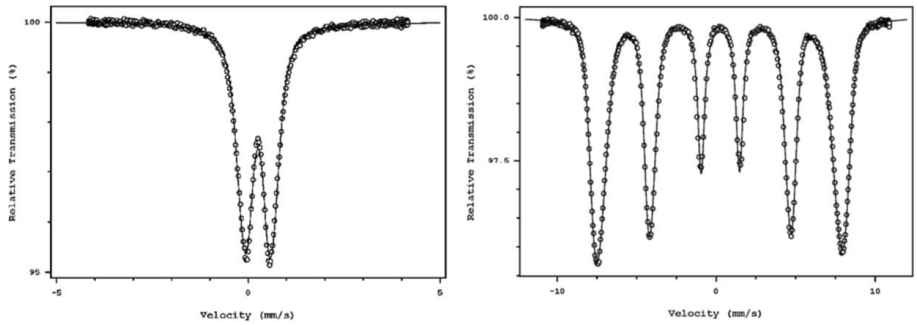

Figure S7A. Mössbauer spectra of **M-50** recorded at room-temperature (left) and at 4.2 K (right).

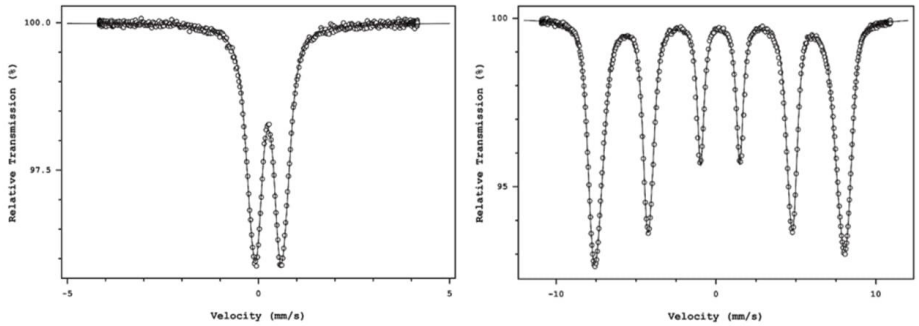

Figure S7B. Mössbauer spectra of **M** recorded at room-temperature (left) and at 4.2 K (right).

Both samples, **M** and **M-50** show similar Mössbauer spectra. In line with previous reports on mössbauerite, the room-temperature ^{57}Fe Mössbauer spectra consists of a single, broad doublet with a mean quadrupole splitting (QS) of 0.69 mm/s and an isomer shift (IS) of 0.38 mm/s with respect to metallic iron. At 4.2 K one observes a sextet pattern with broad lines, a hyperfine field of 49.4 T and a very small electric quadrupole interaction (quadrupole shift) of only -0.09 mm/s. These values agree well with those expected for mössbauerite.[8] No residual ferrous iron doublet was observed in the room temperature spectrum indicating complete oxidation to ferric iron. The isomer shift is reasonable for octahedrally coordinated iron.[5, 9]

3.8. Brunauer-Emmet-Teller surface area analysis

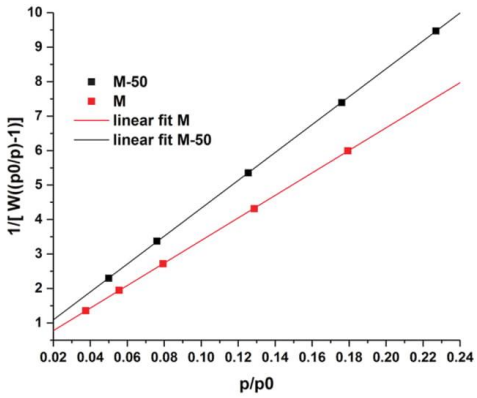

Figure S8. BET plot for N_2 on the samples **M** and **M-50** at 77 K.

The BET equation is given by:

$$\frac{1}{W\left({}^{p_0}/_{p}\right) - 1} = \frac{1}{W_m * C} + \frac{C - 1}{W_m * C} * \left(\frac{p}{p_0}\right)$$

W: weight of the gas adsorbed

p_0/p: relative pressure

W_m: weight of the adsorbate constituting a monolayer of surface coverage

C: BET constant

The measurement data were processed with Quantochrome® ASiQwin™. The adsorbate is N_2 and the data was refined with Oxygen/Zeolite as adsorbent. The results are summarized in the following table.

Table S1: Results of the BET surface area analysis.

	M	**M-50**
specific surface are (m^2/g)	106	85
C constant	+ 273	+ 144
correlation coefficient R	0.999979	0.999995

3.9. Mass loading and mass activity

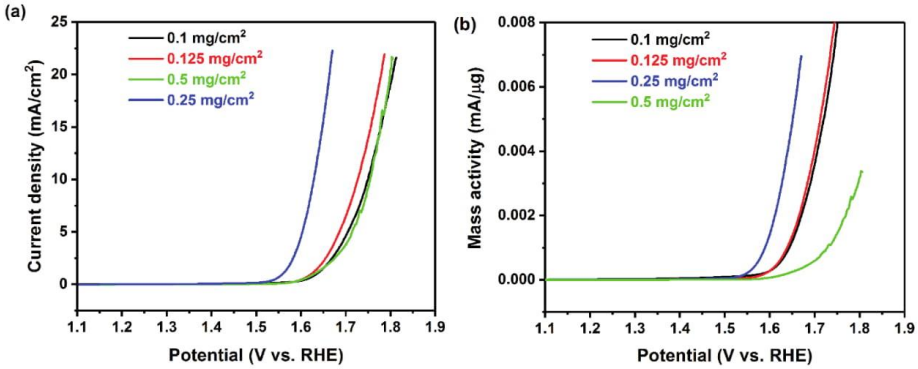

Figure S9. Mass loading influence plotted as current density (a) and mass activity (b) as a function of the potential.

Linear sweep voltammograms registered with a scan rate of 5 mV/s in 1 M KOH, 1600 rpm for **M-50** using different mass loadings. The results are presented as current density and mass activity as function of the applied potential.

3.10. Electrochemical Impedance Spectroscopy (EIS)

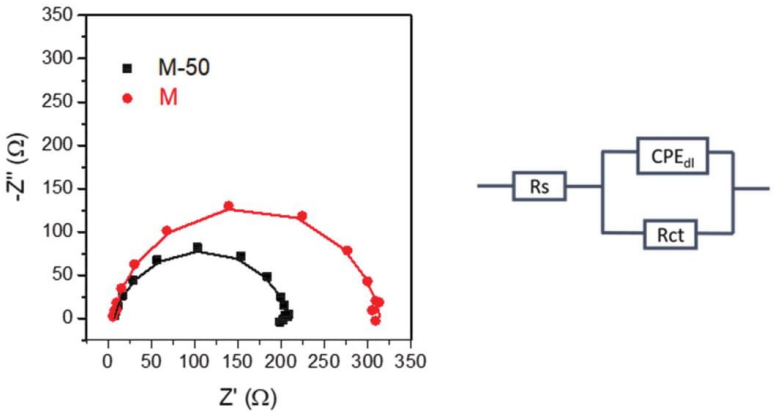

Figure S10. Fitted Nyquist plots registered at 2 mA/cm^2 using the modified Randles circuit.

S14

Table S2. Parameters obtained by fitting the Nyquist spectra using the modified Randler circuit.

Sample	R_s (Ω)	CPE_{dl} – Yo (μMho)	CPE_{dl} – n_{dl}	R_{ct} (Ω)	χ^2	Cdl* (mF)	ESCA§
M-50	6.68	33	0.83	202.41	0.33	0.006	0.15
M	5.63	34	0.88	308.9	0.29	0.011	0.275

Nyquist plots from Figure S9a were fitted using the modified Randles Circuit, where a constant phase element (CPE) was introduced instead of a capacitor. In the model, R_s is the electrolyte resistance, R_{ct} - charge transfer resistance and CPE_{dl} - double layer capacitance.

*The double layer capacitance was calculated using the following formula[10]:

$$C_{dl} = \left[Y_o \cdot \left(\frac{1}{R_s} + \frac{1}{R_{ct}}\right)^{(n_{dl}-1)}\right]^{1/n_{dl}}$$

§Estimation of electrochemically surface area (ESCA) was done from the double layer capacitance using the following formula:

$$ECSA = \frac{C_{dl}}{C_s}$$

Where Cs is the specific capacitance of the sample. We used Cs = 0.04 mF/cm^2 as an average value which was reported for different metal electrodes in alkaline environment. The resulted value needs to be carefully used since it was described that the error used to determine ECSA by using an average C_S value can be off a factor of 7.

3.11. Faradaic efficiency

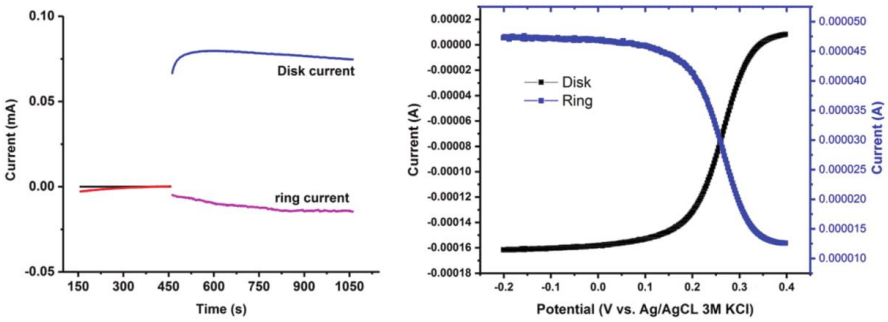

Figure S11. Chronoamperometric Faradaic efficiency measurements.

S15

Chronoamperometric Faradaic efficiency measurements registered in Ar saturated 1 M KOH solution (left). The potential of the Pt disk electrode was -0.7 V vs. Ag/AgCl/3M KCl. The potential of the disk electrode was initially kept at OCP and was then increased to 0.66 V vs. Ag/AgCl/3M KCl (~450 s). Collection efficiency measurement performed in 5 mM $K_3[Fe(CN)_6]$ in 1 M KOH solution (right). The potential of the disk electrode was swept from 0.4 to -0.2 V vs. Ag/AgCl/3M KCl with a scan rate of 5 mV/s, while the potential of the ring electrode was kept constant at +0.4 V vs. Ag/AgCl/3M KCl.

3.12. Catalyst conditioning

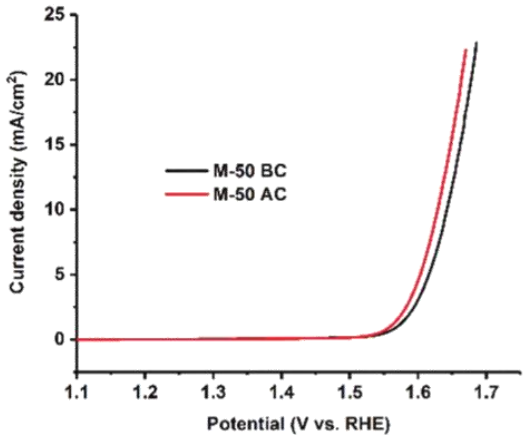

Figure S12. Linear sweep voltammograms registered before (**M-50 BC**) and after (**M-50 AC**) conditioning.

Linear sweep voltammograms registered with a scan rate of 5 mV/s in 1 M KOH, 1600 rpm for **M-50 BC** and **M-50 AC** performing 10 cyclic voltammograms between 0 – 0.5 V vs. Ag/AgCl/ 3 M KCl with a scan rate of 100 mV/s (conditioning step). The slightly increased activity after conditioning probably origins from a modification of the catalyst in contact with the electrolyte.

3.13. *Post-electrolysis* SEM and EDX characterization

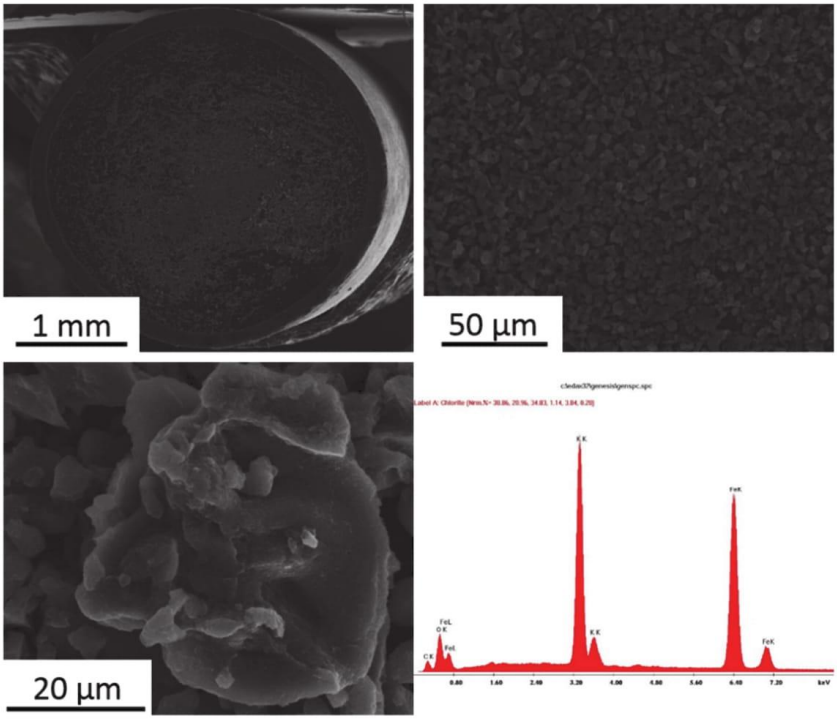

Figure S13. SEM pictures and EDX spectrum of the **M-50** deposited on the GCE after the long-term measurements (**M-50 4h**).

SEM images of the electrode show, that the catalyst is still attached to the electrode. However, the material is rather inhomogeneously distributed. During catalysis, small amounts of catalyst can be dissolved into the electrolyte and redeposited as amorphous FeOOH.

The EDX spectrum registered after electrolysis show just the presence of Fe, K, C and O, indicating that no other metal was intercalated as impurity from the electrolyte. Also in PXRD we were able to fit all peaks to Fe based compounds or $KHCO_3$ (Figure S14).

3.14. *Post-electrolysis* synchrotron X-ray diffraction

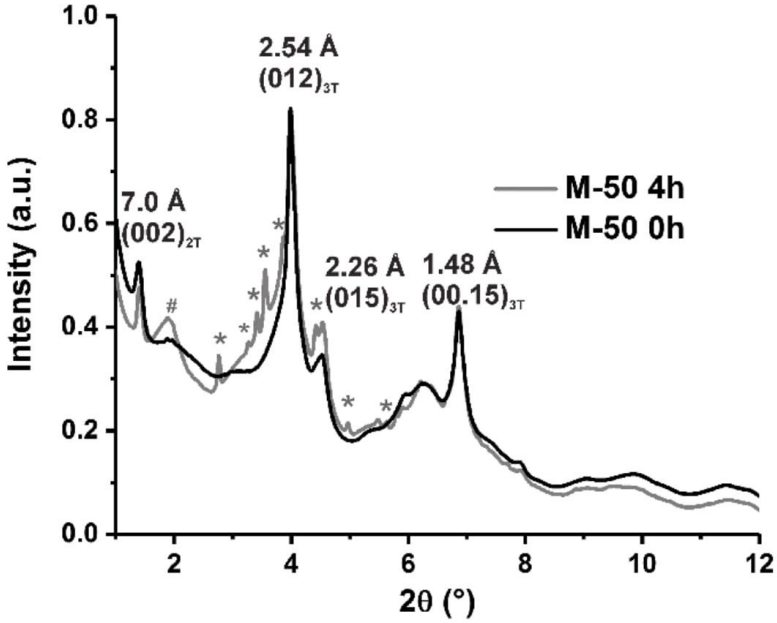

Figure S14. Synchrotron X-ray diffraction data of **M-50** (black) and **M-50 4h** (grey) before and after long term measurement. Reflections marked by an asterisk can be assigned to $KHCO_3$, the broad reflection at ~2θ = 2° originates from akaganeite (PDF# 00-034-1266).

S18

3.15. Table S3: Comparison of catalytic performance of transition metal species

Table S3. Catalytic activity of related materials in the electrocatalytic OER in comparison to this work.

Material	η@10mAcm^{-2} (mV)	Electrode	Electrolyte	Tafel slope (mV/dec)
M-50	400	GC	1M KOH	57
M	540	GC	1M KOH	125
$(Ni_1/Fe_0)OOH$[11]	680	Au/Ti-SiN	0.1 M KOH	
$(Ni_{0.9}/Fe_{0.1})OOH$[11]	380	Au/Ti-SiN	0.1 M KOH	
$(Ni_{0.75}/Fe_{0.25})OOH$	370	Au/Ti-SiN	0.1 M KOH	
$(Ni_{0.5}/Fe_{0.5})OOH$[11]	375	Au/Ti-SiN	0.1 M KOH	
$(Ni_{0.25}/Fe_{0.75})OOH$[11]	410	Au/Ti-SiN	0.1 M KOH	
$(Ni_{0.1}/Fe_{0.9})OOH$[11]	525	Au/Ti-SiN	0.1 M KOH	
$(Ni_0/Fe_1)OOH$[11]	560	Au/Ti-SiN	0.1 M KOH	
bulk NiFe LDH[12]	347	GC	1M KOH	67
δ-MnO_2 ns[13]	320	Ni foam	1 M KOH	40
bulk-CoFe LDH[14]	400	Ni foam	1 M KOH	47
ex-CoFe LDH[14]	255	Ni foam	1 M KOH	40
ex-CoFe LDH[15]	232	Ni foam	1 M KOH	36
NiFe LDH/Co,N-CNF[16]	312	GC	0.1 M KOH	60
NiTi MMO ns[17]	320	GC	1 M KOH	52
α-FeOOH [18]	600	Pt-mesh	1 M KOH	
α-FeOOH calc. [18]	480	Pt-mesh	1 M KOH	
FeOOH[19]	420	Pt/Au	1 M KOH	46 / 31
β-$Ni(OH)_2$ ns[20]	500 @ 4.4 mAcm^{-2}	GC	1 M KOH	415

(abbreviations: Au/Ti-SiN: Au and Ti-coated silicon nitride; ns: nanosheet; ex: exfoliated; Co,N-CNF: Co,N-Codoped carbon nanoframes, GC: glassy carbon; calc.: calcined at 300 °C)

S19

References

[1] F. Bocher, A. Géhin, C. Ruby, J. Ghanbaja, M. Abdelmoula, J.-M. R. Génin, *Solid State Sci.* **2004**, *6*, 117-124.

[2] K. Barthélémy, S. Naille, C. Despas, C. Ruby, M. Mallet, *J. Colloid Interface Sci.* **2012**, *384*, 121-127.

[3] S. Brunauer, P. H. Emmett, E. Teller, *J. Am. Chem. Soc.* **1938**, *60*, 309-319.

[4] S. Drissi, P. Refait, M. Abdelmoula, J.-M. R. Génin, *Corros. Sci.* **1995**, *37*, 2025-2041.

[5] J.-M. R. Génin, S. Mills, A. Christy, O. Guérin, A. Herbillon, E. Kuzmann, G. Ona-Nguema, C. Ruby, C. Upadhyay, *Mineral. Mag.* **2014**, *78*, 447-465.

[6] J. C. Villalba, V. R. Constantino, F. J. Anaissi, *J. Colloid Interface Sci.* **2010**, *349*, 49-55.

[7] D. Peak, R. G. Ford, D. L. Sparks, *J. Colloid Interface Sci.* **1999**, *218*, 289-299.

[8] J.-M. R. Génin, O. Guérin, A. Herbillon, E. Kuzmann, S. Mills, G. Morin, G. Ona-Nguema, C. Ruby, C. Upadhyay, *Hyperfine Interact.* **2012**, *204*, 71-81.

[9] J.-M. Génin, A. Christy, E. Kuzmann, S. Mills, C. Ruby, *Hyperfine Interact.* **2014**, *226*, 459-482.

[10] C. C. L. McCrory, S. Jung, J. C. Peters, T. F. Jaramillo, *J. Am. Chem. Soc.* **2013**, *135*, 16977-16987.

[11] D. Friebel, M. W. Louie, M. Bajdich, K. E. Sanwald, Y. Cai, A. M. Wise, M. J. Cheng, D. Sokaras, T. C. Weng, R. Alonso-Mori, R. C. Davis, J. R. Bargar, J. K. Norskov, A. Nilsson, A. T. Bell, *J. Am. Chem. Soc.* **2015**, *137*, 1305-1313.

[12] F. Song, X. Hu, *Nat. Commun.* **2014**, *5*, 4477.

[13] Y. X. Zhao, C. Chang, F. Teng, Y. F. Zhao, G. B. Chen, R. Shi, G. I. N. Waterhouse, W. F. Huang, T. R. Zhang, *Adv. Energy Mater.* **2017**, *7*, 1700005.

[14] P. F. Liu, S. Yang, B. Zhang, H. G. Yang, *ACS Applied Materials & Interfaces* **2016**, *8*, 34474-34481.

[15] R. Liu, Y. Y. Wang, D. D. Liu, Y. Q. Zou, S. Y. Wang, *Adv. Mater.* **2017**, *29*, 1701546.

[16] Q. Wang, L. Shang, R. Shi, X. Zhang, Y. F. Zhao, G. I. N. Waterhouse, L. Z. Wu, C. H. Tung, T. R. Zhang, *Adv. Energy Mater.* **2017**, *7*, 1700467.

[17] Y. F. Zhao, X. D. Jia, G. B. Chen, L. Shang, G. I. N. Waterhouse, L. Z. Wu, C. H. Tung, D. O'Hare, T. R. Zhang, *J. Am. Chem. Soc.* **2016**, *138*, 6517-6524.

[18] W. Luo, C. Jiang, Y. Li, S. A. Shevlin, X. Han, K. Qiu, Y. Cheng, Z. Guo, W. Huang, J. Tang, *J. Mater. Chem. A* **2017**, *5*, 2021-2028.

[19] S. Zou, M. S. Burke, M. G. Kast, J. Fan, N. Danilovic, S. W. Boettcher, *Chem. Mater.* **2015**, *27*, 8011-8020.

[20] J. F. Xie, X. D. Zhang, H. Zhang, J. J. Zhang, S. Li, R. X. Wang, B. C. Pan, Y. Xie, *Adv. Mater.* **2017**, *29*, 1604765.

6.2. Mössbauerite/WO_3 Heterojunction Photoanodes

Michael Ertl,[†,+] Zili Ma,[‡,+] Thomas Thersleff, Pengbo Lyu,[§] Sven Huettner,[‖] Petr Nachtigall,[§] Josef Breu,[†] and Adam Slabon,[‡,«]

Mössbauerite as Iron-Only Layered Oxyhydroxide Catalyst for WO_3 Photoanodes

Published in Inorganic Chemistry **2019**, *58*, 9655-9662.
Reprinted with permission, Copyright (2019) American Chemical Society.
Impact Factor (2019) Inorg. Chem.: 4.85
https://doi.org/10.1021/acs.inorgchem.9b00327

† Bavarian Polymer Institute and Department of Chemistry, University of Bayreuth, Universitätsstr. 30, 95440 Bayreuth, Germany
‡ Institute of Inorganic Chemistry, RWTH Aachen University, Landoltweg 1, 52056, Germany
§ Department of Physical and Macromolecular Chemistry, Faculty of Sciences, Charles University, Hlavova 8, 128 43 Prague 2, Czech Republic
‖ Organic and Hybrid Electronics, University of Bayreuth, Universitätsstr. 30, 95440 Bayreuth, Germany
« Department of Materials and Environmental Chemistry, Stockholm University, Svante Arrhenius väg 16 C, 106 91 Stockholm, Sweden

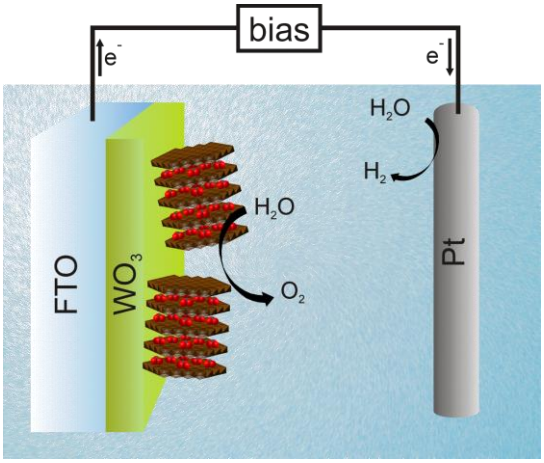

Individual Contributions:

The publication was initiated by Prof. Josef Breu and Prof. Adam Slabon. The synthesis, characterization and initial photoelectrochemical experiments were done by myself. The in-depth photoelectrochemical experiments were done by Zili Ma. Prof. Sven Hüttner helped with the interpretation of the XPS spectra. Thomas Thersleff performed the TEM experiments. Pengbo Lyu and Prof. Petr Nachtigall calculated and analyzed the electronic band structure. The manuscript was written by myself, Prof. Josef Breu and Prof. Adam Slabon.

Inorganic Chemistry
Article
Cite This: Inorg. Chem. 2019, 58, 9655−9662
pubs.acs.org/IC

Mössbauerite as Iron-Only Layered Oxyhydroxide Catalyst for WO_3 Photoanodes

Michael Ertl,[†,#] Zili Ma,[§,#] Thomas Thersleff,[∥] Pengbo Lyu,[⊥] Sven Huettner,[‡] Petr Nachtigall,[⊥] Josef Breu,[*,†] and Adam Slabon[*,∥]

[†]Bavarian Polymer Institute and Department of Chemistry and [‡]Organic and Hybrid Electronics, University of Bayreuth, Universitätsstraße 30, Bayreuth D-95440, Germany

[§]Institute of Inorganic Chemistry, RWTH Aachen University, Landoltweg 1, Aachen D-52056, Germany

[∥]Department of Materials and Environmental Chemistry, Stockholm University, Svante Arrhenius väg 16 C, Stockholm 10691, Sweden

[⊥]Department of Physical and Macromolecular Chemistry, Faculty of Sciences, Charles University, Hlavova 8, Prague 212843, Czech Republic

Supporting Information

Downloaded via UNIV BAYREUTH on August 5, 2019 at 10:19:23 (UTC).
See https://pubs.acs.org/sharingguidelines for options on how to legitimately share published articles.

ABSTRACT: Mössbauerite, a trivalent iron-only layered oxyhydroxide, has been recently identified as an electrocatalyst for water oxidation. We investigated the material as potential cocatalyst for photoelectrochemical water oxidation on semiconductor photoanodes. The band edge positions of mössbauerite were determined for the first time with a combination of Mott−Schottky analysis and UV−vis diffuse reflectance spectroscopy. The positive value of the Mott−Schottky slope and the flatband potential of 0.34 V vs reversible hydrogen electrode (RHE) identifies the material as an n-type semiconductor, but bare mössbauerite does not produce noticeable photocurrent during water oxidation. Type-II heterojunction formation by facile drop-casting with WO_3 thin films yielded photoanodes with amended charge carrier separation and photocurrents up to 1.22 mA cm^{-2} at 1.23 V vs RHE. Mössbauerite is capable of increasing the charge carrier separation at lower potential and improving the photocurrent during photoelectrochemical water oxidation. The rise in photocurrent of the mössbauerite-functionalized WO_3 photoanode thus originates from improved charge carrier separation and augmented hole collection efficiency. Our results highlight the potential of mössbauerite as a second-phase catalyst for semiconductor electrodes.

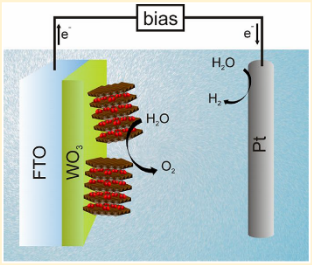

INTRODUCTION

Photoelectrochemical (PEC) water-splitting enables the direct conversion of solar energy into useable energy consisting of storable hydrogen.[1−6] PEC water-splitting consists of two half reactions. On the cathode site, electrons are used to generate molecular hydrogen, formally from protons, which is generally highly efficiently catalyzed by noble metals.[7] The oxygen evolution reaction (OER) at the photoanode proceeds via a coupled multistep electron transfer reaction and is more demanding from both a kinetic and a thermodynamic point of view.[8] A broad variety of oxidic n-type semiconductor materials such as TiO_2,[9] ZnO,[10] α-Fe_2O_3,[11] WO_3,[12] $BiVO_4$,[13] and $CuWO_4$[14] have been employed in recent years as photoanodes.

Still, these materials have substantial drawbacks, i.e., poor hole transfer efficiency, low charge carrier mobility, and therefore high recombination rates, which decrease their performance significantly.[15] Along with nano-[16] and meso-structuring,[2] the concept of OER cocatalysts has led to uncountable combinations of semiconductor and cocatalyst for efficient PEC water oxidation.[17]

Among all those efforts, the most challenging goal is to create a highly efficient, highly stable, environmentally friendly, and cost-efficient combination of materials.[18] This is a prerequisite for rendering PEC water splitting a superior alternative to a wide variety of energy generation systems.[19]

Thin iron-based coatings, such as FeOOH,[20] $FeNiO_x$,[21] and ferrihydrite,[22] have emerged as efficient catalytic coating to increase the PEC performance of photoanodes. Ferrihydrite is an iron oxyhydroxide nanomaterial that can raise the photocurrent of different oxide and nitride semiconductors photoanodes.[23] For instance, ferrihydrite can act simultaneously as a protective coating and hole storage layer for $SrTaO_2N$ nanowire photoanodes.[24] Layered double hydroxides (LDH) are a promising class of materials for electrocatalysis, for photocatalysis, or as precursor for oxidic catalysts because of their facile synthesis, versatility in chemical composition, and structural morphology.[25]

Received: February 3, 2019
Published: July 16, 2019

ACS Publications © 2019 American Chemical Society

DOI: 10.1021/acs.inorgchem.9b00327
Inorg. Chem. 2019, 58, 9655−9662

Recently, we have shown that mössbauerite (Figure 1A), an iron-only layered oxyhydroxide, is an efficient electrocatalyst

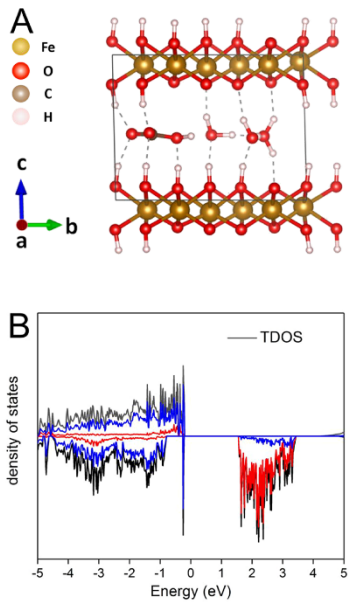

Figure 1. (A) Side view of mössbauerite structure; (B) total and partial density of states (TDOS and PDOS, respectively) projected on Fe 3d and O 2p atomic orbitals (blue and red, respectively). The upper and lower panels indicate the spin-up and spin-down projections, respectively.

for water oxidation, generating 10 mA cm^{-2} at 1.63 V vs RHE.[26] The layers in mössbauerite are of CdI_2-type ($Fe^{III}_6O_4(OH)_8[CO_3]\cdot 3H_2O$); they carry a positive charge and are separated by carbonate for charge balance. Mössbauerite is an iron-only material that can be synthesized by fast chemical oxidation applying H_2O_2 to green rust, a Fe^{2+}/Fe^{3+}= 2:1 mixed-valence iron-only LDH that is green in color.[27] Upon oxidation to mössbauerite, partial deprotonation to an oxyhydroxide occurs concomitantly.

Mössbauerite is an intrinsic semiconductor with a band gap in the visible range. The strong light absorption, purely semiconducting behavior, and the layered oxyhydroxide structure make mössbauerite a promising material for the formation of heterojunctions. Previously, a type-II (n-type/n-type) heterojunction of tungsten trioxide and hematite has been shown to increase charge carrier separation.[11]

In this work, we report on the physical characterization of mössbauerite by a combination UV−vis diffuse reflectance spectroscopy, Mott−Schottky analysis, XPS, and DFT+U calculations. We employ these nanoplatelets for the first time as a cocatalyst for thin films of monoclinic tungsten oxide and investigate the effect of mössbauerite functionalization for PEC water oxidation.

■ EXPERIMENTAL SECTION

Synthesis of Mössbauerite. All chemicals have been purchased from Sigma. Mössbauerite was synthesized according to a previously reported procedure.[28] In brief, a 2:1 mixture of ferrous (2.65 g, 99.9%) and ferric chloride hydrate (1.75 g, 99.9%) was dissolved in argon-saturated deionized water, yielding a total iron concentration of 0.4 M. Subsequently, a 1 M solution of Na_2CO_3 in argon-saturated water was added at a temperature of 323 K. Under continuous argon flow, the resulting greenish suspension was stirred for 30 min at 323 K. Then, 2 mL of a 30 wt % H_2O_2 solution was added in one shot whereupon the color of the suspension changes to brownish-red. The obtained mössbauerite suspension was washed with distilled water and finally freeze-dried. Mössbauerite can be handled in air.

Synthesis of WO_3 Photoanodes. WO_3 thin films were grown on conductive fluorine-doped tin oxide (FTO) glass slides (2.2 mm thick, Sigma-Aldrich) based on a modified synthesis by Diao.[29] First, 5 mL of 0.1 M $Na_2WO_4\cdot 2H_2O$ (99.995%) were cautiously added dropwise into 10 mL of 0.1 M $H_2C_2O_4$(99%). Then, 10 mL of 1 M HCl was added into the above mixture and ultrasonicated for 15 min. Next, 6 mL of the solution was transferred to a 20 mL Teflon-lined stainless-steel autoclave, and the FTO substrate was placed vertically. The autoclave was sealed tightly and heated at 453 K for 2 h. After cooling down to room temperature, the FTO glass was washed with deionized water. The FTO glass with the deposited thin film was annealed at 823 K for 2 h under ambient atmosphere in order to increase the crystallinity of the tungsten trioxide.

Deposition of Mössbauerite on the WO_3 Photoanode. Mössbauerite powder was dispersed by ultrasound in ethanol (35.0 $\mu g\ mL^{-1}$). The WO_3 thin film electrode was placed on a heating plate at 323 K and the Fe-LDH dispersion was drop-cast on the surface. The electrode was dried under vacuum for 24 h.

Preparation of Mössbauerite on FTO. Electrophoretic deposition (EPD) was used to immobilize mössbauerite onto FTO. Briefly, 5 mg of iodine and 20 mg of mössbauerite powder were dispersed in 30 mL of acetone with ultrasonication to obtain a suspension for EPD. Two FTO glass slides were electrically wired and placed inside the solution within a distance of 5 mm under 20 V of bias for 5 min to coat the FTO substrate with a mössbauerite layer.

X-ray Diffraction (XRD). Powder XRD patterns of the bare thin films, WO_3 and WO_3/mössbauerite photoelectrodes, were recorded in the transmission mode on a STOE STADI-P diffractometer (Cu $K\alpha_1$ radiation) equipped with a DECTRIS Mythen 1K detector.

Electron Microscopy, X-ray Photoelectron Spectroscopy (XPS), and UV−Vis Spectroscopy. Transmission electron microscopy (TEM) images were acquired using a Zeiss/LEO EM922 Omega transmission electron microscope. Scanning electron microscopy (SEM) images were acquired using a Zeiss/LEO 1530. The TEM results from Figure 7 were obtained on an aberration-corrected Themis Z instrument from FEI company (now Thermo Fisher) operated at 300 kV. For the high-angle annular dark field (HAADF) and electron energy-loss spectroscopy (EELS) results, the TEM was operated in STEM mode with a convergence angle of 19.5 mrad and a collection angle of 17 mrad. The selected-area electron diffraction pattern (SAEDP) was acquired by using a parallel illumination and a selected area entrance aperture centered over an agglomerate similar to that shown in Figure 2a. The EELS data were extracted from a spectrum image where both core-loss and low-loss EELS was simultaneously acquired. The spectrum in Figure 7c was stripped of the pre-edge background and deconvolved to represent a single scattering distribution.

XP spectra were measured with a Versa Probe III from Physical Electronics. UV Vis diffuse reflectance spectra were recorded with an Agilent Cary 5000 spectrophotometer equipped with an integrating sphere and PTFE as 100% reflection reference.

Photoelectrochemical (PEC) Characterization. The measurements were carried out with a PEC cell (WAT Venture) operating in a conventional three-electrode configuration. A platinum wire and a 1 M Ag/AgCl electrode were used as counter and reference electrodes, respectively. The produced thin films on FTO were used as working

DOI: 10.1021/acs.inorgchem.9b00327
Inorg. Chem. 2019, 58, 9655−9662

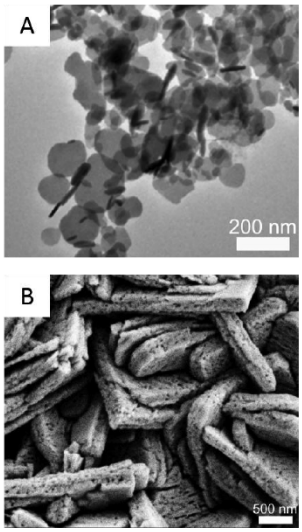

Figure 2. Electronic micrographs of (A) mössbauerite and (B) nanoporous composite WO_3/mössbauerite photoanode.

electrodes. All current values of the photoanodes were recorded versus 1 M Ag/AgCl and converted vs RHE according to E_{RHE} (volt) = $E_{1M\ Ag/AgCl}$ + (0.059 × pH). The supporting electrolyte was 0.1 M Na_2SO_4 solution buffered to pH 7 by 0.1 M potassium phosphate. The electrolyte was prepared with Milli-Q water (18.3 Ω cm).

A potentiostat (SP-150, BioLogic) was employed to record the electrochemical data. The light source for all data presented in this work was an AM 1.5G solar simulator (100 mW/cm^2, class-AAA 94023A, Newport). Photoanodes were illuminated from the backside. In a typical linear square voltammetry (LSV), the voltage was swept linearly from negative to positive potential direction at a rate of 10 mV/s. Mott–Schottky measurements were performed at three different frequencies, i.e., 10, 100, and 1000 Hz, and analyzed with EC Lab Software.

Computational Methods. Spin-polarized DFT calculations were performed using the projector augmented wave (PAW)[30] formalism and the generalized gradient approximation (GGA) method with Perdew–Burke–Ernzerhof (PBE) exchange-correlation functional as implemented in the Vienna Ab Initio Simulation Package (VASP).[31−33] The DFT-D3 method of Grimme was employed to evaluate the dispersion contribution for the adsorption.[34] The cutoff energy of 500 eV for the plane-wave basis set has been used. The convergence criteria of 10^{-5} eV and 10^{-2} eV/A were used for the energy and forces (in geometry optimizations) convergence, respectively. DFT+U theory was applied with the $U-J$ values of 3.7 eV.[35]

The 1T polytype (O1 geometry) was used to represent the structures of mössbauerite. On the basis of test calculations, a $\sqrt{3} \times 2\sqrt{3}$ supercell was adopted to accommodate the carbonate anion ($CO3^{2-}$) and three water molecules in the interlayer space ($Fe^{III}{}_6O_4(OH)_8[CO_3]*3H_2O$); the total magnetic moment was fixed at 30 μ_B per cell and 4 × 3 × 2 k-point sampling[36] was consistently used.

■ RESULTS AND DISCUSSSION

Structural Characterization. For the XRD analysis of tungsten trioxide, the thin films were mechanically removed from the FTO-glass to avoid reflection peaks of tin oxide. The diffractogram shows that the thin film consists only of tungsten trioxide (Figure S1).

Synchrotron high-energy X-ray diffraction of the highly disordered carbonate interlayered mössbauerite was published in a previous work.[26] The diffractogram indicates a turbostratic disordered layered material with a d-spacing of 7.0 Å. As stated in the previous work on a mössbauerite electrocatalyst, the lack of an integral 00l-series might be related to an interstratification of varying d-spacings.

The semiconducting nature of mössbauerite and the size of the bandgap were confirmed by quantum mechanics. Starting with published structures of related LDH, the crystal structure of carbonate interlayered mössbauerite was optimized by DFT methods (Figure 1A). The total density of states (TDOS) and partial density of states (PDOS) projected on Fe 3d and O 2p atomic orbitals confirm mössbauerite to be semiconducting (Figure 1B). In very good agreement with experimental observations, the band gap between the spin-up valence band and spin-down conduction band calculated via DFT+U was found to be 1.8 eV. The former and the latter are mainly contributed from O 2p and Fe 3d orbitals, respectively.

TEM micrographs show the 2D structure of mössbauerite, consisting of intergrown hexagonal nanoplatelets (Figure 2A).[37] The length and thickness of the nanoplatelets are around 50–200 nm and 10–20 nm, respectively. Figure 2B depicts a representative SEM image of the composite photoanode WO_3/mössbauerite. Since the amount of mössbauerite was very small, the morphology of the nanoporous tungsten trioxide plates remains unchanged. The WO_3 plates are several micrometers large and display a thickness of approximately 200 nm, while the nanoporous structure is visible over the whole crystallites.

The chemical states of mössbauerite were analyzed by XPS (Figure 3). The sample was sputtered with Ar ions after introducing the sample into the XPS chamber to remove adsorbed hydrocarbons. In mössbauerite, all Fe^{3+} cations are octahedrally coordinated with O^{2-} or OH^- comparable to the alpha phase of FeOOH (goethite).[38] The Fe 2p energy region in the XP spectrum resembles the one previously reported for goethite.[38] Curve-fitting of mixed iron oxyhydroxide species however is difficult due to varying peak shapes, varying satellite intensities and satellite overlap.

The main peaks were deconvoluted into two Fe $2p_{3/2}$/Fe $2p_{1/2}$ doublets with an additional satellite peak for each. The maxima of the peaks are found at 710.4, 712.5, and 718.2 eV for Fe $2p_{3/2}$ and 724.8, 732.6, and 742.6 eV for Fe $2p_{1/2}$, respectively, and are in good agreement with goethite.[38] Fitting a Gupta and Sen multiplet splitting to the XP spectrum would yield no additional information.[39] In the O 1s spectrum, three peaks can be identified and assigned to oxidic Fe–O (529.6 eV), hydroxide Fe–OH (531.2 eV) and water in the interlayer or external surface of mössbauerite.[40] The C 1s spectrum is dominated by an impurity species related to tape used to attach the powder sample to the measurement stage. Additionally, C–O and C=O peaks are present at 286.0 and 288.7 eV, confirming the presence of carbonate as the counteranion of the mössbauerite.[41]

The optical bandgap of mössbauerite was measured by UV–vis diffuse reflectance spectroscopy, and the calculated Tauc plot is shown in Figure 4A. The experimentally determined bandgap for the indirect transition is 1.8 eV. This value might be slightly shifted by the influence of an Urbach tail, originating from less crystalline domains or defect states, as

DOI: 10.1021/acs.inorgchem.9b00327
Inorg. Chem. 2019, 58, 9655−9662

Inorganic Chemistry Article

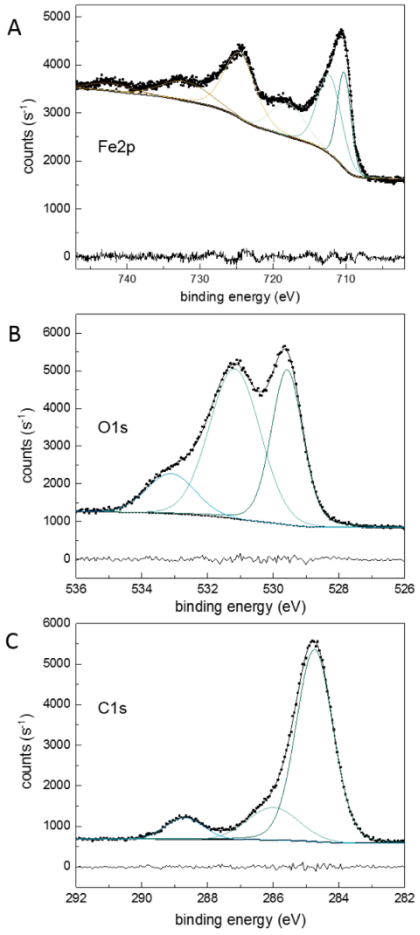

Figure 3. XP spectra of mössbauerite.

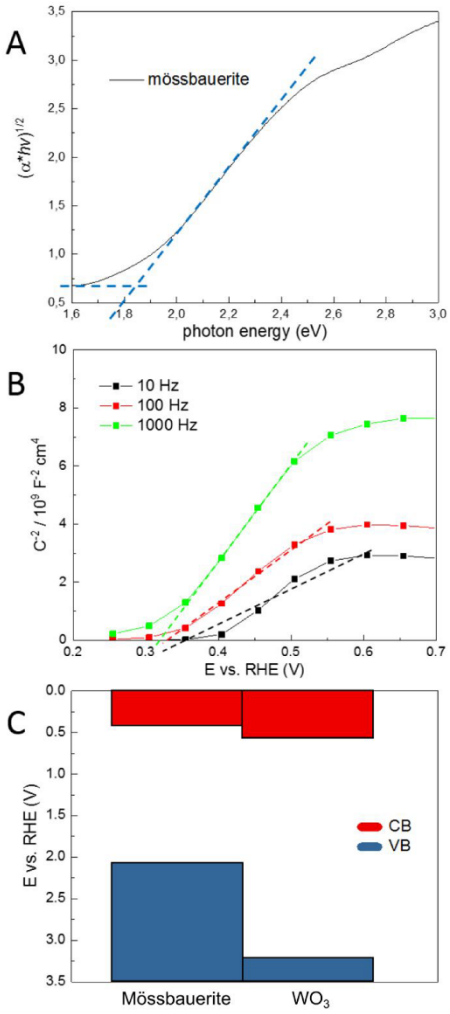

Figure 4. (A) UV–vis and (B) Mott–Schottky plots of mössbauerite at different frequencies. (C) Schematic illustration of valence band (VB) and conduction band (CB) edge positions for tungsten trioxide and mössbauerite.

frequently encountered in semiconducting materials.[42] The bandgap of the direct transition is 2.1 eV but will be disregarded in the following because the PEC experiments are conducted at room temperature where sufficient energy is supplied to change the impulse of electrons during the band transition.

Photoelectrochemistry. The flatband position of mössbauerite was determined by means of Mott–Schottky (MS) analysis at 10, 100, and 1000 Hz (Figure 4B). The positive slope of the reciprocal square of the capacitance versus the potential indicates the material to be an n-type semiconductor. The MS plots measured at different frequencies are consistent and put the flatband of mössbauerite at 0.34 V vs RHE. This value is comparable with literature reports on both oxide and hydroxide species of iron. For instance, for hematite values between 0.71 and 0.47 V vs RHE were reported, depending vastly on sample preparation and morphology.[43] With increasing hydroxide content, the flatband is shifted toward lower potentials. Mössbauerite being an iron oxyhydroxide is more similar to ferrihydrite for which a flatband potential of around 0.3 V vs RHE was reported.[22]

The resulting valence band edge (VBE) and conduction band edge (CBE) positions of mössbauerite vs RHE are plotted in Figure 4C and compared to those of WO_3. The different positions of the VBE and CBE would yield a type-II heterojunction upon contact of both n-type semiconductors.[44]

DOI: 10.1021/acs.inorgchem.9b00327
Inorg. Chem. 2019, 58, 9655−9662

The formation of interfaces between two semiconductors of the same type but different band edge positions can improve the charge carrier separation of photoelectrodes. The comparison of the open-circuit potential of WO_3 before and after mössbauerite functionalization shows that the photo-induced potential drop was slightly larger for the heterojunction (Figure S2). This is highly likely to originate from the more negative CBE position of mössbauerite in comparison to WO_3.

For the photoelectrochemical characterization of mössbauerite, LSV curves of electrodes prepared by EPD were recorded in 0.1 M Na_2SO_4 (pH 7) at a scan rate of 10 mV s^{-1}. Mössbauerite developed a small anodic current of approximately 15 μA cm^{-2} at 1.23 V vs RHE current density and no upsurge could be observed upon illumination (Figure 5A). The lack of photocurrent may be due to low electronic conductivity combined with fast surface recombination of charge carriers at interconnected mössbauerite nanoplatelets.

Applying a modified synthesis of Diao,[29] we were able to prepare a WO_3 thin film photoanode with very good PEC water oxidation performance (Figure 5B) as reflected in a significant photocurrent of 1.44 mA cm^{-2} at 1.23 V vs RHE. The onset potential, i.e., the value at which photocurrent can be detected, for water oxidation is about 0.65 V vs RHE. Since water oxidation is a kinetically demanding process, it is impossible to determine directly the number of photogenerated holes reaching the electrode−electrolyte interface. Contrary to water, the oxidation of sulfite anions to sulfate anions is a very fast process. Using sulfite as a hole scavenger therefore allows us to determine the number of surface-reaching holes available for oxidative processes. When oxidizing sulfite instead of water, the neat WO_3 photoanode generates a photocurrent of 1.64 mA cm^{-2} at 1.23 V vs RHE (Figure 5B). After functionalization with mössbauerite, the heterojunction photoanode shows a small but significant increase in photocurrent density during sulfite oxidation at a potential below 1.15 V vs RHE indicating improved charge carrier separation at the WO_3/mössbauerite heterojunction.

In the absence of sulfite, a similar tendency of an enhanced photocurrent density during PEC water oxidation can be observed on the WO_3/mössbauerite heterojunction photoanode (Figure 5C). An upsurge in photocurrent during LSV in comparison to WO_3 photoanode was recorded after coating the surface with mössbauerite. After having exceeded the optimal loading amount of 4 μg of mössbauerite, the photocurrent decreased (Figure S3).

This is a frequent observation for composite electrodes, where after reaching the optimized amount of catalyst, further addition leads to a decrease of semiconductor−catalyst interfaces being exposed to the electrolyte. Though the photocurrent of the composite electrode is among the highest for WO_3 photoanodes, the catalytic enhancement of the current density remains lower than the value obtained for the oxidation of sulfite as hole scavenger (Figure 5B). Above the thermodynamic potential for water oxidation (1.23 V vs RHE), the bare WO_3 photoanode exhibits a higher value for sulfite oxidation in comparison to the heterojunction electrode; a phenomenon often occurring for composite photoelectrodes based on tungsten trioxide.[45]

Chronoamperometry at 1.23 V vs RHE under interrupted illumination shows that mössbauerite advances the photocurrent of the WO_3 photoanode by 10% from 1.11 to 1.22 mA cm^{-2} (Figure 6). The slight decay in photocurrent during the

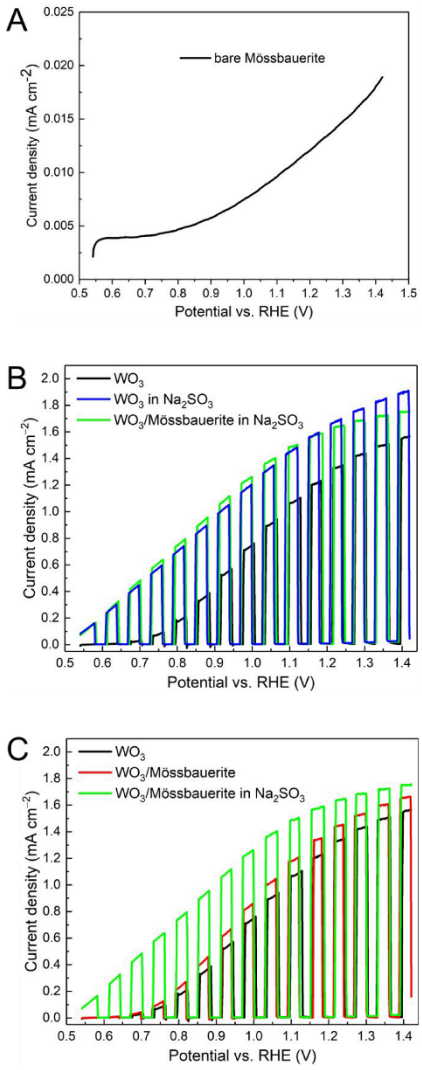

Figure 5. LSV at a scan rate of 10 mV s^{-1} under sequentially interrupted backlight AM 1.5G illumination at pH 7: (A) bare mössbauerite, (B) comparison of bare WO_3 and WO_3/mössbauerite in the presence of sulfite anions (50 mM) as hole scavenger, (C) comparison of bare WO_3 and WO_3/mössbauerite. The black curves and red curve correspond to PEC water oxidation without sulfite addition.

CA can be mainly attributed to WO_3 because the shape of the curvature is similar to the pristine tungsten trioxide photoanode. It should be noted that the WO_3 photoanode was not subject to postannealing treatment before mössbauerite deposition.[46] Such treatment under nonambient atmosphere

DOI: 10.1021/acs.inorgchem.9b00327
Inorg. Chem. 2019, 58, 9655−9662

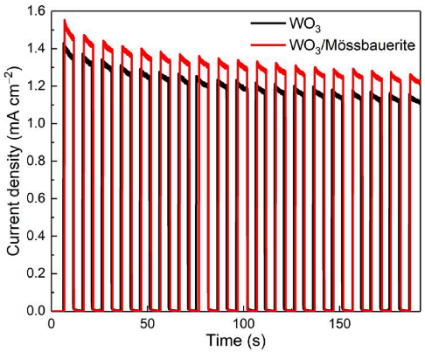

Figure 6. Chronoamperometry during PEC water oxidation on photoanodes WO_3 and WO_3/mössbauerite at 1.23 V vs RHE under chopped illumination at pH 7 under sequentially interrupted backlight AM 1.5G illumination.

is usually necessary to obtain current densities above 1 mA cm^{-2} at 1.23 V vs RHE.[47] The percent increase of photocurrent by mössbauerite depends on the initial photocurrent of the tungsten trioxide. We measured the PEC water oxidation with the heterojunction system but used a WO_3 photoanode exhibiting a poorer initial photocurrent (Figure S4).[11] After mössbauerite functionalization, the photocurrent increased from 18 to 26 μA cm^{-2} at 1.23 V vs RHE.

The difference between mössbauerite and the iron oxyhydroxide ferrihydrite, which is known to be a very efficient hole storage layer, becomes clear when analyzing the curvature of the chronoamperometry. Upon interruption of illumination, the current of the photoanode WO_3/mössbauerite drops to zero without the occurrence of a cathodic overshoot, i.e., a current drop below zero accompanied by a subsequent rapid rise to zero. The described cathodic overshoot is the characteristic behavior of a hole storage layer such as provided by ferrihydrite. A complementary bare mössbauerite electrode, containing the same amount as for the heterojunction photoanode, did not develop any noticeable photocurrent at 1.23 V vs RHE (Figure S6).

A more detailed analytical study of the mössbauerite catalytic interface after PEC water oxidation is presented in Figure 7. Here, a separate mössbauerite electrode was prepared via EPD and utilized for water oxidation at 1.23 V vs RHE for 60 min. The sample was mechanically removed from the substrate, dispersed in hexane and deposited on a TEM grid. The corresponding HAADF micrograph and SAEDP are presented in Figure 7a,b. The rotational average of this diffraction pattern is inset in yellow, and a simulated powder diffraction pattern is overlaid in black. The pattern was generated using the structure file from DFT+U in the Mercury program and was blurred to more closely simulate the electron diffraction conditions. Since the mössbauerite plates rest atop a thin amorphous carbon TEM grid, the amorphous carbon rings present a very high background contribution, obscuring some of the weaker reflections. Nevertheless, a number of reflections corresponding to strongly diffracting atomic planes are visible, and these are annotated with dashed rings over part of the figure. Miller indices accompany these rings. The outer three rings have two indices each, as multiple strong reflections are present in the angular range but cannot be individually distinguished in this data set. Figure 7c shows an EEL spectrum from the agglomerated nanoplates after PEC water oxidation. Energy-loss near-edge fine structure (ELNES) features for the oxygen K and iron $L_{2,3}$ edges are both visible and bear a striking resemblance to Fe_2O_3, strongly suggesting that the oxidation state is primarily +3.[48]

Electrochemical impedance spectroscopy measurements performed under illumination show a smaller arc radius for the heterojunction; hinting toward improved charge transfer upon mössbauerite functionalization (Figure S5). The rise in photocurrent of the mössbauerite-functionalized WO_3 photoanode thus originates from (i) improved charge carrier separation as a consequence of the type-II heterojunction formation and (ii) an improved hole collection efficiency due to mössbauerite acting as a water oxidation catalyst.

■ CONCLUSION

We have investigated mössbauerite as a cocatalyst for PEC water oxidation on tungsten trioxide thin film electrodes.

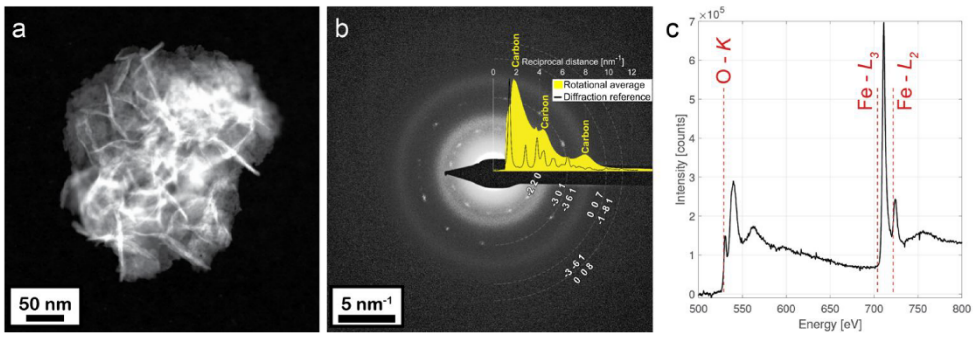

Figure 7. (A) HAADF micrograph of a mössbauerite nanoplates after PEC water oxidation at 1.23 V vs RHE. (B) SAEDP from the mössbauerite nanoplates. A rotational average of this SAEDP is in the inset and is overlaid with a simulated powder diffraction pattern from DFT+U. Selected reflections are indexed. (C) EEL spectra of the mössbauerite nanoplates.

DOI: 10.1021/acs.inorgchem.9b00327
Inorg. Chem. 2019, 58, 9655−9662

Mössbauerite-functionalized WO_3 photoanodes reached a photocurrent of 1.22 mA cm^{-2} at 1.23 V vs RHE during PEC water oxidation. Mott–Schottky measurements in combination with UV–vis spectroscopy show mössbauerite to be an n-type semiconductor with a band gap of 1.8 eV and a flatband potential of +0.34 V vs RHE. The XP spectra confirm all Fe^{3+} cations to be octahedrally coordinated with O^{2-} or OH^- similar to the structurally related goethite.

PEC oxidation of sulfite as hole scavenger on mössbauerite-modified WO_3 photoanodes indicates an enhancement of the charge separation by the type-II heterojunction created. Our work demonstrates that, in addition to the known electrocatalytic activity of mössbauerite, its semiconducting nature and band alignment additionally improve the photocurrent due to better charge carrier separation at the interface. Our results highlight the potential of mössbauerite in the construction of heterojunctions for improving the performance of photoanodes.

■ ASSOCIATED CONTENT

Supporting Information

The Supporting Information is available free of charge on the ACS Publications website at DOI: 10.1021/acs.inorgchem.9b00327.

PXRD of WO_3, open-circuit photovoltages, LSV of WO_3 with stepwise addition of mössbauerite, CA heterojunction photoanodes, EIS of WO_3 and WO_3/mössbauerite photoanode, CA of pure mössbauerite (PDF)

■ AUTHOR INFORMATION

Corresponding Authors

*E-mail: adam.slabon@mmk.su.se. Phone: +49 (0) 173 1560 468 (A.S.).

*E-mail josef.breu@uni-bayreuth.de. Phone: +49 (0) 921 55-2530 (J.B.).

ORCID

Josef Breu: 0000-0002-2547-3950

Adam Slabon: 0000-0002-4452-1831

Author Contributions

#M.E. and Z.M. contributed equally to this work. J.B. and A.S. initiated the research project. M.E. synthesized mössbauerite and carried out most of its structural characterization. Z.M. synthesized WO_3 photoelectrodes and did all electrochemical experiments. M.E. and S.H. carried out the XPS experiments. T.T. performed the TEM experiments; P.L. and P.N. calculated and analyzed the electronic band structure.

Notes

The authors declare no competing financial interest.

■ ACKNOWLEDGMENTS

M.E. thanks the Hanns-Seidel foundation for a doctoral scholarship. Z.M. thanks the China Scholarship Council for a Ph.D. scholarship. J.B. is grateful to the Deutsche Forschungsgemeinschaft (DFG) in the framework of the SFB 840. Access to computing and storage facilities owned by parties and projects contributing to the National Grid Infrastructure MetaCentrum, provided under the programme "Projects of Large Research, Development, and Innovations Infra-structures" (CESNET LM2015042), is greatly appreciated. P.N. and J.B. gratefully acknowledge financial support from the Bavarian-Czech Academic Agency (Bayerisch-Tschechische Hochschulagentur) in the framework of the project "Entwicklung und Designprinzipien für strukturierte Materialien" financed by funds of the Free State of Bavaria. T.T. acknowledges support from the Electron Microscopy Center (EMC) at Stockholm University as well as funding from the Swedish Research Council (Project No. 2016-05113). This work was financially supported by Stockholm University.

■ REFERENCES

(1) McKone, J. R.; Lewis, N. S.; Gray, H. B. Will Solar-Driven Water-Splitting Devices See the Light of Day? *Chem. Mater.* **2014**, *26*, 407–414.

(2) Sivula, K.; Le Formal, F.; Grätzel, M. WO_3-Fe_2O_3 Photoanodes for Water Splitting: A Host Scaffold, Guest Absorber Approach. *Chem. Mater.* **2009**, *21*, 2862–2867.

(3) Nocera, D. G. Solar Fuels and Solar Chemicals Industry. *Acc. Chem. Res.* **2017**, *50*, 616–619.

(4) Sougrati, M. T.; Arayamparambil, J. J.; Liu, X.; Mann, M.; Slabon, A.; Stievano, L.; Dronskowski, R. Carbodiimides as Energy Materials: Which Directions for a Reasonable Future? *Dalt. Trans.* **2018**, *47*, 10827–10832.

(5) Seabold, J. A.; Choi, K. S. Effect of a Cobalt-Based Oxygen Evolution Catalyst on the Stability and the Selectivity of Photo-Oxidation Reactions of a WO_3 photoanode. *Chem. Mater.* **2011**, *23*, 1105–1112.

(6) Song, F.; Moré, R.; Schilling, M.; Smolentsev, G.; Azzaroli, N.; Fox, T.; Luber, S.; Patzke, G. R. $\{Co_4O_4\}$ and $\{Co_xNi_{4-X}O_4\}$ Cubane Water Oxidation Catalysts as Surface Cut-Outs of Cobalt Oxides. *J. Am. Chem. Soc.* **2017**, *139*, 14198–14208.

(7) Nocera, D. G. The Artificial Leaf. *Acc. Chem. Res.* **2012**, *45*, 767–776.

(8) Davi, M.; Mann, M.; Ma, Z.; Schrader, F.; Drichel, A.; Budnyk, S.; Rokicinska, A.; Kustrowski, P.; Dronskowski, R.; Slabon, A. An MnNCN-Derived Electrocatalyst for $CuWO_4$ Photoanodes. *Langmuir* **2018**, *34*, 3845–3852.

(9) Fujishima, A.; Honda, K. Electrochemical Photolysis of Water at a Semiconductor Electrode. *Nature* **1972**, *238*, 37–38.

(10) Reed, P. J.; Mehrabi, H.; Schichtl, Z. G.; Coridan, R. H. Enhanced Electrochemical Stability of TiO_2-Protected, Al-Doped ZnO Transparent Conducting Oxide Synthesized by Atomic Layer Deposition. *ACS Appl. Mater. Interfaces* **2018**, *10*, 43691–43698.

(11) Davi, M.; Ogutu, G.; Schrader, F.; Rokicinska, A.; Kustrowski, P.; Slabon, A. Enhancing Photoelectrochemical Water Oxidation Efficiency of WO_3/α-Fe_2O_3 Heterojunction Photoanodes by Surface Functionalization with CoPd Nanocrystals. *Eur. J. Inorg. Chem.* **2017**, *2017*, 4267–4274.

(12) Zhao, Z.; Butburee, T.; Lyv, M.; Peerakiatkhajohn, P.; Wang, S.; Wang, L.; Zheng, H. Etching Treatment of Vertical WO_3 nanoplates as a Photoanode for Enhanced Photoelectrochemical Performance. *RSC Adv.* **2016**, *6*, 68204–68210.

(13) Davi, M.; Peter, S.; Slabon, A. Fabrication of Hierarchically Ordered Porous Scheelite-Related Monoclinic $BiVO_4$ Nanotubes by Electrochemical Deposition. *Funct. Mater. Lett.* **2016**, *09*, 1650036.

(14) Ma, Z.; Linnenberg, O.; Rokicinska, A.; Kustrowski, P.; Slabon, A. Augmenting the Photocurrent of $CuWO_4$ Photoanodes by Heat Treatment in the Nitrogen Atmosphere. *J. Phys. Chem. C* **2018**, *122*, 19281–19288.

(15) Chen, Z. B.; Jaramillo, T. F.; Deutsch, T. G.; Kleiman-Shwarsctein, A.; Forman, A. J.; Gaillard, N.; Garland, R.; Takanabe, K.; Heske, C.; Sunkara, M.; McFarland, E. W.; Domen, K.; Miller, E. L.; Turner, J. A.; Dinh, H. N. Accelerating Materials Development for Photoelectrochemical Hydrogen Production: Standards for Methods, Definitions, and Reporting Protocols. *J. Mater. Res.* **2010**, *25*, 3–16.

(16) Zandi, O.; Beardslee, J. A.; Hamann, T. Substrate Dependent Water Splitting with Ultrathin α-Fe2O3 Electrodes. *J. Phys. Chem. C* **2014**, *118*, 16494–16503.

DOI: 10.1021/acs.inorgchem.9b00327
Inorg. Chem. 2019, 58, 9655–9662

(17) Lewis, N. S. Developing a Scalable Artificial Photosynthesis Technology through Nanomaterials by Design. *Nat. Nanotechnol.* **2016**, *11*, 1010−1019.
(18) Seo, J.; Nishiyama, H.; Yamada, T.; Domen, K. Visible-Light-Responsive Photoanodes for Highly Active, Stable Water Oxidation. *Angew. Chem., Int. Ed.* **2018**, *57*, 8396−8415.
(19) Kwong, W. L.; Lee, C. C.; Messinger, J. Transparent Nanoparticulate FeOOH Improves the Performance of a WO_3 Photoanode in a Tandem Water-Splitting Device. *J. Phys. Chem. C* **2016**, *120*, 10941−10950.
(20) Kim, J. Y.; Youn, D. H.; Kang, K.; Lee, J. S. Highly Conformal Deposition of an Ultrathin FeOOH Layer on a Hematite Nanostructure for Efficient Solar Water Splitting. *Angew. Chem., Int. Ed.* **2016**, *55*, 10854−10858.
(21) Morales-Guio, C. G.; Liardet, L.; Hu, X. Oxidatively Electrodeposited Thin-Film Transition Metal (Oxy)Hydroxides as Oxygen Evolution Catalysts. *J. Am. Chem. Soc.* **2016**, *138*, 8946−8957.
(22) Liu, G.; Shi, J.; Zhang, F.; Chen, Z.; Han, J.; Ding, C.; Chen, S.; Wang, Z.; Han, H.; Li, C. A Tantalum Nitride Photoanode Modified with a Hole-Storage Layer for Highly Stable Solar Water Splitting. *Angew. Chem., Int. Ed.* **2014**, *53*, 7295−7299.
(23) Yu, F.; Li, F.; Yao, T.; Du, J.; Liang, Y.; Wang, Y.; Han, H.; Sun, L. Fabrication and Kinetic Study of a Ferrihydrite-Modified $BiVO_4$ Photoanode. *ACS Catal.* **2017**, *7*, 1868−1874.
(24) Davi, M.; Schrader, F.; Scholz, T.; Ma, Z.; Rokicinska, A.; Dronskowski, R.; Kustrowski, P.; Slabon, A. $SrTaO_2N$ Nanowire Photoanode Modified with a Ferrihydrite Hole-Storage Layer for Photoelectrochemical Water Oxidation. *ACS Appl. Nano Mater.* **2018**, *1*, 869−876.
(25) Wang, Q.; O'Hare, D. Recent Advances in the Synthesis and Application of Layered Double Hydroxide (LDH) Nanosheets. *Chem. Rev.* **2012**, *112*, 4124−4155.
(26) Ertl, M.; Andronescu, C.; Moir, J.; Zobel, M.; Wagner, F. E.; Barwe, S.; Ozin, G.; Schuhmann, W.; Breu, J. Oxygen Evolution Catalysis with Mössbauerite—A Trivalent Iron-Only Layered Double Hydroxide. *Chem. - Eur. J.* **2018**, *24*, 9004−9008.
(27) Génin, J.-M. R.; Mills, S. J.; Christy, A. G.; Guérin, O.; Herbillon, A. J.; Kuzmann, E.; Ona-Nguema, G.; Ruby, C.; Upadhyay, C. Mössbauerite, $Fe^{3+}{}_6O_4(OH)_8[CO_3]\cdot 3H_2O$, the Fully Oxidized "green Rust" Mineral from Mont Saint-Michel Bay, France. *Mineral. Mag.* **2014**, *78*, 447−465.
(28) Barthélémy, K.; Naille, S.; Despas, C.; Ruby, C.; Mallet, M. Carbonated Ferric Green Rust as a New Material for Efficient Phosphate Removal. *J. Colloid Interface Sci.* **2012**, *384*, 121−127.
(29) Hu, D.; Diao, P.; Xu, D.; Wu, Q. Gold/WO_3 Nanocomposite Photoanodes for Plasmonic Solar Water Splitting. *Nano Res.* **2016**, *9*, 1735−1751.
(30) Perdew, J. P.; Burke, K.; Ernzerhof, M. Generalized Gradient Approximation Made Simple. *Phys. Rev. Lett.* **1996**, *77*, 3865−3868.
(31) Blöchl, P. E. Projector Augmented-Wave Method. *Phys. Rev. B* **1994**, *50*, 17953−17979.
(32) Kresse, G.; Furthmuller, J. Efficiency of Ab-Initio Total Energy Calculations for Metals and Semiconductors Using a Plane-Wave Basis Set. *Comput. Mater. Sci.* **1996**, *6*, 15−50.
(33) Kresse, G.; Joubert, D. From Ultrasoft Pseudopotentials to the Projector Augmented-Wave Method. *Phys. Rev. B: Condens. Matter Mater. Phys.* **1999**, *59*, 1758−1775.
(34) Grimme, S.; Antony, J.; Ehrlich, S.; Krieg, H. A Consistent and Accurate Ab Initio Parametrization of Density Functional Dispersion Correction (DFT-D) for the 94 Elements H-Pu. *J. Chem. Phys.* **2010**, *132*, 154104.
(35) Santos-Carballal, D.; Roldan, A.; Grau-Crespo, R.; de Leeuw, N. H. A DFT Study of the Structures, Stabilities and Redox Behaviour of the Major Surfaces of Magnetite Fe_3O_4. *Phys. Chem. Chem. Phys.* **2014**, *16*, 21082−21097.
(36) Monkhorst, H. J.; Pack, J. D. Special Points for Brillouin-Zone Integrations. *Phys. Rev. B* **1976**, *13*, 5188−5192.
(37) Chaturvedi, A.; Slabon, A.; Hu, P.; Feng, S.; Zhang, K.; Prabhakar, R.; Kloc, C. Rapid Synthesis of Transition Metal Dichalcogenide Few-Layer Thin Crystals by the Microwave-Induced-Plasma Assisted Method. *J. Cryst. Growth* **2016**, *450*, 140−147.
(38) Grosvenor, A. P.; Kobe, B. A.; Biesinger, M. C.; McIntyre, N. S. Investigation of Multiplet Splitting of Fe 2p XPS Spectra and Bonding in Iron Compounds. *Surf. Interface Anal.* **2004**, *36*, 1564−1574.
(39) Stoch, J.; Capecki, A. Decomposition of $2p_{3/2}$ Bands in XPS Spectra of Fe, Co and Ni Compounds. *Surf. Interface Anal.* **1990**, *15*, 206−210.
(40) Biesinger, M. C.; Payne, P. P.; Grosvenor, A. P.; Lau, L. W. M.; Gerson, A. R.; Smart, R. St. C. Resolving surface chemical states in XPS analysis of first row transition metals, oxides and hydroxides: Cr, Mn, Fe, Co and Ni. *Appl. Surf. Sci.* **2011**, *257*, 2717−2730.
(41) Mullet, M.; Khare, V.; Ruby, C. XPS Study of Fe(II)-Fe(III) (Oxy)Hydroxycarbonate Green Rust Compounds. *Surf. Interface Anal.* **2008**, *40*, 323−328.
(42) Dunstan, D. J. Evidence for a Common Origin of the Urbach Tails in Amorphous and Crystalline Semiconductors. *J. Phys. C: Solid State Phys.* **1982**, *15*, L419.
(43) Björksten, U.; Moser, J.; Grätzel, M. Photoelectrochemical Studies on Nanocrystalline Hematite Films. *Chem. Mater.* **1994**, *6*, 858−863.
(44) Davi, M.; Drichel, A.; Mann, M.; Scholz, T.; Schrader, F.; Rokicinska, A.; Kustrowski, P.; Dronskowski, R.; Slabon, A. Enhanced Photoelectrochemical Water Oxidation Efficiency of $CuWO_4$ Photoanodes by Surface Modification with Ag_2NCN. *J. Phys. Chem. C* **2017**, *121*, 26265−26274.
(45) Rao, P. M.; Cai, L. L.; Liu, C.; Cho, I. S.; Lee, C. H.; Weisse, J. M.; Yang, P. D.; Zheng, X. L. Simultaneously Efficient Light Absorption and Charge Separation in $WO_3/BiVO_4$ Core/Shell Nanowire Photoanode for Photoelectrochemical Water Oxidation. *Nano Lett.* **2014**, *14*, 1099−1105.
(46) Ma, M.; Zhang, K.; Li, P.; Jung, M. S.; Jeong, M. J.; Park, J. H. Dual Oxygen and Tungsten Vacancies on a WO_3 Photoanode for Enhanced Water Oxidation. *Angew. Chem., Int. Ed.* **2016**, *55*, 11819−11823.
(47) Zhang, J.; Chang, X.; Li, C.; Li, A.; Liu, S.; Wang, T.; Gong, J. WO_3 Photoanodes with Controllable Bulk and Surface Oxygen Vacancies for Photoelectrochemical Water Oxidation. *J. Mater. Chem. A* **2018**, *6*, 3350−3354.
(48) Pan, Y.; Brown, A.; Brydson, R.; Warley, A.; Li, A.; Powell, J. Electron Beam Damage Studies of Synthetic 6-Line Ferrihydrite and Ferritin Molecule Cores within a Human Liver Biopsy. *Micron* **2006**, *37*, 403−411.

DOI: 10.1021/acs.inorgchem.9b00327
Inorg. Chem. 2019, 58, 9655−9662

6.2.1. Supporting Information

SUPPORTING INFORMATION

Mössbauerite as Iron-only Layered Oxyhydroxide Catalyst for WO_3 Photoanodes

Michael Ertl[†,a], Zili Ma[‡,a], Thomas Thersleff[§], Pengbo Lyu[⊥], Sven Huettner[ǁ], Petr Nachtigall[⊥], Josef Breu[†,*], and Adam Slabon[§,*]

[†]Bavarian Polymer Institute and Department of Chemistry, University of Bayreuth, Universitätsstraße 30, D-95440, Germany

[‡]Institute of Inorganic Chemistry, RWTH Aachen University, Landoltweg 1, D-52056 Aachen, Germany

[ǁ]Organic and Hybrid Electronics, University of Bayreuth, Universitätsstraße 30, D-95440, Germany

[⊥]Department of Physical and Macromolecular Chemistry, Faculty of Sciences, Charles University, Hlavova 8, 128 43 Prague 2, Czech Republic

[§]Department of Materials and Environmental Chemistry, Stockholm University, Svante Arrhenius väg 16 C, 106 91 Stockholm, Sweden

[a]M.E. and Z.M. contributed equally.

Table of Content

Figure S1. Powder X-ray diffraction data of WO_3.

Figure S2. Open-circuit photovoltage of WO_3 and WO_3/Mössbauerite photoanodes.

Figure S3. LSV at a scan rate of 10 mV s^{-1} under sequentially interrupted backlight AM 1.5G illumination at pH 7 with stepwise addition of mössbauerite.

Figure S4. CA at 1.23 V vs. RHE and LSV at 10 mV s^{-1} of heterojunction photoanodes under AM 1.5G illumination in 0.1M Na_2SO_4 (pH 7) with WO_3 synthesized according to ref[1].

Figure S5. Photoelectrochemical impedance spectra of the WO_3 photoanode compared with the heterojunction WO_3/Mössbauerite photoanode.

Figure S6. CA at 1.23 V vs. RHE of bare mössbauerite under sequentially interrupted AM 1.5G illumination in 0.1M Na_2SO_4 (pH 7).

References

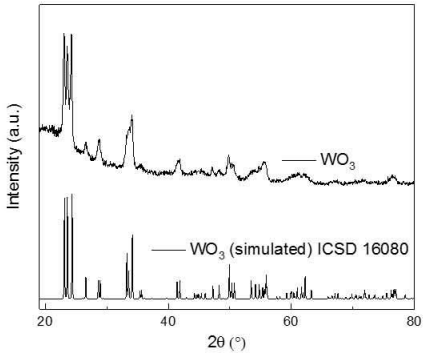

Figure S1. Powder X-ray diffraction data of WO_3.

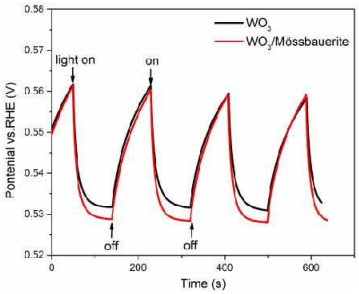

Figure S2. Open-circuit photovoltage of WO_3 and WO_3/Mössbauerite photoanodes upon light on and light off.

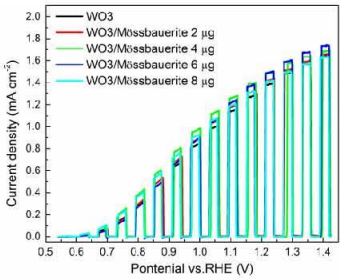

Figure S3. LSV at a scan rate of 10 mV s^{-1} under sequentially interrupted backlight AM 1.5G illumination at pH 7 with stepwise addition of mössbauerite.

S2

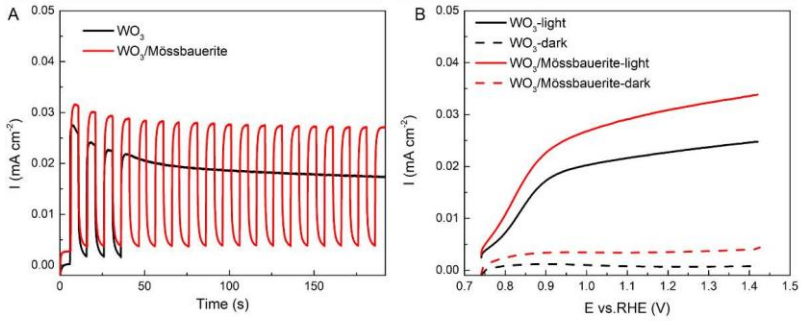

Figure S4. CA at 1.23 V vs. RHE and LSV at 10 mV s^{-1} of heterojunction photoanodes under AM 1.5G illumination in 0.1M Na_2SO_4 (pH 7) with WO_3 synthesized according to ref[1].

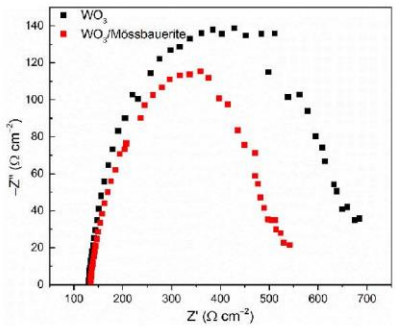

Figure S5. Photoelectrochemical impedance spectra of the WO_3 photoanode compared with the heterojunction WO_3/Mössbauerite photoanode. The EIS was measured at 1.0 V vs RHE in the ac. potential frequency range of 20 KHZ–0.2 Hz under AM 1.5G illumination.

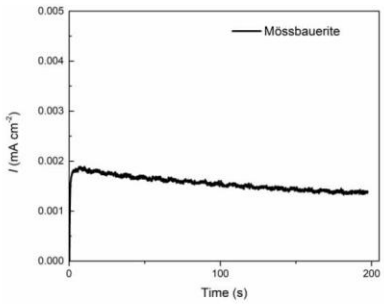

Figure S6. CA at 1.23 V vs. RHE of bare mössbauerite under sequentially interrupted AM 1.5G illumination in 0.1M Na_2SO_4 (pH 7).

S3

References

(1) Davi, M.; Ogutu, G.; Schrader, F.; Rokicinska, A.; Kustrowski, P.; Slabon, A. Enhancing Photoelectrochemical Water Oxidation Efficiency of $WO_3/\alpha\text{-}Fe_2O_3$ Heterojunction Photoanodes by Surface Functionalization with CoPd Nanocrystals. *Eur. J. Inorg. Chem.* **2017**, *2017*, 4267–4274.

6.3. In-depth Study on the Structure of Iron-Only Layered (Oxy-)Hydroxides

Pengbo Lyu,[†] Michael Ertl,[‡] Christopher J. Heard,[†] Lukáš Grajciar,[†] A.V. Radha,[‡] Thomas Martin,[‡] Josef Breu,[‡] Petr Nachtigall[†*]

Structure Determination of the Oxygen Evolution Catalyst Mössbauerite

Published in The Journal of Physical Chemistry C **2019**, *58*, 9655-9662.
Reprinted with permission, Copyright (2019) American Chemical Society.
Impact Factor (2019) J. Phys. Chem. C: 4.31
https://doi.org/10.1021/acs.jpcc.9b06061

† Department of Physical and Macromolecular Chemistry, Faculty of Sciences, Charles University, Hlavova 8, 128 43 Prague 2, Czech Republic
‡ Bavarian Polymer Institute and Department of Chemistry, University of Bayreuth, Universitätsstr. 30, 95440 Bayreuth, Germany

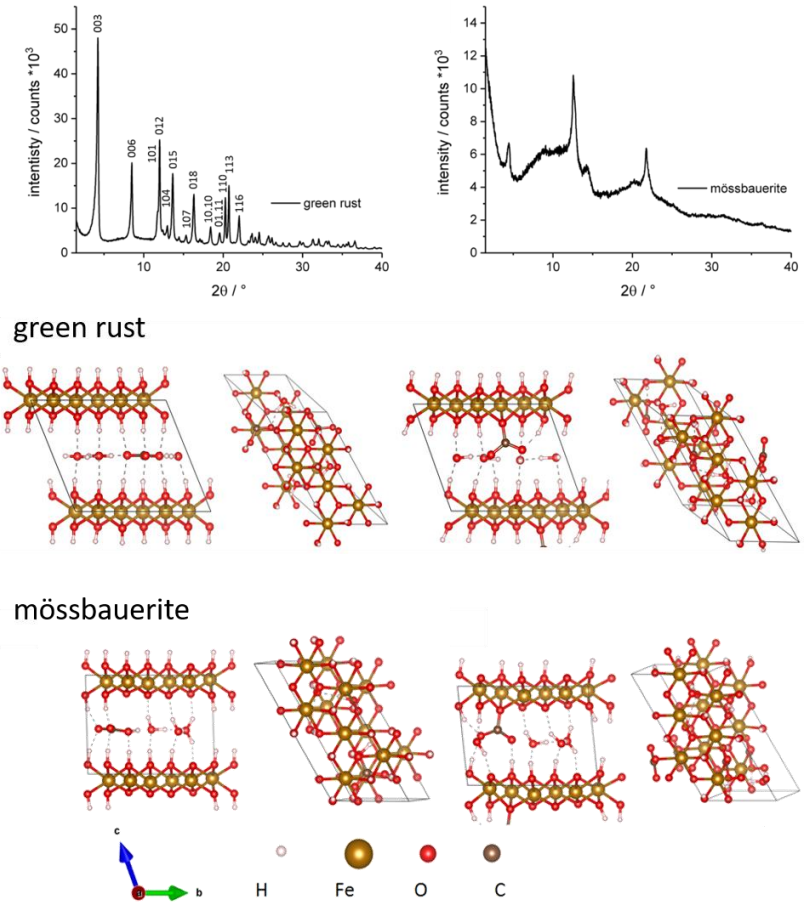

Individual Contributions:

The concept of the publication was developed by myself, Prof. Josef Breu, Pengbo Lyu and Prof. Petr Nachtigall in the framework of the Bavarian-Czech Academic Agency (BTHA). The manuscript was written by Pengbo Lyu, Prof. Petr Nachtigall, Prof. Josef Breu and myself. The computational part was done by Pengbo Lyu, Christopher Heard and Lukáš Grajciar. The refinement of the crystal structure and the characterization of mössbauerite was done by myself as well as the experimental part. Radha A. Venkataramana helped with the refinement. Thomas Martin helped with the refinement and the discussion of the results.

THE JOURNAL OF PHYSICAL CHEMISTRY C

Article

Cite This: J. Phys. Chem. C 2019, 123, 25157−25165

pubs.acs.org/JPCC

Structure Determination of the Oxygen Evolution Catalyst Mössbauerite

Pengbo Lyu,[†,§] Michael Ertl,[‡,§] Christopher J. Heard,[†] Lukáš Grajciar,[†] A.V. Radha,[‡] Thomas Martin,[‡] Josef Breu,[*,‡] and Petr Nachtigall[*,†]

[†]Department of Physical and Macromolecular Chemistry, Faculty of Sciences, Charles University, Hlavova 8, Prague 2 128 43, Czech Republic

[‡]Bavarian Polymer Institute and Department of Chemistry, University of Bayreuth, Universitätsstraße 30, Bayreuth D-95440, Germany

Supporting Information

ABSTRACT: Layered double hydroxides (LDHs) of various compositions have been shown to be potent photo- and electrocatalysts. Recently, mössbauerite, obtained by chemical oxidation of an all-iron, mixed-valence green rust (GR) LDH, was introduced as an efficient oxygen evolution reaction (OER) electrocatalyst. An accurate characterization of the structure of mössbauerite is necessary for a knowledge-based future optimization of OER performance. However, as is typical for layered materials, massive defects hamper the understanding of its true structure. In this work, we elucidate the structure of mössbauerite and gain insight into the structure−property relationships relevant to its potential as an OER catalyst. Density functional theory calculations show that upon oxidation of a GR precursor to mössbauerite, the direct grafting of interlayer anions to octahedral iron becomes energetically feasible. This indicates that the grafted and interlayer carbonate anions may coexist in a random interstratification. This prediction is supported by analysis of infrared spectroscopy and X-ray powder diffraction data, which show that an interstratified model with turbostratic planar disorder provides a good fit with the experiment.

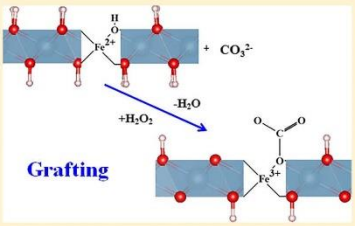

1. INTRODUCTION

Layered double hydroxides (LDHs) of various compositions have been identified as the best oxygen evolution catalysts with respect to overpotential.[1] LDHs consist of brucite-type layers that carry a positive charge because of isomorphous substitution of trivalent with divalent octahedral cations, for instance, $[Ni_{1-x}^{2+}Fe_x^{3+}(OH)_2]^{x+}$.[2] The charge is compensated by anions, which reside in the interlayer space between the layers. For a 2:1-ratio of divalent and trivalent cations with carbonate interlayer anions, the interlayer space is densely packed with CO_3^{2-}, lying parallel to the layers with smaller voids filled with interlayer water molecules. As is the case with all layered compounds, LDHs exhibit massive planar defects. Adjacent layers are stacked in a random way (turbostraticity), which complicates the structural analysis by X-ray diffraction.[3]

In the course of electrocatalysis, the redox-active octahedral cations in the LDH layers become partially oxidized, rendering the structural protons of the LDH more acidic.[4] It has been suggested that the compensation of the additional positive charges generated by (electro-)oxidation happens via the loss of protons from the structure.[5] Moreover, this might partially trigger the direct coordination of the interlayer anions to the octahedral cations (grafting), leading to a random modulation of the layer spacing. This random interstratification will affect the positions, the full width of half maximum, and the intensities of 00*l* reflections.[6] In such a case, the X-ray beam averages the different real *d*-spacings corresponding to grafted and nongrafted layers, and hence, the observed basal spacing is no longer related to the real structural parameter. Carbonate-grafted LDHs have been experimentally observed in the thermal evolution (from room temperature to 300 °C) of Ni−Co and Ni−Fe LDHs.[7] In addition to carbonates, grafting of other anions to brucite layers after calcination has also been suggested, including sulfate,[8] phosphate,[9] chromate/dichromate,[10,11] metavanadate,[12] and other oxometalate anions. Such grafting phenomena seem to be common during thermal decomposition. Grafted structures were proposed as intermediates in the thermal LDH decomposition based on density functional theory (DFT) calculations;[13] grafting can only occur at high temperature (330 °C) as indicated by both experiment and theory.[14,15] However, grafting has also been observed under relatively mild conditions for acetates and nitrates in "simple" hydroxides.[16,17]

In summary, the impressive flexibility of the brucite-type structure leads to an extensive "family" tree spanning various combinations of substitution types (valence and types of metals, structural O^{2-}, and OH^-, and types of grafted anions, as shown in Scheme 1) comprising both anionic and cationic

Received: June 26, 2019
Revised: September 11, 2019
Published: September 24, 2019

ACS Publications © 2019 American Chemical Society

DOI: 10.1021/acs.jpcc.9b06061
J. Phys. Chem. C 2019, 123, 25157−25165

Downloaded via UNIV BAYREUTH on October 21, 2019 at 08:59:29 (UTC).
See https://pubs.acs.org/sharingguidelines for options on how to legitimately share published articles.

The Journal of Physical Chemistry C Article

layers and encompasses materials applied in various technical fields such as batteries[18] and catalysis.[19,20]

Scheme 1. Overview (Making No Claim of Completeness) of Brucite-Type (Hydr-)Oxides with One or Two Different Types of Metals of Equal or Different Oxidation States[5,21−26]

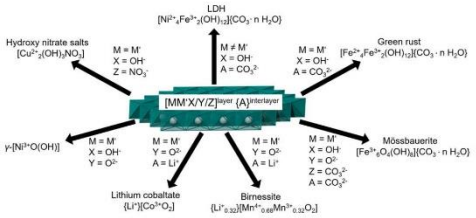

In this paper, a joint computational and experimental effort was taken to determine where mössbauerite is located in this extensive structural family tree and to unambiguously assign its structure.

2. METHODS

2.1. Computational Details. To determine the most stable structures of green rust (GR) and mössbauerite, we employed a two-phase computational strategy. First, 7.5 ps ab initio molecular dynamics (AIMD) simulations were run for all the configurations (surface OH constitution, and grafting states), in order to generate a set of reasonable structures at finite temperature (300 K). An energy convergence criterion of 10^{-7} eV was employed to minimize the energy drift during the simulations. Then, the most stable four structurally inequivalent configurations were selected from the simulation trajectory, and subsequent geometry optimization was performed to locate local minima on the potential energy surface (PES). These structures were then used as starting points for the calculation of minimum energy pathways between relevant minima, via climbing image nudged-elastic band (CI-NEB) calculations. In summary, AIMD is employed as a tool to increase the sampling of configuration space under experimentally realistic conditions, while multiple starting configurations allow all important structures to be accessed, avoiding problems of rare event sampling. All energetic and structural analyses are then performed on the PES on which we search for stationary points at relevant regions.

Spin-polarized DFT calculations were performed using the projector-augmented wave[27] formalism and the generalized gradient approximation method with the Perdew−Burke−Ernzerhof exchange-correlation functional as implemented in the Vienna Ab initio Simulation Package (VASP).[28−30] The DFT-D3 method of Grimme with Becke−Johnson damping was employed to evaluate the dispersion contribution.[31] The plane-wave basis set was expanded to a cutoff energy of 500 eV. Convergence criteria of 10^{-5} eV and 10^{-2} eV/A were used for the energy and forces in geometry optimizations, respectively. The DFT + U approach is applied to treat the electron correlation of highly localized iron d orbitals, with the values of $U-J$ for Fe^{2+}/Fe^{3+} set to 3.7 eV. This value has been proposed previously for iron oxide surfaces.[32] The volume and lattice parameters of unit cells and atomic positions were fully relaxed during geometry optimizations. The transition states were localized using the climbing image nudged elastic band method[33] as implemented in the Transition State Tools for the VASP (VTST) module.[34] The solid-state CI-NEB was used, in which the volumes and lattice parameters of all intermediates were fully relaxed during the transition state search.

Test calculations carried out for mössbauerite with 2T unit cells (two layers per cell) revealed that ferromagnetic (FM) and antiferromagnetic states have very similar energies (the differences are always smaller than 10 kJ mol^{-1} and mostly smaller than 5 kJ mol^{-1}). Thus, FM coupling was adopted for all calculations. Consequently, calculations were performed for a unit cell comprising a single layer. The $3R_1$ model was used for GR, and it was reduced to 1/3 by an offset vector, considering the symmetry. There are a large number of possible structures of mössbauerite, $3T_7$ ($O_1O_2P_2$). Therefore, the 1T model was used; the corresponding O_1 geometry represents reasonably well the structure of mössbauerite, and it is suitable for an atomistic understanding of the interlayer space. The $\sqrt{3} \times 2\sqrt{3}$ supercell was adopted to accommodate the carbonate anion (CO_3^{2-}). Three water molecules were included in the interlayer space within both models, giving the following stoichiometries: GR $[Fe^{II}_4Fe^{III}_2(OH)_{12}]\{CO_3{\cdot}3H_2O\}$ and mössbauerite $[Fe^{III}_6O_4(OH)_8]\{CO_3{\cdot}3H_2O\}$. Thus, the total magnetic moments of GR and mössbauerite were fixed at 26 and 30 μ_B per cell, respectively, (6 Fe atoms in total, 4 Fe^{2+} and 2 Fe^{3+} in GR, and 6 Fe^{3+} in mössbauerite). $4 \times 3 \times 2$ k-point sampling was used in all calculations.

2.2. Refinement of the Disorder Model. TOPAS-Academic V6 was used for the refinement of the real structure and the disorder model.[35] Applying the unit cell data from DFT calculations, a stack of 400 layers was created with stacking probabilities of $p_{grafted} = 0.7$ and $p_{non\text{-}grafted} = 0.3$. To introduce turbostratic disorder in the stack, random shifts in a and b directions were applied between adjacent layers in the stack. To compensate the thermal expansion of the lattice parameters of the DFT-calculated values, the unit cell parameters a and b were refined within a range of 5.5−5.9 and 10.6−11.5 Å, respectively. The c axis for grafted layers was allowed to refine within a range of 7.2−7.3 Å and for nongrafted within 7.5−7.8 Å. Cell angles were allowed to vary within ±3°. Also, the atomic displacement parameters (beq) were fixed to seven for hydrogen, six for carbon, four for iron, and six for oxygen. A step size of 0.05° 2θ was chosen for the refinement.

2.3. Synthesis and Characterization. Carbonate-interlayered GR was synthesized according to a literature procedure. In brief, a 2:1 mixture of ferrous (2.65 g) and ferric chloride (1.75 g) was dissolved in 48 mL Ar-saturated water. This yields a total iron concentration of 0.4 M. Na_2CO_3 solution (40 mL, 1.0 M) in Ar-saturated water was added, which results in the precipitation of a greenish-blue solid. Both solutions were heated to 50 °C before mixing them. Under continuous Ar-flow, the GR suspension was stirred at 50 °C for 30 min. For the synthesis of mössbauerite, 2 mL of an aqueous 30 wt % H_2O_2 solution was added to the GR suspension described above. Assuming that 1 molecule of H_2O_2 can oxidize two ferrous iron atoms, this corresponds to a three-fold excess of the oxidant to Fe^{2+}.

Powder X-ray diffraction patterns of GR and mössbauerite were recorded with a STOE STADI-P equipped with four MYTHEN2 R 1K detectors and Ag Kα (λ = 0.5594075 Å) in 0.5 mm glass capillaries.[36] The mössbauerite diffraction pattern for the refinement was sampled with synchrotron radiation in

DOI: 10.1021/acs.jpcc.9b06061
J. Phys. Chem. C 2019, 123, 25157−25165

The Journal of Physical Chemistry C Article

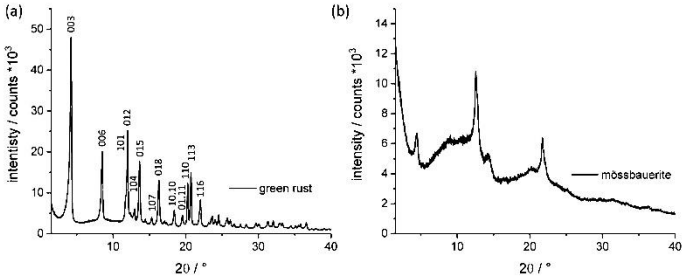

Figure 1. PXRD patterns of (a) carbonate-interlayered GR indexed according to Drissi et al.[38] and the resulting (b) carbonate-interlayered mössbauerite after forced oxidation with H_2O_2.

transmission mode (beamline ID-31 at the ESRF, Grenoble, with an X-ray energy of 70 keV, λ = 0.1771 Å) using a Pilatus X CdTe 2M detector and NIST CeO_2 for distance calibration. The IR spectra of the powder samples were recorded using a JASCO FTIR 6100 spectrometer (400−4000 cm^{-1} range; 4 cm^{-1} resolution).

3. RESULTS AND DISCUSSION

GR $[Fe^{II}_4Fe^{III}_2(OH)_{12}]\{CO_3{\cdot}3H_2O\}$ is a member of the fougèrite group minerals and is unique among LDHs because the divalent and trivalent cations are of the same element (Fe). It is known to be present in the form of naturally occurring GR phases. Some rare natural samples of GR are ordered sufficiently well to determine unequivocally the layer stacking as typically $3R_1$ polytype and to refine the structure.[5,37] GR synthesized in the laboratory is not turbostratically disordered as well, showing strong *hkl* reflections in addition to the 00*l* series (Figure 1a). The basal distance is uniform leading to a so-called rational 00*l*-series. When calculating the basal spacing from individual 00*l* reflections, the coefficient of variation is small, indicating that the basal spacing represents the distance in the real structure.

Recently, mössbauerite $[Fe^{III}_6O_4(OH)_8]\{CO_3{\cdot}3H_2O\}$ synthesized by the chemical oxidation of GR by H_2O_2 has been shown to be a promising all-iron efficient oxygen evolution reaction (OER) catalyst.[39] Unlike most other LDH materials, mössbauerite is found to be a purely semiconducting material with no localized d → d-transitions, as observed in the UV−vis diffuse reflectance spectrum.[39] This photo-electronic property might be related to the catalytic performance. It is, however, unknown which structural feature is related to the important change in the electronic structure. The diffraction pattern of mössbauerite is rather featureless with very few, rather broad, and asymmetrical peaks (Figure 1b). The first peak observed at 7.0 Å has been related to the basal spacing.[5] A 00*l* series is, however, missing. Moreover, this apparent basal spacing is considerably lower than that of the parent GR (7.5 Å)[40] and all other carbonate LDHs.[8] Upon oxidation of GR, the morphology is preserved, suggesting that the transformation is topotactic. The features of the diffraction pattern point toward turbostratic disorder combined with random interstratification of different layer separations. Clearly, structural details would be needed for a knowledge-based optimization of the OER performance, but with these diffraction data in hand, such details are not accessible.

Given this situation, computational studies of both GR and mössbauerite will be of great assistance, and at the same time, they will provide an understanding of the electronic properties. Both nongrafted (for the interlayer carbonate) and grafted layers are considered in this study. Results of the periodic DFT models are critically evaluated in the light of published and newly acquired experimental data. The presented computational and experimental results address the following questions: the structures of nongrafted and grafted GR and mössbauerite, energetics and mechanism of grafting, grafting of mössbauerite driven by hydrogen peroxide, and the stability of bidentate carbonates.

3.1. Green Rust. For geometry optimization, the published structure for GR[41] was modified by saturating all surface oxygen atoms with hydrogens (Figure 2). A $\sqrt{3} \times 2\sqrt{3}$

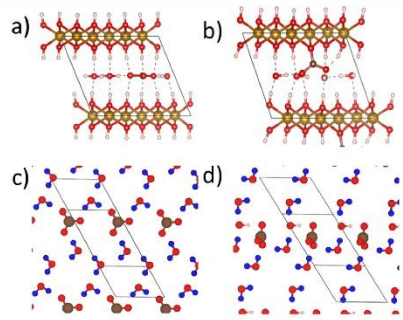

Figure 2. Side and top views of the most stable optimized structures of GR without grafting (GRNG_1) (a,c) and with carbonate grafting (GRG_1) (b,d). Top views show only species in the interlayer gallery. Iron is gold, carbon is brown, oxygen is red, interlayer water hydrogen is blue, and hydrogen on the displaced hydroxyl (d) is white.

supercell of $[Fe^{II}_4Fe^{III}_2(OH)_{12}]\{CO_3{\cdot}3H_2O\}$ was chosen as the model that is consistent with the model of mössbauerite discussed below. Because of the larger number of geometrical and conformational degrees of freedom of molecules in the interlayer space, several low-lying energy minima were obtained via the two-phase—AIMD and local optimization procedure described in Section 2.1. The located low-energy structures are depicted in the Supporting Information (Figure S1). The top and side views of the most stable optimized GR

DOI: 10.1021/acs.jpcc.9b06061
J. Phys. Chem. C 2019, 123, 25157−25165

The Journal of Physical Chemistry C Article

structures for nongrafted (GRNG_1, Figure 2a,c) and grafted (GRG_1, Figure 2b,d) are given in Figure 2. In GRNG_1, the carbonate anion lies parallel to the layers, and it is surrounded by water molecules, which form a two-dimensional hydrogen-bonding network. In GRG_1, the carbonate ion substitutes an OH^- group upon grafting and lies perpendicular to the layer. The replaced hydroxyl group lies in the interlayer space (Figure 2d) and interacts with the interlayer water molecules and a hydrogen atom in the lower layer. The relative energies (with respect to the most stable configuration obtained) and the unit cell parameters of the five lowest energy structures are summarized in Table 1. We found that the grafted structures are higher in energy than the corresponding nongrafted structures. This indicates that grafting for GR is unlikely to take place spontaneously (Table 1). In addition, grafting leads to a sizable decrease of the lattice parameter c, while the a parameter is not changed significantly.

Table 1. Relative Energies (E_{rel}, in kJ mol^{-1}) and a and c^* (d_{001}) Parameters (in Å) of Optimized GR Structures

nongrafted			grafted		
structure	E_{rel}	a/c^*	structure	E_{rel}	a/c^*
GRNG_1	0	3.20/7.43	GRG_1	19	3.21/7.19
GRNG_2	1	3.20/7.43	GRG_2	20	3.21/7.11
GRNG_3	1	3.20/7.44	GRG_3	28	3.20/7.12
GRNG_4	2	3.20/7.42	GRG_4	48	3.20/7.14
GRNG_5	3	3.20/7.43	GRG_5	54	3.23/7.19

3.2. Mössbauerite. The starting model for mössbauerite $[Fe_6^{III}O_4(OH)_8]\{CO_3{\cdot}3H_2O\}$ was derived from the optimized GR structure. The presence of four surface O^{2-} (per UC) introduces additional complexity of the interlayer space (compared to GR) because various OH distributions must be considered: (i) ($6OH^-/2OH^-$) with the fully protonated top surface and only two OH^- groups on the bottom surface, (ii) ($5OH^-/3OH^-$) with five and three OH^- groups on the top and bottom surfaces, respectively, and (iii) ($4OH^-/4OH^-$) with an equal number of OH^- groups on both surfaces. For each of these top/bottom distributions, different lateral distribution patterns exist. In addition, protons can also be exchanged with carbonate (HCO_3^-) and water (H_3O^+) in the interlayer space. This range of configurations was captured by the combination of AIMD and local geometry optimization. For the proton exchange between the surface and the interlayer, multiple transitions were found to occur within the duration of the simulation, implying low barriers. Grafting/ungrafting events and the transfer of protons between lateral positions was not observed, as these constitute rare events. Hence, each such configuration was generated and simulated with AIMD to ensure all important configurations were considered.

The scatter in energy among the various nongrafted configurations of mössbauerite is as large as 89 kJ mol^{-1} (MNG_8), which emphasizes the crucial influence of the distribution of protons within the structure (Table 2). The four lowest energy structures for each of three OH distributions are shown in Figure S2. Among these, the most stable ($5OH^-/3OH^-$)-MNG_1 configuration is found to be 37 kJ mol^{-1} and 32 kJ mol^{-1} more stable than the most stable ($6OH^-/2OH^-$)-MNG_5 and ($4OH^-/4OH^-$)-MNG_9 configurations, respectively. Based on these results, the energy hypersurface of grafted structures for mössbauerite was explored for the ($5OH^-/3OH^-$) distribution, and the results for the four lowest energy grafted structures (MG_1 to MG_4) are reported in Table 2 (the corresponding structures are shown in Figure S3). While the energy difference between grafted and nongrafted structures is slightly lower for mössbauerite than that for GR; nevertheless, the higher energies of grafted structures suggest that the carbonate grafting cannot proceed spontaneously.

Figure 3 shows the most stable nongrafted ($5OH^-/3OH^-$)-MNG_1 and grafted ($5OH^-/2OH^-$)-MG_1 structures of mössbauerite (see Supporting Information for cif files S5 and S6). It is interesting to note that the lower symmetry of the hydrogen distribution between layers leads to a lower symmetry interlayer water network, with water molecules rotated away from the perfect planarity as observed in fougerite. In the grafted mössbauerite structure (Figure 3b,d), the CO_3^{2-} grafted on the bottom of the trioctahedral sheet surface is protonated to a bicarbonate by the proton formerly residing on the adjacent trioctahedral sheet, and

Table 2. Relative Energies (E_{rel}, in kJ mol^{-1}) and a and c^* (d_{001}) Parameters (in Å) of Mössbauerite Layers with Different Numbers of Hydroxide Groups on Upper and Lower Surfaces of Trioctahedral Sheets

nongrafted minima			grafted minima		
Structure	E_{rel}	a/c^*	structure	E_{rel}	a/c^*
($5OH^-/3OH^-$)			($5OH^-/2OH^-$)		
MNG_1	0	3.14/7.17	MG_1	16	3.15/6.90
MNG_2	17	3.15/7.11	MG_2	17	3.15/6.85
MNG_3	29	3.12/7.03	MG_3	27	3.13/6.84
MNG_4	45	3.09/7.08	MG_4	27	3.15/6.83
($6OH^-/2OH^-$)					
MNG_5	37	3.08/7.16			
MNG_6	40	3.09/7.11			
MNG_7	48	3.07/7.17			
MNG_8	89	3.06/7.21			
($4OH^-/4OH^-$)					
MNG_9	32	3.09/6.98			
MNG_10	33	3.08/7.03			
MNG_11	57	3.06/7.03			
MNG_12	63	3.12/7.28			

DOI: 10.1021/acs.jpcc.9b06061
J. Phys. Chem. C 2019, 123, 25157−25165

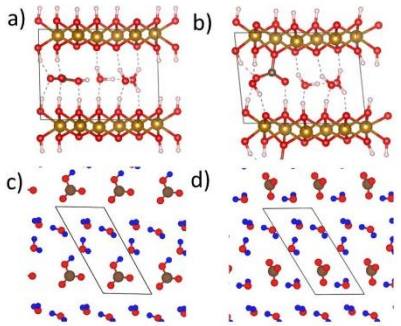

Figure 3. Side and top views of optimized mössbauerite structure without grafting ($5OH^-/3OH^-$)-MNG_1 (a,c) and with grafting ($5OH^-/2OH^-$)-MG_1 of the carbonate (b,d). Top views show only species in the interlayer gallery. Iron is gold, carbon is brown, oxygen is red, and interlayer water hydrogen is blue.

therefore, this structure is no longer denoted as ($5OH^-/3OH^-$) but as ($5OH^-/2OH^-$). Similar to GR, the c^* parameter of the grafted mössbauerite is found to be significantly smaller than that of the nongrafted structure, while the a value remains unchanged. While the basal spacing (d_{001}) obtained for the optimized nongrafted structure of mössbauerite (7.17 Å) is longer than the experimental value of 7.0 Å, the basal spacing obtained for the grafted structure (6.90 Å) is shorter. These results indicate that the experimental sample could be a mixture of grafted and nongrafted surfaces.

3.3. Monodentate Versus Bidentate Carbonates. According to previous theoretical studies of the thermal decomposition of the Mg–Al LDH, the energy barrier for interconversion between monodentate and bidentate carbonate grafted structures is as high as 175 kJ mol^{-1}, and the reaction energy is above 150 kJ mol^{-1}.[13] Both the high barrier and reaction energy values render this process unlikely to proceed under mild conditions, and hence, the phase-change in the Mg–Al LDH appears between 180 and 200 °C.

In the case of mössbauerite, the reaction energy for the transformation of the monodentate to the bidentate structure (Figure 4) is 149 kJ mol^{-1}. Such a high reaction energy inhibits this reaction under the experimental conditions (up to ~50 °C) and agrees well with previous theoretical work.[13] Hence, bidentate carbonate grafting is much less likely than monodentate grafting, and only a monodentate grafting is discussed in the following sections.

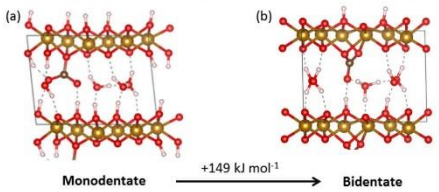

Figure 4. Interlayer structures of (a) monodentate ($5OH^-/2OH^-$)-MG_1 and (b) bidentate carbonate-grafted mössbauerite. a and c^* of the bidentate structure are 5.42 and 6.95 Å, respectively.

3.4. Mechanism of Carbonate Grafting. In order to determine the kinetic feasibility of the grafting process, we have calculated the energy profiles for grafting. These are shown in Figure 5a,b for GR (from GRNG_1 to GRG_1) and mössbauerite (from ($5OH^-/3OH^-$)-MNG_1 to ($5OH^-/2OH^-$)-MG_1), respectively. The energies of the reactants, transition states, and products are depicted in Figure 5a,b. The structures of stationary points are shown in Figure 5c.

We first describe the mechanism of grafting for GR. The transition-state structure (**2** in Figure 5a) is reached when the carbonate anion abstracts a hydrogen ion from the trioctahedral sheet and forms a HCO_3^- anion. The grafted carbonate is formed along with the hydroxyl group (OH^-) in the interlayer space (**3** in Figure 5a). The barrier for this transformation from GRNG_1 to GRG_1 in GR is as high as 190 kJ mol^{-1}, and the whole processes is endothermic by 19 kJ mol^{-1}, which suggests that grafting process in GR is both thermodynamically and kinetically unfavorable, and thus, unlikely to occur under the experimental conditions (up to ~50 °C).

The grafting reaction path from nongrafted ($5OH^-/3OH^-$)-MNG_1 to the grafted ($5OH^-/2OH^-$)-MG_1 structure is quite different in the case of mössbauerite (Figure 5b). As mentioned above, the carbonate anion (CO_3^{2-}) exists in a protonated form, as HCO_3^-. From the most stable nongrafted mössbauerite structure (**1′** in Figure 5b), the OH group on HCO_3^- rotates via transition state **2′** to the local minimum **3′** at +20 kJ/mol. The whole carbonate molecule undergoes a rotation about the plane parallel to the layers, to align the OH group with a surface hydrogen, leading to the intermediate product **5′**, which is 20 kJ/mol higher in energy than the initial state. The formed OH^- group subsequently attacks a surface H^+, leading to the transition state **6′**. The intermediate product formed is the grafted carbonate and one H_2O molecule (**7′** in Figure 5b). A range of energetically facile rotations of the formed water molecule are possible. One such pathway moves through the low energy transition state **8′** to form the final product **9′**. The overall barrier for the entire process is 94 kJ mol^{-1}, which while being significantly lower than that in GR, is still too high for the reaction to take place under the experimental conditions. Although this reaction is also slightly less endothermic (17 kJ mol^{-1}) than that of GR (19 kJ mol^{-1}), there is still no clear driving force for the formation of carbonate-grafted mössbauerite.

3.5. Effect of H_2O_2. H_2O_2 is used for the oxidation of all Fe^{2+} in GR to Fe^{3+} and to transform GR to mössbauerite. In doing so, four H_2O molecules are formed from two H_2O_2

$$[Fe_4^{II}Fe_2^{III}(OH)_{12}]\{CO_3\cdot nH_2O\}(\text{green rust}) + 2H_2O_2 \rightarrow [Fe_6^{III}O_4(OH)_8]\{CO_3\cdot nH_2O\}(\text{mössbauerite}) + 4H_2O \quad (1)$$

It is difficult to explore the entire reaction paths from GR to mössbauerite; however, the calculation of the reaction energy is straightforward (Figure 6). Assuming the stoichiometry of the above proposed process, the reaction proceeds exothermally with a reaction energy of −154 kJ mol^{-1}, which is likely to be the driving force for carbonate grafting in mössbauerite. In the absence of H_2O_2, there is no kinetic nor thermodynamic driving force for the grafting reaction in GR or mössbauerite. However, in the transformation of ungrafted GR to grafted mössbauerite, there is sufficient energy to overcome the

DOI: 10.1021/acs.jpcc.9b06061
J. Phys. Chem. C 2019, 123, 25157−25165

The Journal of Physical Chemistry C Article

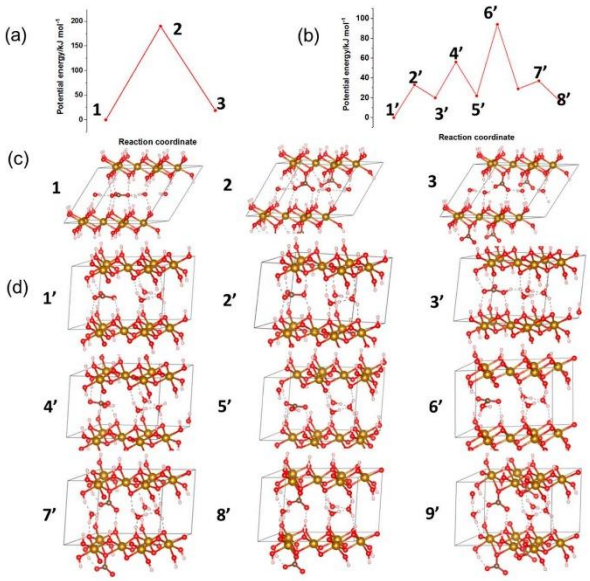

Figure 5. Potential energy profiles of the carbonate grafting process for (a) GR from GRNG_1 to GRG_1 and (b) mössbauerite from ($5OH^-$/$3OH^-$)-MNG_1 to ($5OH^-$/$2OH^-$)-MG_1. Structures for the transitions of GR (c) and mössbauerite (d).

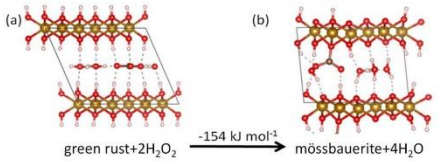

Figure 6. Transformation of (a) GR (GRNG_1) to (b) carbonate-grafted mössbauerite [($5OH^-$/$2OH^-$)-MG_1].

moderate energetic penalty of grafting, despite the overall preference of ungrafted mössbauerite. It is valuable to note that if the grafting (driven by H_2O_2) takes place, the resulting structure is protected by relatively high barriers against returning to nongrafted structures (Figure 5). Hence, it is reasonable to assume that once the grafted surface is obtained, it is kinetically stable, despite being energetically metastable.

3.6. Refining the Real Structure and the Disordered Model of Mössbauerite. By comparing the experimentally observed diffraction pattern (Figure 1b) with the diffraction patterns calculated for the various 3-dimensionally ordered computationally optimized mössbauerite structures (Figure S4), it becomes obvious that real mössbauerite is crystallographically heavily disordered and lacks 3-dimensional translational symmetry. Based on the computational results, it appears likely that mössbauerite suffers from both a turbostratic stacking disorder and a statistical interstratification of nongrafted and grafted trioctahedral sheets with randomly varying separation of the adjacent layers ($d_{grafted}$ = 6.90 Å; $d_{non\text{-}grafted}$ = 7.17 Å). TOPASS offers a routine based on the DIFFaX code by M. M. J. Tracey that allows refinement of such non-Bragg diffuse scattering patterns. Given the poor ratio of allowed variables to observables, the precision of such a refinement is of course far worse than can be expected for an ordinary Rietveld refinement. Nevertheless, a valuable insight into the disorder model that is effective for mössbauerite can be obtained. If the refinement confirms the coexistence of nongrafted and grafted trioctahedral sheets, it would even support the computational findings. For reasons of a better signal to the background ratio, synchrotron data have been used for the refinement of the mössbauerite structure.

Applying the computational geometry optimized structures for nongrafted and grafted mössbauerites [($5OH^-$/$3OH^-$)-MNG_1 and ($5OH^-$/$2OH^-$)-MG_1 in Table 2 and cif files in S5 and S6], a supercell was created using Materials Studio in order to obtain symmetry-related coordinates with average cell parameters. For the refinement, this supercell was converted back to sheets of grafted and nongrafted mössbauerite layers. A random stack of 400 trioctahedral sheets with either grafted or nongrafted carbonate was created with stacking probabilities of $p_{grafted}$ = 0.7 and $p_{non\text{-}grafted}$ = 0.3. This value was chosen to match the position of the 001 peak and was found not to vary during refinement. To introduce turbostratic disorder in the stack, random shifts in *a* and *b* directions were applied between adjacent trioctahedral sheets in the stack. The refinement of the experimental diffraction traces of mössbauerite (Figure 7) yielded a reasonable R_{wp} of 5.9 for such a heavily disordered structure. The refined cell parameters remain close to the starting values (Table 3). The deviation from the DFT calculated values results mainly from the fact that DFT calculations do not consider thermal expansion or thermally induced flexibility of the lattice.

DOI: 10.1021/acs.jpcc.9b06061
J. Phys. Chem. C 2019, 123, 25157−25165

The Journal of Physical Chemistry C Article

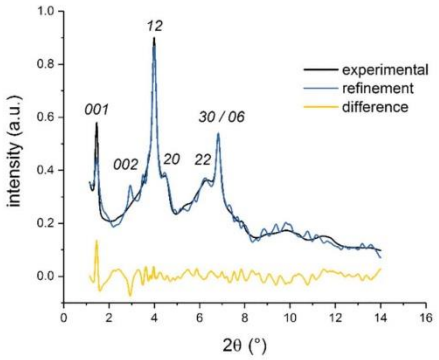

Figure 7. Fit to Rietveld-generated pattern comprises stacks of grafted and nongrafted mössbauerite with a stacking probability of 0.7 for grafted and 0.3 for nongrafted layers.

Table 3. Refined Cell Parameters along with DFT Calculated Distances (Å) and Angles (deg)

cell parameter	DFT-grafted	DFT-nongrafted	refinement
A	5.450(6)	5.446(4)	5.525(8)
B	10.863(5)	10.872(4)	10.733(2)
C	7.156(9)	7.227	7.203(2)/7.800
α	87.78(9)	86.59(5)	87.32(3)
β	104.23(8)	102.81(9)	108.16(9)
γ	120.62(9)	120.45(9)	123.26(7)

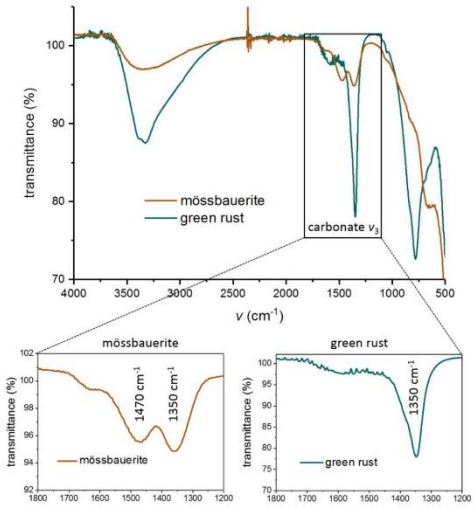

Figure 8. FTIR spectra of GR and mössbauerite. The inset shows the regional characteristic for the carbonate. The splitting of the ν_3 band with an energy difference of ~120 cm^{-1} indicates the monodentate carbonate in mössbauerite, whereas the ν_3 absorption band in the IR spectrum of GR shows a little to no splitting indicating no grafted carbonate.

The calculated pattern takes the turbostratic disorder into account by shifting the stacks in a and b directions by $\Delta \neq 1/3$. This results in a broadening of the $hk0$ Bragg reflections into asymmetric, λ-shaped hk-bands. The first prominent reflection at $2\theta = 1.45°$ corresponds to the averaged trioctahedral sheet separation 7.0 Å, which, however, is not found in the real structure. The difference plot suggests that the interstratification cannot be mimicked perfectly by using random sequences of just two types of trioctahedral sheet separations. A potential explanation is that within a single layer domain of the interstratified phase, both grafted and nongrafted regions are found with smooth transitions between their different thicknesses. Additionally, the second peak centered at $2\theta = 3.99°$ cannot be indexed unequivocally because of the number of superimposed reflections from both grafted and nongrafted structural motifs. The most intense reflections in this region can be assigned to the $hk = 12$ band according to the refinement. The reflex centered at $2\theta = 6.83°$ can be assigned mainly to $hk = 30$ and $hk = 06$ bands. In summary, the refinement of the disorder model strongly supports the computational results, which suggests that for mössbauerite, a grafted structure is energetically feasible, and it indeed coexists in a randomly interstratified manner with nongrafted layers.

Further experimental evidence for the grafting of interlayer carbonate anions to the trioctahedral sheet comes from a comparison of IR spectra (Figure 8) of GR and mössbauerite. Usually, three frequency domains are considered in the IR spectrum of a typical LDH: (i) 400−800 cm^{-1} for lattice vibrations, (ii) 800−1500 cm^{-1} for vibrations of adsorbed or intercalated species, and (iii) the third region up to 4000 cm^{-1} for characteristic adsorbed or structural water molecules.

The insets are zoomed-in images of the spectral region that is characteristic for the carbonate. Mössbauerite shows three absorption bands, while GR shows only two bands in this region. The absorption maximum at 1630 cm^{-1} in both spectra can be assigned to structural water. The remaining absorption maxima originate from the ν_3 band of the carbonate. A single ν_3 band at 1350 cm^{-1} in the spectrum of GR indicates the presence of the nongrafted carbonate. The ν_3 band splits into two distinct bands at 1350 and 1470 cm^{-1} in mössbauerite. The splitting by 120 cm^{-1} seen in the spectrum of mössbauerite indicates the lowering of carbonate symmetry from D_{3h} to C_{2v} due to formation of monodentate rather than that of bidentate carbonate species (grafting),[7] in agreement with the calculations in Section 3.3. This, however, does not exclude the presence of the nongrafted carbonate as suggested by the refinement.

4. CONCLUSIONS

The results of the first systematic, combined computational and experimental investigations of GR (GR) and mössbauerite LDHs are presented. DFT models in combination with periodic models of iron-containing LDHs allow us to identify various structural details at the atomistic level. A critical synopsis of these computational results with experimental data leads us to the following conclusions:

(1) The calculated relative energies of grafted and nongrafted structures of GR and mössbauerite suggest that carbonate grafting is unlikely in both phases.

DOI: 10.1021/acs.jpcc.9b06061
J. Phys. Chem. C 2019, 123, 25157−25165

(2) The carbonate grafting process in GR is endothermic (19 kJ mol^{-1}), and it exhibits a high barrier (190 kJ mol^{-1}).
(3) The carbonate grafting process in mössbauerite is also endothermic (16 kJ mol^{-1}), and the corresponding barrier is 94 kJ mol^{-1}.
(4) Considering the involvement of H_2O_2, which is utilized experimentally for the GR to mössbauerite conversion, the grafting along with iron oxidation becomes strongly exothermic (−154 kJ mol^{-1}). This is proposed to be the driving force for carbonate grafting in mössbauerite. Grafting is also supported by the features of the carbonate band in the IR spectrum.
(5) Grafting leads to the formation of monodentate carbonates, while the formation of bidentate carbonates is unlikely.
(6) The computational findings allow for the establishment of a disordered model which, in addition to turbostratic stacking, includes random interstratification. This model provides a satisfactory fit for the observed diffraction pattern.

■ ASSOCIATED CONTENT

Supporting Information

The Supporting Information is available free of charge on the ACS Publications website at DOI: 10.1021/acs.jpcc.9b06061.

Side views of optimized structures of GR, side views of optimized structures of nongrafted mössbauerite, side views of optimized structures of grafted mössbauerite, simulated PXRD patterns of grafted and nongrafted mössbauerite, cif file of nongrafted mössbauerite from computation, cif file of grafted mössbauerite from computation (PDF)

■ AUTHOR INFORMATION

Corresponding Authors

*E-mail: josef.breu@uni-bayreuth.de (J.B.).
*E-mail: petr.nachtigall@natur.cuni.cz (P.N.).

ORCID

Pengbo Lyu: 0000-0002-1785-9861
Lukáš Grajciar: 0000-0001-9464-7769
Josef Breu: 0000-0002-2547-3950
Petr Nachtigall: 0000-0002-1628-7275

Author Contributions

[§]P.L. and M.E. contributed equally.

Notes

The authors declare no competing financial interest.

■ ACKNOWLEDGMENTS

We acknowledge the financial support from the Bavarian-Czech Academic Agency (Bayerisch-Tschechische Hochschulagentur) for the framework of the project "Entwicklung und Designprinzipien für strukturierte Materialien" financed by funds of the Free State of Bavaria. Work in Prague was also supported by the "CHARLES UNIVERSITY CENTRE OF ADVANCED MATERIALS: DESIGN, SYNTHESIS, AND APPLICATIONS", OP VVV "Excellent Research Teams", project no. CZ.02.1.01/0.0/0.0/15_003/0000417, and Charles University Research Centre program no. UNCE/SCI/014. Computational resources were partially provided by the CESNET LM2015042 and the CERIT Scientific Cloud LM2015085, provided under the programme "Projects of Large Research, Development, and Innovation Infrastructures". J.B. is grateful to the Deutsche Forschungsgemeinschaft (DFG) in the framework of SFB 840. M.E. thanks the Hanns Seidel foundation for a doctoral scholarship and Sebastian Mangelsen from the Institut für Anorganische Chemie of the Christian-Albrechts-Universität zu Kiel for his help with the refinement in TOPAS. Beamtime at the European Synchrotron Radiation Facility (ESRF, ID31) is gratefully acknowledged.

■ REFERENCES

(1) Gong, M.; Li, Y.; Wang, H.; Liang, Y.; Wu, J. Z.; Zhou, J.; Wang, J.; Regier, T.; Wei, F.; Dai, H. An Advanced Ni−Fe Layered Double Hydroxide Electrocatalyst for Water Oxidation. *J. Am. Chem. Soc.* **2013**, *135*, 8452−8455.
(2) Wang, Q.; O'Hare, D. Recent Advances in the Synthesis and Application of Layered Double Hydroxide (LDH) Nanosheets. *Chem. Rev.* **2012**, *112*, 4124−4155.
(3) Ramesh, T. N.; Jayashree, R. S.; Kamath, P. V. Disorder in Layered Hydroxides: Diffax Simulation of the X-Ray Powder Diffraction Patterns of Nickel Hydroxide. *Clays Clay Miner.* **2003**, *51*, 570−576.
(4) Chen, J. Y. C.; Dang, L.; Liang, H.; Bi, W.; Gerken, J. B.; Jin, S.; Alp, E. E.; Stahl, S. S. Operando Analysis of Nife and Fe Oxyhydroxide Electrocatalysts for Water Oxidation: Detection of Fe^{4+} by Mössbauer Spectroscopy. *J. Am. Chem. Soc.* **2015**, *137*, 15090−15093.
(5) Génin, J.-M. R.; Mills, S. J.; Christy, A. G.; Guérin, O.; Herbillon, A. J.; Kuzmann, E.; Ona-Nguema, G.; Ruby, C.; Upadhyay, C. Mössbauerite, $Fe_6^{3+}O_4(OH)_8[CO_3]\cdot 3H_2O$, the fully oxidized 'green rust' mineral from Mont Saint-Michel Bay, France. *Mineral. Mag.* **2014**, *78*, 447−465.
(6) Reynolds, R. C.; Hower, J. F. The Nature of Interlayering in Mixed-Layer Illite-Montmorillonites. *Clays Clay Miner.* **1970**, *18*, 25−36.
(7) Vaysse, C.; Guerlou-Demourgues, L.; Delmas, C. Thermal Evolution of Carbonate Pillared Layered Hydroxides with (Ni, L) (L = Fe, Co) Based Slabs: Grafting or Nongrafting of Carbonate Anions? *Inorg. Chem.* **2002**, *41*, 6905−6913.
(8) Constantino, V. R. L.; Pinnavaia, T. J. Basic Properties of $Mg^{2+}_{1-x}Al^{3+}_x$ Layered Double Hydroxides Intercalated by Carbonate, Hydroxide, Chloride, and Sulfate Anions. *Inorg. Chem.* **1995**, *34*, 883−892.
(9) Shimamura, A.; Kanezaki, E.; Jones, M. I.; Metson, J. B. Direct Observation of Grafting Interlayer Phosphate in Mg/Al Layered Double Hydroxides. *J. Solid State Chem.* **2012**, *186*, 116−123.
(10) Bigey, L.; Depège, C.; de Roy, A.; Besse, J. EXAFS and XANES Study of Layered Double Hydroxides. *J. Phys. IV* **1997**, *7*, 949−950.
(11) Malherbe, F.; Bigey, L.; Forano, C.; de Roy, A.; Besse, J.-P. Structural Aspects and Thermal Properties of Takovite-Like Layered Double Hydroxides Pillared with Chromium Oxo-Anions. *J. Chem. Soc., Dalton Trans.* **1999**, 3831−3839.
(12) Han, K.; Guerlou-Demourgues, L.; Delmas, C. A New Metavanadate Inserted Layered Double Hydroxide Prepared by 'Chimie Douce'. *Solid State Ionics* **1996**, *84*, 227−238.
(13) Costa, D. G.; Rocha, A. B.; Souza, W. F.; Chiaro, S. S. X.; Leitão, A. A. Ab Initio Study of Reaction Pathways Related to Initial Steps of Thermal Decomposition of the Layered Double Hydroxide Compounds. *J. Phys. Chem. C* **2012**, *116*, 13679−13687.
(14) Meng, Q.; Yan, H. Theoretical Study on the Topotactic Transformation and Memory Effect of M (II) M (III)-Layered Double Hydroxides. *Mol. Simul.* **2017**, *43*, 1338−1347.
(15) Zhang, S.-T.; Dou, Y.; Zhou, J.; Pu, M.; Yan, H.; Wei, M.; Evans, D. G.; Duan, X. Dft-Based Simulation and Experimental Validation of the Topotactic Transformation of Mgal Layered Double Hydroxides. *ChemPhysChem* **2016**, *17*, 2754−2766.
(16) Laget, V.; Hornick, C.; Rabu, P.; Drillon, M. Hybrid Organic-Inorganic Layered Compounds Prepared by Anion Exchange

DOI: 10.1021/acs.jpcc.9b06061
J. Phys. Chem. C 2019, 123, 25157−25165

Reaction: Correlation between Structure and Magnetic Properties. *J. Mater. Chem.* **1999**, *9*, 169−174.
(17) Yamanaka, S.; Sako, T.; Seki, K.; Hattori, M. Anion Exchange Reactions in Layered Basic Copper Salts. *Solid State Ionics* **1992**, *53−56*, 527−533.
(18) Hall, D. S.; Lockwood, D. J.; Bock, C.; MacDougall, B. R. Nickel Hydroxides and Related Materials: A Review of Their Structures, Synthesis and Properties. *Proc. R. Soc. A* **2015**, *471*, 20140792.
(19) Gong, M.; Dai, H. A Mini Review of Nife-Based Materials as Highly Active Oxygen Evolution Reaction Electrocatalysts. *Nano Res.* **2015**, *8*, 23−39.
(20) Fan, G.; Li, F.; Evans, D. G.; Duan, X. Catalytic Applications of Layered Double Hydroxides: Recent Advances and Perspectives. *Chem. Soc. Rev.* **2014**, *43*, 7040−7066.
(21) Génin, J.-M. R.; Aïssa, R.; Géhin, A.; Abdelmoula, M.; Benali, O.; Ernstsen, V.; Ona-Nguema, G.; Upadhyay, C.; Ruby, C. Fougerite and FeII-III hydroxycarbonate green rust; ordering, deprotonation and/or cation substitution; structure of hydrotalcite-like compounds and mythic ferrosic hydroxide. *Solid State Sci.* **2005**, *7*, 545−572.
(22) Julien, C.; Massot, M.; Baddour-Hadjean, R.; Franger, S.; Bach, S.; Pereira-Ramos, J. P. Raman Spectra of Birnessite Manganese Dioxides. *Solid State Ionics* **2003**, *159*, 345−356.
(23) Singh, D. Characteristics and Effects of γ-NiOOH on Cell Performance and a Method to Quantify It in Nickel Electrodes. *J. Electrochem. Soc.* **1998**, *145*, 116−120.
(24) Newman, S. P.; Jones, W. Comparative Study of Some Layered Hydroxide Salts Containing Exchangeable Interlayer Anions. *J. Solid State Chem.* **1999**, *148*, 26−40.
(25) Wang, B.; Bates, J. B.; Hart, F. X.; Sales, B. C.; Zuhr, R. A.; Robertson, J. D. Characterization of Thin-Film Rechargeable Lithium Batteries with Lithium Cobalt Oxide Cathodes. *J. Electrochem. Soc.* **1996**, *143*, 3203−3213.
(26) Dionigi, F.; Strasser, P. NiFe-Based (Oxy)Hydroxide Catalysts for Oxygen Evolution Reaction in Non-Acidic Electrolytes. *Adv. Energy Mater.* **2016**, *6*, 1600621.
(27) Perdew, J. P.; Burke, K.; Ernzerhof, M. Generalized Gradient Approximation Made Simple. *Phys. Rev. Lett.* **1996**, *77*, 3865−3868.
(28) Blöchl, P. E. Projector Augmented-Wave Method. *Phys. Rev. B: Condens. Matter Mater. Phys.* **1994**, *50*, 17953−17979.
(29) Kresse, G.; Joubert, D. From Ultrasoft Pseudopotentials to the Projector Augmented-Wave Method. *Phys. Rev. B: Condens. Matter Mater. Phys.* **1999**, *59*, 1758−1775.
(30) Kresse, G.; Furthmüller, J. Efficiency of Ab-Initio Total Energy Calculations for Metals and Semiconductors Using a Plane-Wave Basis Set. *Comput. Mater. Sci.* **1996**, *6*, 15−50.
(31) Grimme, S.; Antony, J.; Ehrlich, S.; Krieg, H. A Consistent and Accurate Ab Initio Parametrization of Density Functional Dispersion Correction (DFT-D) for the 94 Elements H-Pu. *J. Chem. Phys.* **2010**, *132*, 154104.
(32) Santos-Carballal, D.; Roldan, A.; Grau-Crespo, R.; de Leeuw, N. H. A DFT Study of the Structures, Stabilities and Redox Behaviour of the Major Surfaces of Magnetite Fe_3O_4. *Phys. Chem. Chem. Phys.* **2014**, *16*, 21082−21097.
(33) Henkelman, G.; Uberuaga, B. P.; Jónsson, H. A Climbing Image Nudged Elastic Band Method for Finding Saddle Points and Minimum Energy Paths. *J. Chem. Phys.* **2000**, *113*, 9901−9904.
(34) Henkelman, G. Vasp TST Tools. http://theory.cm.utexas.edu/vtsttools/ (accessed Feb 9, 2006).
(35) Coelho, A. A. Topas and Topas-Academic: An Optimization Program Integrating Computer Algebra and Crystallographic Objects Written in C++. *J. Appl. Crystallogr.* **2018**, *51*, 210−218.
(36) Thomae, S. L. J.; Prinz, N.; Hartmann, T.; Teck, M.; Correll, S.; Zobel, M. Pushing Data Quality for Laboratory Pair Distribution Function Experiments. *Rev. Sci. Instrum.* **2019**, *90*, 043905.
(37) Bookin, A. S.; Drits, V. A. Polytype Diversity of the Hydrotalcite-Like Minerals. I. Possible Polytypes and Their Diffraction Features. *Clays Clay Miner.* **1993**, *41*, 551−557.
(38) Drissi, S. H.; Refait, P.; Abdelmoula, M.; Génin, J. M. R. The Preparation and Thermodynamic Properties of Fe(II)-Fe(III) Hydroxide-Carbonate (Green Rust 1); Pourbaix Diagram of Iron in Carbonate-Containing Aqueous Media. *Corros. Sci.* **1995**, *37*, 2025−2041.
(39) Ertl, M.; Andronescu, C.; Moir, J.; Zobel, M.; Wagner, F. E.; Barwe, S.; Ozin, G.; Schuhmann, W.; Breu, J. Oxygen Evolution Catalysis with Mössbauerite—a Trivalent Iron-Only Layered Double Hydroxide. *Chem.—Eur. J.* **2018**, *24*, 9004−9008.
(40) Génin, J.-M. R.; Christy, A.; Kuzmann, E.; Mills, S.; Ruby, C. Structure and Occurrences of ≪ Green Rust ≫ Related New Minerals of the ≪ Fougérite ≫ Group, Trébeurdenite and Mössbauerite, Belonging to the ≪ Hydrotalcite ≫ Supergroup; How Mössbauer Spectroscopy Helps XRD. *Hyperfine Interact.* **2014**, *226*, 459−482.
(41) Trolard, F.; Bourrié, G.; Abdelmoula, M.; Refait, P.; Feder, F. Fougerite, a New Mineral of the Pyroaurite-Iowaite Group: Description and Crystal Structure. *Clays Clay Miner.* **2007**, *55*, 323−334.

DOI: 10.1021/acs.jpcc.9b06061
J. Phys. Chem. C 2019, 123, 25157−25165

6.3.1. Supporting Information

Electronic Supplementary Information for:

Structure Determination of the Oxygen Evolution Catalyst Mössbauerite

Pengbo Lyu [a,c], Michael Ertl [b,c], Christopher J. Heard [a], Lukáš Grajciar [a], A.V. Radha [b], Thomas Martin [b], Josef Breu [b*], Petr Nachtigall [a*]

[a] Department of Physical and Macromolecular Chemistry, Faculty of Sciences, Charles University, Hlavova 8, 128 43 Prague 2, Czech Republic

[b] Bavarian Polymer Institute and Department of Chemistry, University of Bayreuth, Bayreuth, Universitätsstraße 30, D-95440, Germany

[c] These two authors contributed equally.

Emails: josef.breu@uni-bayreuth.de petr.nachtigall@natur.cuni.cz

S1

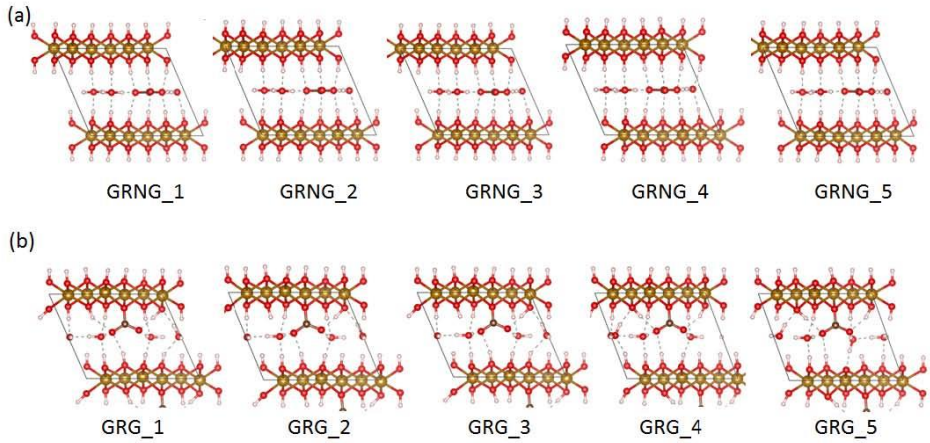

Figure S1: The side views of optimized lowest energy structures for green rust with carbonate (a) non-grafted (GRNG_1 to GRNG_5) and (b) grafted (GRG_1 to GRG_5).

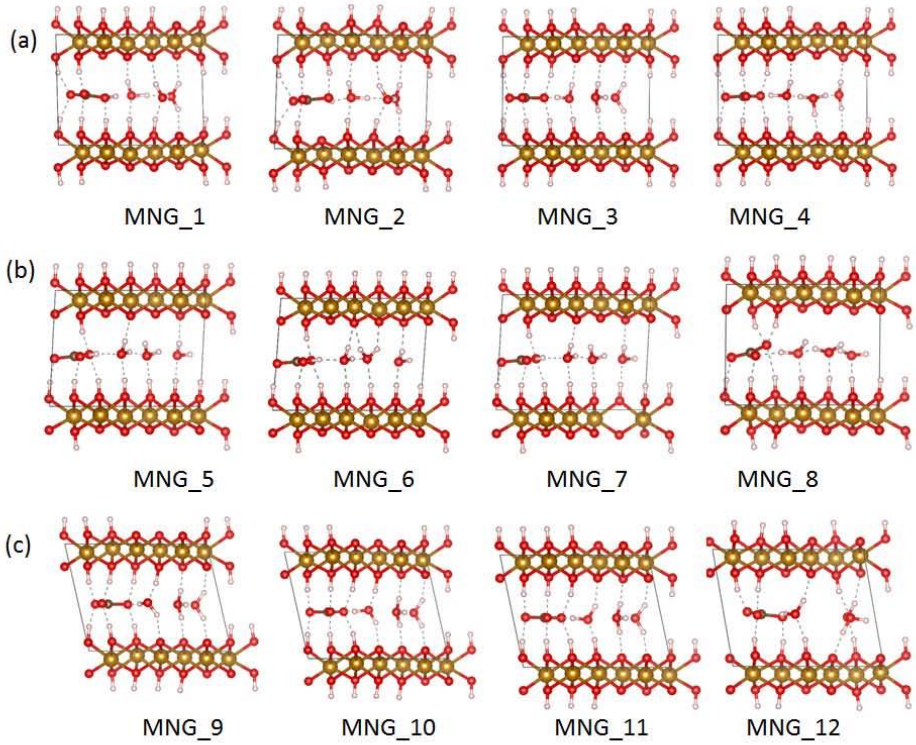

Figure S2: The side views of optimized lowest energy structures for mössbauerite with carbonate non-grafted for (a) ($5OH^-/3OH^-$) configuration from MNG_1 to MNG_4, (b) ($6OH^-/2OH^-$) configuration from MNG_5 to MNG_8, and (c) ($4OH^-/4OH^-$) configuration from MNG_9 to MNG_12.

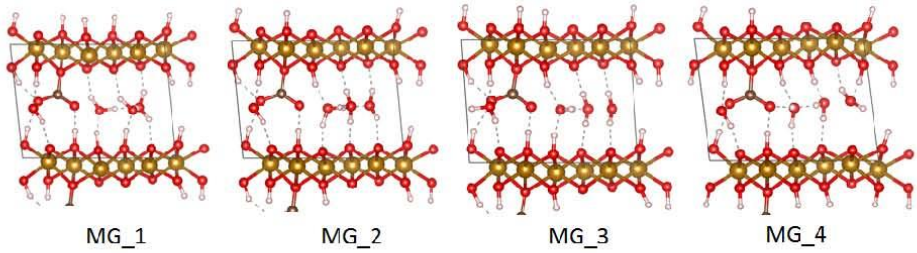

Figure S3: The side views of optimized lowest energy structures for mössbauerite with carbonate grafted for ($5OH^-/2OH^-$) configuration from MG_1 to MG_4.

S3

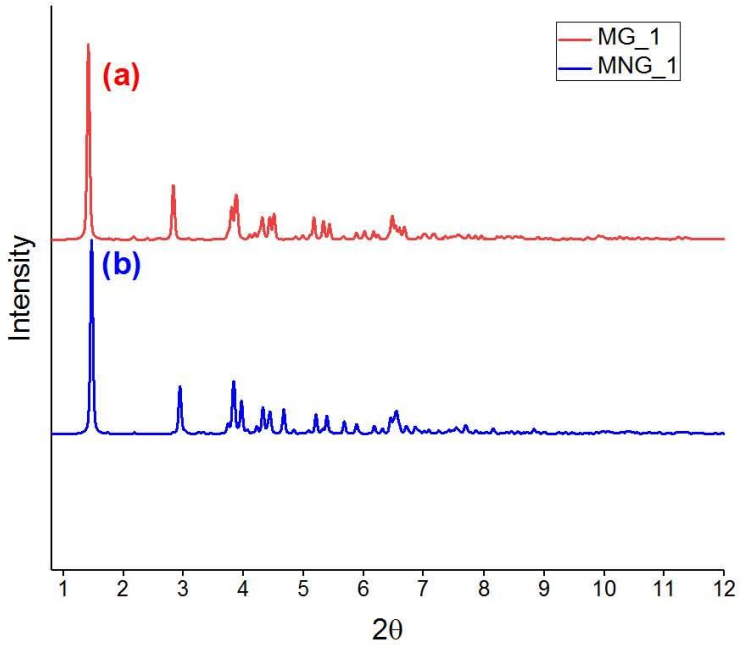

Figure S4: Simulated PXRD patterns for mössbauerite structure (a) without grafting ($5OH^-/3OH^-$)-MNG_1 and (b) with grafting ($5OH^-/2OH^-$)-MG_1 of carbonate.

S5: Cif file for computational geometry optimized structure for non-grafted mössbauerite [($5OH^-/3OH^-$)-MNG_1 in Tab. 2].

#==========

CRYSTAL DATA

#----------

data_VESTA_phase_1

S4

```
_chemical_name_common          'Generated by cif2cell 1.2.10. : Fail'
_cell_length_a                 5.44225
_cell_length_b                 10.88133
_cell_length_c                 7.31172
_cell_angle_alpha              85.43613
_cell_angle_beta               101.41692
_cell_angle_gamma              120.28811
_space_group_name_H-M_alt      'P 1'
_space_group_IT_number         1

loop_
_space_group_symop_operation_xyz
  'x, y, z'

loop_
  _atom_site_label
  _atom_site_occupancy
  _atom_site_fract_x
  _atom_site_fract_y
  _atom_site_fract_z
  _atom_site_adp_type
  _atom_site_B_iso_or_equiv
  _atom_site_type_symbol
  H1     1.0   0.730363   0.162553   0.232388   Biso  1.000000 H
```

S5

H2	1.0	0.096309	0.015381	0.231847	Biso	1.000000	H
H3	1.0	0.398005	0.330540	0.219460	Biso	1.000000	H
H4	1.0	0.067453	0.492149	0.229366	Biso	1.000000	H
H5	1.0	0.759312	0.669644	0.230117	Biso	1.000000	H
H6	1.0	0.168896	0.486289	0.570996	Biso	1.000000	H
H7	1.0	0.191558	0.617101	0.448976	Biso	1.000000	H
H8	1.0	0.501039	0.837720	0.556074	Biso	1.000000	H
H9	1.0	0.410140	0.828974	0.322929	Biso	1.000000	H
H10	1.0	0.709403	0.752129	0.439122	Biso	1.000000	H
H11	1.0	0.882710	0.679442	0.549279	Biso	1.000000	H
H12	1.0	0.879192	0.154353	0.662042	Biso	1.000000	H
H13	1.0	0.746975	0.402633	0.440690	Biso	1.000000	H
H14	1.0	0.252447	0.008374	0.655860	Biso	1.000000	H
C1	1.0	0.502999	0.194490	0.452868	Biso	1.000000	C
Fe1	1.0	0.328378	0.163654	0.933099	Biso	1.000000	Fe
Fe2	1.0	0.643711	0.492242	0.916927	Biso	1.000000	Fe
Fe3	1.0	0.319307	0.664454	0.931346	Biso	1.000000	Fe
Fe4	1.0	0.987650	0.333479	0.933036	Biso	1.000000	Fe
Fe5	1.0	0.982060	0.816508	0.935824	Biso	1.000000	Fe
Fe6	1.0	0.651311	0.981748	0.955177	Biso	1.000000	Fe
O1	1.0	0.616888	0.319804	0.812904	Biso	1.000000	O
O2	1.0	0.278220	0.488026	0.798853	Biso	1.000000	O
O3	1.0	0.624336	0.827624	0.811054	Biso	1.000000	O
O4	1.0	0.728709	0.184409	0.462495	Biso	1.000000	O
O5	1.0	0.531996	0.326964	0.427474	Biso	1.000000	O

S6

O6	1.0	0.248454	0.092587	0.455963	Biso	1.000000	O
O7	1.0	0.943408	0.152541	0.801279	Biso	1.000000	O
O8	1.0	0.943498	0.653193	0.796880	Biso	1.000000	O
O9	1.0	0.281829	0.993826	0.795082	Biso	1.000000	O
O10	1.0	0.693863	0.156298	0.092771	Biso	1.000000	O
O11	1.0	0.347012	0.325464	0.078874	Biso	1.000000	O
O12	1.0	0.697483	0.656538	0.085644	Biso	1.000000	O
O13	1.0	0.353301	0.832186	0.080676	Biso	1.000000	O
O14	1.0	0.032354	0.494594	0.088458	Biso	1.000000	O
O15	1.0	0.039714	0.000715	0.093217	Biso	1.000000	O
O16	1.0	0.080602	0.509866	0.448318	Biso	1.000000	O
O17	1.0	0.450059	0.783357	0.439825	Biso	1.000000	O
O18	1.0	0.854047	0.722976	0.428389	Biso	1.000000	O

S6: Cif file for computational geometry optimized structures for grafted mössbauerite [($5OH^-/3OH^-$)-MG_1 in Tab. 2].

#==========
==

CRYSTAL DATA

#----------

data_VESTA_phase_1

S7

```
_chemical_name_common              'Generated by cif2cell 1.2.10.  :  Fail'
_cell_length_a                     5.45062
_cell_length_b                     10.86357
_cell_length_c                     7.15695
_cell_angle_alpha                  87.78951
_cell_angle_beta                   104.23888
_cell_angle_gamma                  120.62983
_space_group_name_H-M_alt          'P 1'
_space_group_IT_number             1

loop_
_space_group_symop_operation_xyz
  'x, y, z'

loop_
  _atom_site_label
  _atom_site_occupancy
  _atom_site_fract_x
  _atom_site_fract_y
  _atom_site_fract_z
  _atom_site_adp_type
  _atom_site_B_iso_or_equiv
  _atom_site_type_symbol
  H1      1.0   0.789732   0.155229   0.320827   Biso  1.000000 H
  H2      1.0   0.130171   0.054305   0.257964   Biso  1.000000 H
```

S8

H3	1.0	0.429100	0.359636	0.239025	Biso	1.000000	H
H4	1.0	0.041774	0.500473	0.218581	Biso	1.000000	H
H5	1.0	0.805791	0.694503	0.239660	Biso	1.000000	H
H6	1.0	0.140621	0.488357	0.532152	Biso	1.000000	H
H7	1.0	0.261912	0.635344	0.434834	Biso	1.000000	H
H8	1.0	0.556283	0.835128	0.579885	Biso	1.000000	H
H9	1.0	0.478289	0.848947	0.340714	Biso	1.000000	H
H10	1.0	0.784578	0.778656	0.440261	Biso	1.000000	H
H11	1.0	0.919484	0.680718	0.516854	Biso	1.000000	H
H12	1.0	0.890892	0.140111	0.652684	Biso	1.000000	H
H13	1.0	0.562698	0.109669	0.444969	Biso	1.000000	H
H14	1.0	0.247628	0.026011	0.664348	Biso	1.000000	H
C1	1.0	0.437617	0.273629	0.559968	Biso	1.000000	C
Fe1	1.0	0.344741	0.167278	0.970052	Biso	1.000000	Fe
Fe2	1.0	0.637655	0.503949	0.904384	Biso	1.000000	Fe
Fe3	1.0	0.312840	0.669021	0.927805	Biso	1.000000	Fe
Fe4	1.0	0.000440	0.333187	0.936022	Biso	1.000000	Fe
Fe5	1.0	0.979270	0.822154	0.933036	Biso	1.000000	Fe
Fe6	1.0	0.653090	0.995626	0.958015	Biso	1.000000	Fe
O1	1.0	0.737647	0.105728	0.437493	Biso	1.000000	O
O2	1.0	0.249892	0.481288	0.787754	Biso	1.000000	O
O3	1.0	0.612590	0.831837	0.810713	Biso	1.000000	O
O4	1.0	0.555534	0.308092	0.758471	Biso	1.000000	O
O5	1.0	0.315054	0.140033	0.498166	Biso	1.000000	O
O6	1.0	0.461523	0.373706	0.459645	Biso	1.000000	O

O7	1.0	0.945653	0.154476	0.801690	Biso	1.000000	O
O8	1.0	0.925338	0.654923	0.783681	Biso	1.000000	O
O9	1.0	0.261265	-0.006117	0.798801	Biso	1.000000	O
O10	1.0	0.724944	0.186425	0.081392	Biso	1.000000	O
O11	1.0	0.386406	0.345464	0.090230	Biso	1.000000	O
O12	1.0	0.703047	0.669283	0.079425	Biso	1.000000	O
O13	1.0	0.366910	0.845274	0.082284	Biso	1.000000	O
O14	1.0	0.013893	0.497739	0.065753	Biso	1.000000	O
O15	1.0	0.063257	0.023818	0.115970	Biso	1.000000	O
O16	1.0	0.089419	0.533560	0.417953	Biso	1.000000	O
O17	1.0	0.528772	0.797002	0.445774	Biso	1.000000	O
O18	1.0	0.930119	0.750387	0.421432	Biso	1.000000	O

7. List of Publications

1. "Oxygen Evolution Catalysis with Mössbauerite – A Trivalent Iron-Only Layered Double Hydroxide"

   Michael Ertl, Corina Andronescu, Jonathon Moir, Mirijam Zobel, F. E. Wagner, Geoffrey A. Ozin, Wolfgang Schuhmann, Josef Breu

   Chem. Eur. J., **2018**, *24*, 9004-9008.

2. "Mössbauerite as Iron-only Oxyhydroxide Catalyst for WO_3 Photoanodes"

   Michael Ertl, Zili Ma, Thomas Thersleff, Pengbo Lyu, Sven Hüttner, Petr Nachtigall, Josef Breu, Adam Slabon

   Inorg. Chem., **2019**, *58*, 9655-9662.

3. "Structure Determination of the Oxygen Evolution Catalyst Mössbauerite"

   Pengbo Lyu, **Michael Ertl**, Christopher J. Heard, Lukáš Grajciar, A.V. Radha, Thomas Martin, Josef Breu, Petr Nachtigall

   J. Phys. Chem. C, **2019**, *123*, 25157-25165.

4. "Clinical Wastewater Treatment: Photoelectrochemical Removal of an Anionic Antibiotic (Ciprofloxacin) by Mesostructured High Aspect Ratio ZnO Nanotubes"

   Carina Bojer, Judith Schöbel, Thomas Martin, **Michael Ertl**, Holger Schmalz, Josef Breu

   Appl. Cat. B., **2017**, *204*, 561-565.

This thesis is based on publications 1-3.

8. Acknowledgements

First of all, I would like to thank my supervisor, Prof. Dr. Josef Breu, for his trust, his advice and for the great opportunities he has provided me since I joined his team in June 2016. He has always been a great source of inspiration and motivation throughout my time as a doctoral student at the chair Inorganic Chemistry I in Bayreuth.

Professor Dr. Geoffrey Ozin who was an amazing host and supervisor during my time in Toronto. Also, I would like to thank his entire team and of course especially Dr. Jonathon Moir for his guidance in electrochemistry, cooperation and all his efforts with our manuscript.

Professor Dr. Wolfgang Schuhmann and especially Prof. Dr. Corina Andronescu, who I wish all the best for her career, for their cooperation and also for their time and effort with our manuscript.

Prof. Dr. Adam Slabon and Zili Ma for our joint project that I enjoyed greatly.

Prof. Dr. Petr Nachtigall and Dr. Pengbo Lyu for our joint project, for the discussions and for being great cooperation partners in the framework of the BTHA.

Prof. Dr. Sven Hüttner, Prof. Dr. Friedrich Wagner, Prof. Dr. Mirijam Zobel, and Prof. Dr. Jean-Marie Refait Génin for their advice, collaboration, help, and inspiration.

I would like to thank the Hanns-Seidel-Stiftung for the financial and ideational support within a doctoral scholarship.

Lena Geiling, Marco Schwarzmann, and Dr. Wolfgang Milius for their time, help, and effort with everything in and around the lab.

Petra Seidler, Iris Raithel and Sieglinde Hörath for taking care of everything organizational to ensure a smooth work routine for the rest of the group.

My colleagues in the AC1 and especially Sonja Amschler, Raphael Kunz, Christoph Habel, and Sebastian Weiß for being great colleagues and great friends.

Finally, my deep and sincere gratitude for my family and their continuous support. This work is dedicated to them.

9. Eidesstattliche Verfassers

(Eidesstattliche) Versicherungen und Erklärungen

(§ 9 Satz 2 Nr. 3 PromO BayNAT)

Hiermit versichere ich eidesstattlich, dass ich die Arbeit selbstständig verfasst und keine anderen als die von mir angegebenen Quellen und Hilfsmittel benutzt habe (vgl. Art. 64 Abs. 1 Satz 6 BayHSchG).

(§ 9 Satz 2 Nr. 3 PromO BayNAT)

Hiermit erkläre ich, dass ich die Dissertation nicht bereits zur Erlangung eines akademischen Grades eingereicht habe und dass ich nicht bereits diese oder eine gleichartige Doktorprüfung endgültig nicht bestanden habe.

(§ 9 Satz 2 Nr. 4 PromO BayNAT)

Hiermit erkläre ich, dass ich Hilfe von gewerblichen Promotionsberatern bzw. -vermittlern oder ähnlichen Dienstleistern weder bisher in Anspruch genommen habe noch künftig in Anspruch nehmen werde.

(§ 9 Satz 2 Nr. 7 PromO BayNAT)

Hiermit erkläre ich mein Einverständnis, dass die elektronische Fassung meiner Dissertation unter Wahrung meiner Urheberrechte und des Datenschutzes einer gesonderten Überprüfung unterzogen werden kann.

(§ 9) Satz 2 Nr. 8 PromO BayNAT)

Hiermit erkläre ich mein Einverständnis, dass bei Verdacht wissenschaftlichen Fehlverhaltens Ermittlungen durch universitätsinterne Organe der wissenschaftlichen Selbstkontrolle stattfinden können.

München, 14.05.2020
……

Ort, Datum, Michael Ertl